AIX-MARSEILLE UNIVERSITÉ

INVESTIGATING BLUNT AORTIC RUPTURE MECHANISMS IN MOTOR VEHICLE CRASH ACCIDENTS: THE ROLE OF INTRA-AORTIC PRESSURE

WEI WEI

ECOLE DOCTORALE 463-SCIENCES DU MOUVEMENT HUMAIN

THÉSE PRÉSENTÉE EN VUE DE L'OBTENTION

DU DIPLÔME DE DOCTEUR ES SCIENCE

SPECIALITE BIOMECANIQUE

DÉCEMBRE 2018

© Wei WEI, 2018.

AIX-MARSEILLE UNIVERSITÉ

ECOLE DOCTORALE 463-SCIENCES DU MOUVEMENT HUMAIN

Cette thèse est intitulée :

ETUDE SUR LES MÉCANISMES CONTONDANTS DE RUPTURE AORTIQUE PROVOQUÉS PAR LA PRESSION INTRA-AORTIQUE INDUITE LORS DES ACCIDENTS DE LA ROUTE

présentée par : WEI Wei

en vue de l'obtention du diplôme de : Docteur Es Science

a été dûment acceptée par le jury d'examen constitué de :

M BEHR Michel, Ph.D	Directeur de thèse
M KAHN Cyril J.F., Ph.D	Codirecteur de thèse
M MO Fuhao, Ph.D	Examinateur
Mme EVIN Morgane , Ph.D	Examinatrice
M BASTIEN Christophe, Ph.D	Rapporteur
M LALANDE Alain, Ph.D	Rapporteur

ACKNOWLEDGEMENTS

First of all, I would like to greatly appreciate the committee members: Prof. Christophe Bastien, Dr. Alain Lalande, Prof. Fuhao Mo and Dr. Morgane Evin for kindly accepting to serve on my doctoral committee and valuable critique on my research work.

I would like to express gratitude to Michel Behr and Cyril J.F Kahn, the directors of my thesis, for your great support and guidance throughout my doctoral studies. You have always provided me encouragement, valuable advice and many great ideas all these years. I am also grateful to you both for your great help in my live, especially during the first year when I did not speak French at all. I still remember the first day when I arrived at the airport and Cyril went to pick me up. I also remember the plenty of time Cyril spent on translating to me the numerous French-written documents. Of course, I will forever remember the help of Michel to register in the hospital for the delivery of my wife and to register in the daycare for my son.

I am very thankful to Morgane Evin and Pierre-Jean Arnoux for your valuable discussion and great support during my Ph.D work. Thanks to Aurélien Culver for your help in experiment setup and in aorta dissection. I am also grateful to all the members of LBA who helped me with scientific problems and French difficulties: Catherine Masson, Lionel Thollon, Yves Godio-Raboutet, Max Py, Audrey Chenel, Manon Sterba, Marion Fournely, Nicolas Bailly, Rohan Bianco, Tristan Tarrade, Guillermo de la Rosa, Axel Legouge, Brieg Lecoublet, Floriane Remy, Oscar Cherta…

Most importantly, I would like to thank my father Yi Wei, my mother Ping Yan, my wife Yizhen Li and my son Randy Wei, who have been providing me infinite love and support. Without your always being with me, I cannot succeed in my career.

RÉSUMÉ

La rupture de l'aorte (RA) est la lésion la plus commune parmi les larges vaisseaux et est détectée dans 10% à 15% des cas mortels liés aux accidents de voiture. Les mécanismes variés de RA (incluant l'éclatement soudain de l'aorte, la contrainte de l'aorte par les structures osseuses, l'augmentation soudaine de la pression appelée « coup de bélier » et la combinaison des mécanismes ci-dessus) peuvent être considérés comme a combinaison de deux types de contributions: la distraction aortique et la pression aortique. La dilatation aortique est liée aux mouvements de l'aorte résultant de la compression thoracique et est considérée comme un mécanisme primaire de RA. Cependant, l'effet de la pression sur la RA reste indéterminé.

Des tests expérimentaux précédents sur échantillons cadavériques ont montré la difficulté de reproduire la RA ou de fournir des informations sur l'indice de lésion pour la RA. Les simulations par éléments finis n'ont pas permis d'études les mécanismes associés à la RA sur la contribution respective de ces deux phénomènes (i.e. distraction aortique et pression intra-aortique). Ainsi, la réponse aortique et les mécanismes associés au RA restent incertains dans des conditions physiologiques de pression intra-aortique (écoulement sanguin) et les interactions avec les organes intra-thoraciques pendant les accidents de voiture.

Pour étudier les mécanismes liés aux RAs dans les accidents de voitures en se focalisant sur les mécanismes associés à la pression intra-aortique, le travail est organisé en quatre parties: 1) quantifier la réponse aortique sous des conditions de chargement physiologiques, 2) identifier la nécessité de considérer la pression intra-aortique dans les RA associés aux accidents de voiture, 3) développer un modèle d'éléments finis incluant une fonction cardiaque réaliste et 4) et finalement étudier le mécanisme de RA pendant les accidents avec le modèle nouvellement développé. Les réponses aortiques sous des conditions de chargements physiologiques associés à l'activité cardiaque sont comparables avec ceux attendus pendant les accidents de voiture et devraient être simulées dans la simulation de la RA. La pression intra-aortique peut entrainer un risque important de la RA en cas d'accidents et est un facteur de risque critique pour une meilleure prédiction de la RA. La RA dans les accidents de voitures résulte d'un mécanisme combiné de l'étirement de l'aorte et de la pression intra-aortique dans lequel l'étirement aortique est la cause primaire et la pression intra-aortique la cause secondaire.

ABSTRACT

Blunt aortic rupture (BAR) is the most common injury among large mediastinal vessels. BAR was detected in 10% to 15% of vehicle mortalities. BAR and as the second leading cause of death following blunt trauma in motor vehicle crash accidents (MVCAs). Various BAR mechanisms (including sudden aortic stretch, aorta entrapment by bony structures; sudden blood pressure stroke referred to as "water hammer effect" and the combination of these mechanisms above) could be considered as a combination of two sources of contribution: aortic distraction and intra-aortic pressure. The aortic distraction is related to aortic motions resulting from thoracic compression and was postulated to be a primary BAR mechanism. However, the pressure effects on BAR remain to be indeterminate.

Previous attempts to investigate BAR mechanisms included experimental tests on human or animal cadavers yielded limited success in reproducing BARs. The effects of human physiological activity on BARs could be challenging to be reproduced in cadaver experiments. Previous finite element (FE) models did not simultaneously investigate the BAR mechanisms of the two contribution sources (i.e. aortic distraction and intra-aortic pressure). Therefore, the aortic responses and BAR mechanisms remain to be ascertained under the effects of physiological intra-aortic pressure (blood flow) and intra-thoracic organ interactions during MVCAs.

The objective of the current work is to investigate BAR mechanisms in MVCAs with a focus on intra-aortic pressure mechanism. The work is organized in four parts: 1) to quantify aortic responses under physiological cardiac function, 2) to identify the necessity of considering intra-aortic pressure for MVCA-related BARs, 3) to develop a FE model including realistic cardiac function and 4) finally to investigate the BAR mechanism during MVCA with the newly developed FE model. The aortic responses under physiological cardiac loadings were comparable with those expected in MVCAs and should be considered for MVCA-related BARs. Intra-aortic pressure could induce a significant BAR risk in MVCAs and was a critical factor to better predict BARs. The modeling of intercostal artery to constrain the descending aorta was also essential to predict BAR occurrences. The BAR in MVCA resulted from a combined mechanism of aortic stretch and intra-aortic pressure, in which aortic stretch was the primary cause with intra-aortic pressure as the secondary cause.

TABLE OF CONTENTS

ACKNOWLEDGEMENTS V
RÉSUMÉ VII
ABSTRACT IX
TABLE OF CONTENTS XI
LIST OF TABLES XVII
LIST OF FIGURES XIX
LISTE OF ABBREVIATIONS XXV
LIST OF APPENDIX XXVII
CHAPTER 1 INTRODUCTION 1
CHAPTER 2 REVIEW OF INJURY BIOMECHANICS FOR BLUNT AORTIC RUPTURE 7
  2.1 Anatomy of aorta 7
  2.2 Structure of aortic wall 9
  2.3 Epidemiologic study of BAR 10
  2.4 Aortic injury mechanisms 11
    2.4.1 Inertia-based 11
    2.4.2 Pressure-based 12
    2.4.3 Stretch-based 12
    2.4.4 Others 13
  2.5 Previous research approaches to simulate BAR mechanisms 14
    2.5.1 Experimental studies 14
    2.5.2 FE human body models 18
CHAPTER 3 AORTIC STRESS LEVEL DURING CARDIAC CYCLE 23
  3.1 Introduction 23

3.2 Article #1: Investigating Heartbeat-Related In-Plane Motion and Stress Levels Induced at the Aortic Root 27
3.2.1 Introduction 28
3.2.2 Materials and methods 29
3.2.3 Results 34
3.2.4 Discussion 39
3.2.5 Conclusions 43
3.3 Aortic stress level against stress thresholds 44
CHAPTER 4 INTRA-AORTIC PRESSURE IN MVCA 47
4.1 Introduction 47
4.2 Article #2: Intra Luminal Pressure as a Determinant Factor in Blunt Aortic Rupture: an Experimental Ex-Vivo Study 50
4.2.1 Background 52
4.2.2 Methods 53
4.2.3 Results 55
4.2.4 Discussion 58
4.2.5 Conclusion 60
4.2.6 Author contribution 61
4.3 Article #3: Intraluminal Pressure Should be Considered for Blunt Aortic Rupture Prediction in Car Crash Accidents: a Numerical Analysis 61
4.3.1 Introduction 62
4.3.2 Methods 63
4.3.3 Results 68
4.3.4 Discussion 71
4.3.5 Conclusions 74

4.3.6 Conflict of interest ... 75

4.3.7 Acknowledgements ... 75

CHAPTER 5 FSI SIMULATION OF AORTIC BLOOD FLOW DURING CARDIAC CYCLE AND MVCA ... 77

5.1 Introduction ... 77

5.1.1 Anatomy ... 78

5.1.2 Physiology ... 82

5.1.3 FSI approaches in LS-DYNA ... 84

5.2 Article #4: Fluid-Structure Interaction Simulation of Aortic Blood Flow by Ventricular Beating: a Preliminary Model for Blunt Aortic Injuries in Vehicle Crashes ... 88

5.2.1 Introduction ... 89

5.2.2 Material and methods ... 90

5.2.3 Results ... 95

5.2.4 Discussion ... 99

5.2.5 Limitations ... 101

5.2.6 Conclusions ... 102

5.2.7 Conflict of interest ... 102

CHAPTER 6 AORTIC STRESS LEVEL AND BAR MECHANISM IN MVCA ... 103

6.1 Aortic stress level under the loadings of blood pressure and intra-thoracic interactions in MVCAs ... 104

6.1.1 Introduction ... 104

6.1.2 Material and methods ... 105

6.1.3 Results ... 109

6.1.4 Discussion ... 111

6.2 Aortic stress level under different intra-aortic pressure conditions in MVCAs ... 113

6.2.1 Introduction 113

6.2.2 Material and methods 114

6.2.3 Results 115

6.2.4 Discussion 118

6.3 Conclusion 120

CHAPTER 7 GENERAL DISCUSSION AND CONCLUSION 123

REFERENCES 131

APPENDIX A STRESS DISTRIBUTION OF STRUCTURAL AND FSI SIMULATIONS . 149

APPENDIX B BLOOD VELOCITY PROFILE AND WSS AT AA, PDA AND DDA 150

APPENDIX C ELEMENT AXIS ORIENTATION 152

APPENDIX D PARAMETRIC COMPARISON BETWEEN CASE DESCRIPTIONS AND FE MODELS FOR RECONSTRUCTION 154

APPENDIX E MINI-SLED ACCELERATIONS 155

APPENDIX F AORTIC DEFLECTION IN MINI-SLED TESTS 156

APPENDIX G OBLIQUE-FRONTAL CRASH RECONSTRUCTION 158

APPENDIX H THE EQUATION OF STATE (EOS) FOR BLOOD AND THE RELATIVE VOLUME TIME-HISTORY FOR FLUID OUTFLOW 159

APPENDIX I PARAMETRIC COMPARISON BETWEEN CASE DESCRIPTIONS AND NUMERICAL RECONSTRUCTION 161

APPENDIX J BLOOD PRESSURE TIME-HISTORY IN THE ASCENDING AORTA AND DESCENDING AORTA 162

APPENDIX K TIME-HISTORY OF SECTION-AVERAGED BLOOD VELOCITY FOR SECTION 3, 4, 6 AND 8 163

APPENDIX L TIME-HISTORY OF BLOOD FLOW RATE FOR SECTION 3, 6 AND 8 ... 164

APPENDIX M SECTION-AVERAGED WSS EVALUATION 165

APPENDIX N DEFORMATION PATTERNS OF NUMERICAL RECONSTRUCTION AND CASE VEHICLE.......... 167

APPENDIX O DETAILED INFORMATION OF SAMPLE PROPERTIES (GENDER, AGE, DIAMETERS AND LENGTH).......... 168

LIST OF TABLES

Table 2.1 Summary of simulation setup in the 8 nearside lateral impact reconstructions (adapted from [21]) 22

Table 3.1 Summary of aortic ultimate stress for longitudinal and transverse direction during quasi-static and dynamic stretch tests [73] 23

Table 3.2: Aortic volumes, diameters of different sections and the averaged stress at the proximal AA section 2cm above the AR in control model and FSI simulations 37

Table 3.3: Averaged VonMises, circumferential and longitudinal stress for proximal AA 2cm above the AR in structural simulations 39

Table 3.4 Peak stresses and stretch ratio of aortic wall during cardiac cycle, MVCAs [17, 19, 21, 101] and tensile failure tests[98, 100] 45

Table 4.1: Summary of specimen parameters, burst pressures and rupture locations 56

Table 4.2. Intrusions of frontal crash reconstruction compared with case vehicle crush profiles . 70

Table 5.1. Aortic diameters at different sections comparing with the data in literature [135, 136]. 90

Table 5.2. Intrusions of vehicle-pole impact reconstruction compared with case vehicle crush profiles 97

Table 6.1 Calculation expenses of the Original GHBMC, Integrated FSI and Sub-model FSI simulation for 120ms-duration oblique-frontal and lateral crashes 110

Table 6.2 Peak values of aortic VonMises stress and maximum principal strain during the simulations of Integrated-FSI, Airbag-0mmHg, Airbag-50mmHg and Airbag-120mmHg 117

LIST OF FIGURES

Figure 1.1: Workflow of the whole study to show the logic relationship among different chapters 3

Figure 2.1: Anatomy of isolated aorta to show different aortic segments and branches (adapted from http://humananatomychart.us/page/10/) 7

Figure 2.2: Anatomy of the mediastinum to show the thoracic aorta and its surrounding organs, where H and D correspond to heart and diaphragm (adapted from https:// radiologykey.com/mediastinum-and-heart/) 8

Figure 2.3: Micro-structure of aortic wall (adapted from [26]) 9

Figure 2.4: Schematic diagram of BAR mechanisms (adapted from [7]) 13

Figure 2.5: Experimental setup for frontal impact at mid-sternum of human cadaver (adapted from [13]) 15

Figure 2.6: Initial experimental configuration for canine thoracic impact (adapted from [64]) 16

Figure 2.7: Experimental setup of entire aorta burst: A) schematic of pressurization apparatus; B) Schematic of instrumented whole aorta for in vitro pressure impulse testing (adapted from [11]) 17

Figure 2.8: Thoracic FE model by Shah et al. (adapted from [70]) 19

Figure 2.9: The Wayne State Human Body Model (WSHBM): (a) global view of the model, (b) upper trunk (c) sagittal section of the chest with the shoulder, ribcage and the left lung removed to view the mediastinum contents (adapted from [71]) 20

Figure 2.10: In vitro FE model of human aorta (adapted from [22]) 21

Figure 3.1 Experimental and computed results of Cauchy stress versus stretch during aortic uniaxial stretch test (adapted from [74]) 24

Figure 3.2 Aortic stress levels reconstructed from vehicle lateral impact cases (adapted from[19]) 25

Figure 3.3 Maximum principal stress contours of the heart and the aorta at the time when the maximum stress was generated in each model (adapted from [75]) 26

Figure 3.4: Oblique sagittal MRI image showing the locations of different aortic sections, the corresponding slice at AA for measuring its in-plane motion, the MRI reference system (MRI Sys) and the PDA system (PDA Sys)..30

Figure 3.5: Aortic FE model and boundary conditions: aortic FE model for structural and FSI simulation (a); boundary conditions for SA-Pre (b), SA-Down (c), SA-XY (d) and SA-2XY (e). AA, PDA and DDA correspond to the sections of distensibility assessment.................32

Figure 3.6: In-plane motion of AA section. AA maximal in-plane motion in absolute value averaging among the volunteers (a); time-history of in-plane resultant and component displacements of a volunteer (25 years, male) (b). X-Disp-Abs and X-Disp-PDA: X component motion under MRI and PDA reference system; Y-Disp-Abs and Y-Disp-PDA: Y component motion under MRI and PDA reference system; Resultant Disp: in-plane resultant displacement..35

Figure 3.7: Aortic diameters and distensibility for AA, PDA and DDA: diameter time-history under the three-cycle pressure loading (a); aortic distensibility in simulation comparing with the literature data (b). The vertical dotted lines indicate the moments when the diameters were recorded for distensibility analysis..36

Figure 3.8: VonMises, circumferential and longitudinal stress distribution for structural simulations with different AA motions..38

Figure 4.1 Schematic illustration of the sled test system to reproduce BAR with limited thoracic deformation (adapted from [12])..48

Figure 4.2 Weibull injury risk for aortic bust tests under pressure impulse loading (adapted from [11])..48

Figure 4.3 Representative frontal impact (top), side impact, with and without arm engagement (middle left and right, respectively), submarining simulation (bottom left), and oblique impact (bottom right) configurations (adapted from [9])...49

Figure 4.4: System configuration for aorta pressurization..55

Figure 4.5: High-speed photos of Aorta-3 burst test at different moments: the first moment of visible rupture (defined as t=0ms), complete aortic rupture (t=5ms), the beginning of latex inflation (t=6ms) and complete latex inflation (t=10ms). 56

Figure 4.6: Mean value of pressure versus time recorded in aortic burst tests along with the experimental corridor and the pressure time-history of the latex tube inflation test. The grey dotted lines correspond to the range of variation for different points on the average curve, which was used to obtain the experimental corridor as previously detailed [114]. 57

Figure 4.7: Weibull injury risk of aorta for pressure loadings compared with the same curve reported by Bass et al. [11]..57

During the aortic burst tests performed in this study, an innovative way was used to prevent leakage by fitting a thin-layered latex tube in the aortic lumen. As previously reported [12], leakage is tough to avoid under physiological pressures solely with sutures and can be quite a problem under higher loadings. On one hand, our combined utilization of latex tube with sutures minimized leakage with a simple and reproducible procedure. On the other hand, the latex sheath has no significant influence on the accuracy of failure pressure measurement due to its much higher compliance than aortas (Figure 4.5 and Figure 4.6). 58

Figure 4.8: Platform configuration of mini-sled test..65

Figure 4.9. Simulation setup for car crash reconstruction: vehicle-barrier crash (stage 1) and occupant-seat impact model (stage 2) 67

Figure 4.10. Aortic deflections in mini-sled tests: deflection time-history of Aorta-3 (a) where P-50 and P-200 correspond to pressure 50mmHg and 200mmHg; peak deflections of all the aortas for Impact-20 (b) and for Impact-20° (c)..69

Figure 4.11. Simulation results of occupant injuries: contour plots of effective plastic strains for ribs (a), max principal strain for lungs (b), VonMises stress for aorta (c) and blood pressure recorded in aorta (d) at t=100ms in stage 2 70

Figure 5.1 Subdivision of mediastinum as seen on sagittal section: (1) superior mediastinum (2) anterior mediastinum (3) medial mediastinum (4) posterior mediastinum (adapted from https://home.comcast.net/~wnor/thoraxlesson3.htm) 79

Figure 5.2 Schematic of the heart showing valves, arteries and veins (The white arrows shows the normal direction of blood flow) (adapted from http://en.wikipedia.org/wiki/Heart)............80

Figure 5.3 Anterior views of coronary circulation (adapted from http://en.wikipedia.org/wiki/ Coronary_ circulation) 81

Figure 5.4 Blood flow patterns of cardiac cycle (adapted from http://www.cvphysiology.com/ Heart%20Disease/HD002.htm). Ao: aorta; IVC: inferior vena cava; LA: left atrium; LV: left ventricle; PA: pulmonary artery; RA: right atrium; RV: right ventricle; SVC: superior vena cava....82

Figure 5.5 Time history of blood pressure and volume during a single cardiac cycle (AP: aortic pressure; LVP: left ventricular pressure; LAP: left atrial pressure; LVEDV: the left ventricular end-diastolic volume; LVESV: the left ventricular end-systolic volume; ECG: electrocardiogram) (adapted from http://www.cvphysiology.com/Heart%20Disease/HD002.htm)....83

Figure 5.6. Schematic drawing to show the deformation and translation of meshes in different formulations: (A) Lagrangian, (B) Eulerian and (C) ALE....87

Figure 5.7. FE model of heart-aorta system. (A) FE model displaying the location of boundary constraints on the descending aorta (red points) and on the heart (orange area in dash lines), (B) FE model showing structural components, fluid domain and the locations of each aortic section....91

Figure 5.8. BAR-related MVCA reconstruction with the heart-aorta integrated human FE model. (A) the whole human FE model integrated with the heart-aorta FSI model, (B) stage 1 of MVCA reconstruction with car-pole side impact, (C) stage 2 of MVCA reconstruction with occupant-vehicle interaction....94

Figure 5.9. The time-history of LV volume (A) and blood pressure (B). The landmarks on LV volume change curve correspond to different cardiac moments when the LV began to contract (A), the LV began to eject (B), the LV stopped ejecting (C) as well as the LV began to recover its volume (D)....95

Figure 5.10. Blood flow and WSS at aortic section 1. (A) Peak blood velocity of section 1 during the cycle where landmark I, II and III represent respectively the beginning of LV ejection, the peak ejection and the beginning of diastole. (B) The blood flow profile fitted with cubic spline at the moment corresponding to landmark II. (C) Section-averaged blood velocity. (D) Blood flow stream line in the LV and aorta at the moment of landmark II. The dash line arrow represents the blood flow direction and the aortic midline from section 1 to 8 for measuring pulse wave velocity. (E) Blood flow rate. (F) Section-averaged WSS. (G) WSS distribution at the moment of landmark II. 96

Figure 5.11. Simulation results of occupant injuries: contour plots of effective plastic strains for rib cortical bones, VonMises stress for diaphragm and aorta at t=90ms in stage 2 98

Figure 5.12. The cardiac output during the reconstructed MVCA compared with the normal cardiac output from isolated heart-aorta model: LV volume (A), LV blood pressure (B), blood pressure (C) and section-averaged velocity (D) recorded at section 1.........................98

Figure 6.1 GHBMC-M50 body region and full body models (adapted from [155] and [142])...105

Figure 6.2 Model integration based on the GHBMC-M50 and the heart-aorta FSI models: (A) the original GHBMC-M50 model; (B) the partial enlarged figure to show the original GHBMC intra-thoracic organs with the lungs transparent; (C) the isolated heart-aorta FSI model; (D) the partial enlarged figure to show the intra-thoracic components of the integrated full body model; (E) the back-oblique view of the integrated model to show the groups of nodes, which are the red dots in the black dashed regions, for defining the “node-to-surface” tied contacts.....................107

Figure 6.3 Oblique-frontal impact simulation with the Integrated FSI model (A) and lateral impact simulation with the Original GHBMC model (B)....................109

Figure 6.4 Aortic stress and strain distributions of the Original GHBMC and Integrated FSI simulations for oblique-frontal and lateral crash....................110

Figure 6.5 Aortic mobility measurement relative to vertebrae T7 with the global space system 115

Figure 6.6 Aortic mobility in terms of aortic nodal displacements for Airbag-0mmHg, Airbag-50mmHg, Airbag-120mmHg and Integrated-FSI simulation 116

Figure 6.7 Airbag pressure time-histories during the crash for Airbag-0mmHg, Airbag-50mmHg and Airbag-120mmHg compared with the blood pressure measured at the aortic root during Integrated-FSI simulation....................116

Figure 6.8 Aortic stress and strain distributions of the integrated FSI and sub-model structural simulations for oblique-frontal and lateral crash....................117

LISTE OF ABBREVIATIONS

2D	Two-Dimensional
3D	Three-Dimensional
AA	Ascending Aorta
ALE	Arbitrary Lagrangian Eulerian
AR	Aortic Root
BAR	Blunt Aortic Rupture
CFD	Computational Fluid Dynamics
CIREN	Crash Injury Research and Engineering Network
CR	Computational Reference
NHTSA	National Highway Traffic Safety Administration
CA	Distal Descending Aorta at the Level of Coeliac Trunk
DA	Descending Aorta
DDA	Distal Descending Aorta
FE	Finite Element
FSI	Fluid-Structure Interaction
GHBMC	Global Human Body Models Consortium
LV	Left Ventricle
MR	Material Reference
MRI	Magnetic Resonance Imagining
MVCA	Moto Vehicle Crash Accident
PDA	Proximal Descending Aorta
ROI	Region of Interest
SR	Spatial Reference

STL	Stereolithography
WSS	Wall Shear Stress

LIST OF APPENDIX

APPENDIX A Stress distribution of structural and FSI simulations..149

APPENDIX B Blood velocity profile and WSS at AA, PDA and DDA..................................150

APPENDIX C Element axis orientation 152

APPENDIX D Parametric comparison between case descriptions and FE models for reconstruction...154

APPENDIX E Mini-sled accelerations 155

APPENDIX F Aortic deflection in mini-sled tests 156

APPENDIX G Oblique-frontal crash reconstruction...158

APPENDIX H The equation of state (EOS) for blood and the relative volume time-history for fluid outflow..159

APPENDIX I Parametric comparison between case descriptions and numerical reconstruction 161

APPENDIX J Blood pressure time-history in the ascending aorta and descending aorta 162

APPENDIX K Time-history of section-averaged blood velocity for section 3, 4, 6 and 8 163

APPENDIX L Time-history of blood flow rate for section 3, 6 and 8 164

APPENDIX M Section-averaged WSS evaluation..165

APPENDIX N Deformation patterns of numerical reconstruction and case vehicle.................167

APPENDIX O Detailed information of sample properties (gender, age, diameters and length) 168

CHAPTER 1 INTRODUCTION

Aorta is one of the major arteries in the human body and blunt aortic rupture (BAR) is the most common injury among large mediastinal vessels. BAR was detected in 10~15% of vehicle mortalities [1-3] and was reported as the second leading cause of death following blunt trauma in motor vehicle crash accidents (MVCAs) [4]. The majority of BARs occurring in MVCAs were found in vehicle occupants (53.5%), followed by pedestrians, motorcyclists, bicyclists and truck occupants [3]. BAR often leads to fatality with 85% of the victims deceased at the collision scene [5]. If untreated, 30% of the remaining injured will decease within 24 hours [5]. Multiple injury mechanisms of BAR have been proposed, including sudden stretching of the aorta with rupture at isthmus [6]; entrapment of the aorta by the surrounding bony structures [7]; sudden stroke of blood pressure with what is referred to in literature as the water hammer effect [8] and the combination of different mechanisms including these above [5].

To some extent, these mechanisms could be considered as a combination of two sources of contribution: aortic distraction and intra-aortic pressure. The aortic distraction is related to aortic motions resulting from thoracic compression and was postulated to be a primary BAR mechanism [9, 10]. However, the pressure effects on BAR are still controversial. Bass et al. [11] proposed a pressure-based injury index with a 101kPa threshold for 50% BAR risk. Forman et al. [12] suggested intraluminal pressure should only be a secondary mechanism due to the limited pressure gradient across the aortic wall during sled tests. Hardy et al. [9] further argued that blood pressure seemed unlikely to cause BAR alone considering the typical transverse rupture in MVCAs and Young-Laplace equation.

The BAR injury mechanisms above were proposed mainly based on previous observations from autopsies after MVCAs, followed by animal and human body ex-vivo experiments. To confirm or further study these injury mechanisms, finite element (FE) models of the whole human body and the isolated aorta were also used to simulate the scenarios relevant with MVCAs. However, these previous experimental or numerical efforts had their corresponding limitations. The experimental simulations on human or animal cadavers yielded limited success in reproducing aortic injury [9, 10, 12-16]. They could not throw direct insight on the aortic stress or strain level which was a useful index in investigating BAR mechanisms. Furthermore, the effects of human physiological activity (e.g. pulsatile intra-aortic pressure during cardiac cycle) on BARs could hardly be reproduced in cadaver experiments. FE simulations were able to obtain the aortic stress and strain information during MVCAs, but previous FE models always tended to be simplified. To be more specific, some models modeled the aortic blood with structural solid elements [17-21]. The aorta responses due to initial intra-aortic pressure and the pressure increase resulting from blood flow occlusion ("water hammer effect") were thus ignored in these models. Other models reproduced aortic blood flow in isolated aorta or aortic segment with fluid-structure interaction (FSI) approach, but they ignored the aortic responses resulting from interactions between aorta and intra-thoracic organs [22-24]. Therefore, previous FE models did not simultaneously investigate the BAR mechanisms of the two contribution sources (i.e. aortic distraction and intra-aortic pressure). In other words, the aortic responses and thus BAR mechanisms remain to be ascertained under the effects of physiological intra-aortic pressure (blood flow) and intra-thoracic organ interactions during MVCAs.

The objective of current work is to investigate BAR mechanisms in MVCAs with a focus on intra-aortic pressure mechanism.

To achieve this final objective, the current manuscript is organized as follows (see Figure 1.1):

- Chapter 2 provides a state of the art on aortic anatomy, aortic wall structure, BAR epidemiology, BAR mechanisms and previous research approaches on the mechanisms.

- Chapter 3 deals with an attempt to quantify the aortic wall stress levels under the effects of cardiac function, which combines the physiological intra-aortic pressure and the aortic root (AR) traction by left ventricle (LV) due to heartbeat. Aortic in-plane motion was assessed on magnetic resonance imagining (MRI) data. An isolated aorta FE model was developed and validated against the distensibility. Combining with the aortic longitudinal motion and the physiological intra-aortic pressure in literature, the aortic in-plane motion was applied to the aorta FE model to evaluate the aortic wall stress level under different conditions of cardiac function. The results of this chapter serve to answer the question whether it is reasonable to ignore cardiac function in MVCA-related studies (see Figure 1.1).

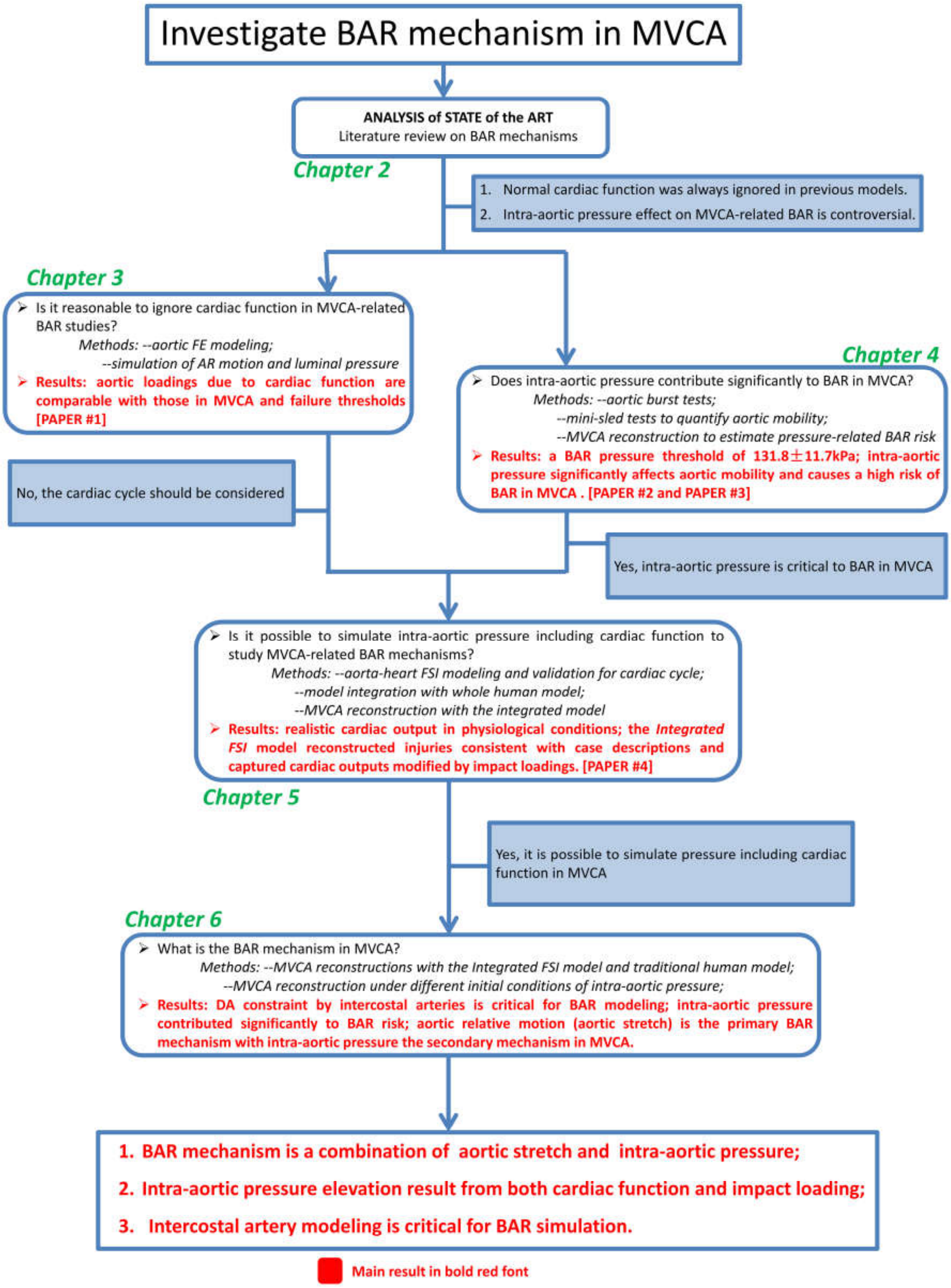

Investigate BAR mechanism in MVCA

ANALYSIS of STATE of the ART
Literature review on BAR mechanisms

1. Normal cardiac function was always ignored in previous models.
2. Intra-aortic pressure effect on MVCA-related BAR is controversial.

- Is it reasonable to ignore cardiac function in MVCA-related BAR studies?
  Methods: --aortic FE modeling;
  --simulation of AR motion and luminal pressure
- **Results: aortic loadings due to cardiac function are comparable with those in MVCA and failure thresholds [PAPER #1]**

No, the cardiac cycle should be considered

- Does intra-aortic pressure contribute significantly to BAR in MVCA?
  Methods: --aortic burst tests;
  --mini-sled tests to quantify aortic mobility;
  --MVCA reconstruction to estimate pressure-related BAR risk
- **Results: a BAR pressure threshold of 131.8±11.7kPa; intra-aortic pressure significantly affects aortic mobility and causes a high risk of BAR in MVCA . [PAPER #2 and PAPER #3]**

Yes, intra-aortic pressure is critical to BAR in MVCA

- Is it possible to simulate intra-aortic pressure including cardiac function to study MVCA-related BAR mechanisms?
  Methods: --aorta-heart FSI modeling and validation for cardiac cycle;
  --model integration with whole human model;
  --MVCA reconstruction with the integrated model
- **Results: realistic cardiac output in physiological conditions; the *Integrated FSI* model reconstructed injuries consistent with case descriptions and captured cardiac outputs modified by impact loadings. [PAPER #4]**

Yes, it is possible to simulate pressure including cardiac function in MVCA

- What is the BAR mechanism in MVCA?
  Methods: --MVCA reconstructions with the Integrated FSI model and traditional human model;
  --MVCA reconstruction under different initial conditions of intra-aortic pressure;
- **Results: DA constraint by intercostal arteries is critical for BAR modeling; intra-aortic pressure contributed significantly to BAR risk; aortic relative motion (aortic stretch) is the primary BAR mechanism with intra-aortic pressure the secondary mechanism in MVCA.**

1. BAR mechanism is a combination of aortic stretch and intra-aortic pressure;

2. Intra-aortic pressure elevation result from both cardiac function and impact loading;

3. Intercostal artery modeling is critical for BAR simulation.

🟥 **Main result in bold red font**

Figure 1.1: Workflow of the whole study to show the logic relationship among different chapters

- Chapter 4 aims to identify the necessity of considering intra-aortic pressure for BAR researches in MVCAs (see Figure 1.1). Aortic burst tests were conducted with human aortas by pressurizing the aortic lumen to quantify the intra-aortic pressure thresholds. A BAR-related MVCA was reconstructed with FE simulations to obtain intra-aortic pressure levels in crash scenarios. The injury risk of BAR due to pressure was evaluated by comparing the experimental pressure thresholds and numerical pressure information. Additional mini-sled tests with isolated human aorta samples were performed under two different pressurizations. By comparing aortic deflections under the two pressurization conditions, the effects of intra-aortic pressure on aortic mobility were evaluated.

- Chapter 5 aims to develop an aorta FE model able to reproduce the intra-aortic pressure in a realistic cardiac function (see Figure 1.1) so as to include both contributions of injury mechanisms for MVCA-related BAR researches. A FE model was developed for an isolated aorta-heart system with FSI method. A normal cardiac cycle was simulated by modelling ventricular contraction and relaxation to reproduce the blood flow in the aorta. The simulation results were validated against the physiological cardiac outputs in terms of blood flow velocity, blood flow rate, wall shear stress (WSS) at different aortic sections. This isolated aorta FSI model was then integrated with a whole human body model. The integrated model was used to reconstruct a MVCA case involving BAR. The reconstructed injuries were validated against the case injury descriptions. The cardiac outputs of the integrated FSI model during crash were compared with the physiological outputs reproduced by the isolated aorta FSI model.

- Chapter 6 aims to investigate the BAR mechanism during MVCA (see Figure 1.1). Two MVCA cases (a frontal-oblique crash and a lateral crash) involving BARs were reconstructed with a traditional whole human body model and the integrated FSI model. The reconstructed injuries were validated against case injury descriptions. The aortic responses including deformation, stress and strain levels were compared among the structural and FSI simulations. Sub-model scale structural simulations with different initial aortic luminal pressures were performed to quantify the aortic stress and strain levels under these different pressure conditions. The aortic responses were compared among these simulations to identify the possible BAR mechanisms for the case and to justify the necessity of considering the initial physiological intra-aortic pressure for MVCA-related BAR researches.

- Chapter 7 presents a general discussion and conclusion on what has been done in previous chapters.

CHAPTER 2 REVIEW OF INJURY BIOMECHANICS FOR BLUNT AORTIC RUPTURE

2.1 Anatomy of aorta

The aorta is a major artery which conveys oxygenated blood throughout the body. According to anatomical compartment, aorta can be divided into different sections (Figure 2.1): thoracic aorta, abdominal aorta and aortic bifurcation [25]. Thoracic aorta is the segment extending from the heart to the diaphragm while the abdominal portion continues from the diaphragm to the point where aorta bifurcates (i.e. aortic bifurcation). Thoracic aorta completely resides in the mediastinum (Figure 2.2), which is one out of the three compartments of thoracic cavity. The mediastinum is bounded by the pleural cavities, thoracic sternum, thoracic vertebrae and diaphragm.

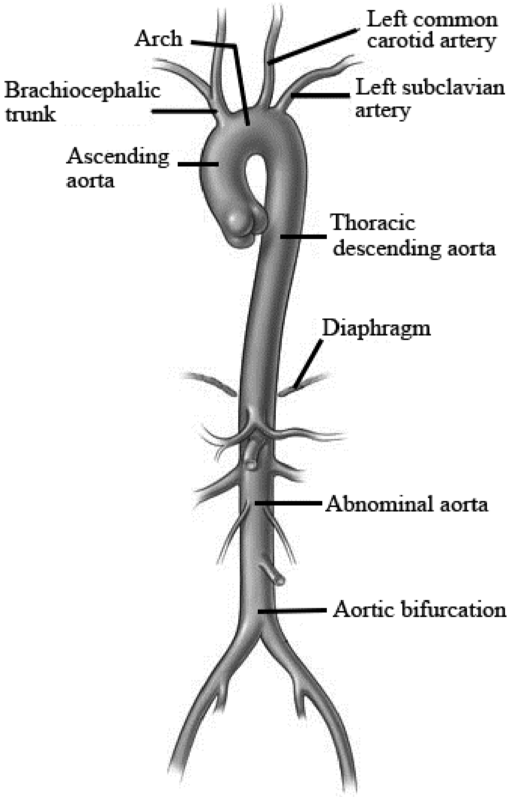
Arch
Left common carotid artery
Brachiocephalic trunk
Left subclavian artery
Ascending aorta
Thoracic descending aorta
Diaphragm
Abnominal aorta
Aortic bifurcation

Figure 2.1: Anatomy of isolated aorta to show different aortic segments and branches (adapted from http://humananatomychart.us/page/10/)

Thoracic aorta can be further divided into different sections (Figure 2.1) according to its course and its blood flow direction: ascending aorta (AA), aortic arch and descending aorta (DA) [25]. The AA begins as AR at the base of LV of the heart. It ascends obliquely, curving forwards and right, behind the sternum to the level of the upper border of the second left costal cartilage. The aortic arch continues from the ascending segment at the pericardial reflection on the aorta. It ascends diagonally back across the left side of the trachea and then descends to the level of fourth thoracic vertebrae. Three branches, known as superior arteries arise from the convex part of aortic arch (Figure 2.1): the brachiocephalic trunk, left common carotid and left subclavian artery. The ligamentum arteriosum, a vestige of the ductus arteriosus, attaches the pulmonary trunk to the inferior curvature of the arch (see Figure 2.2), which is also called as aortic isthmus. Continuing with aortic arch, the DA begins at the lower border of the fourth thoracic vertebrae and ends at the level of twelfth thoracic vertebrae in the diaphragmatic aortic aperture. The DA is confined to the posterior mediastinum and the thoracic spine by intercostal arteries and the reflection of pleura.

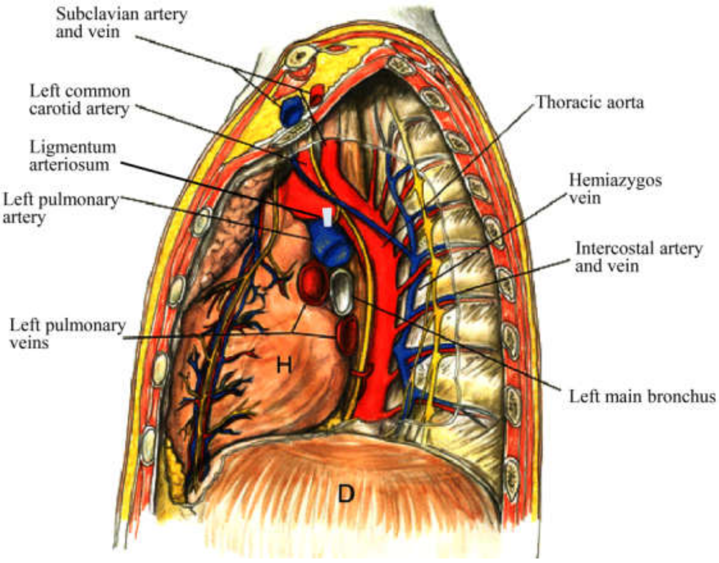
Subclavian artery and vein
Left common carotid artery
Ligmentum arteriosum
Left pulmonary artery
Left pulmonary veins
Thoracic aorta
Hemiazygos vein
Intercostal artery and vein
Left main bronchus
H
D

Figure 2.2: Anatomy of the mediastinum to show the thoracic aorta and its surrounding organs, where H and D correspond to heart and diaphragm (adapted from https://radiologykey.com/mediastinum-and-heart/)

2.2 Structure of aortic wall

The aorta is a tubular structure with two anatomical axes: circumferential (or transverse) and longitudinal (or axial) directions. The aortic wall consists of three distinct layers (displayed in Figure 2.3): tunica interna (the intima), tunica media (the media) and tunica externa (the adventitia). The intima is the innermost layer of the artery, which mainly comprises a layer of endothelial cells in direct contact with the blood flow and a subendothelial layer of connective tissue. The media is the middle and the thickest layer of aorta. It consists of a complex three-dimensional (3D) network of elastin, smooth muscle cells and bundles of collagen fibers. The transverse orientation of the network leads to the circumferentially orientated media able to resist high loadings in this direction. As the outermost layer of the artery, the adventitia is mainly composed of connective elastic and collagen fibers and bundles of smooth muscle tissue. It is surrounded continuously by loose connective tissue, which often makes its outer boundary difficult to define.

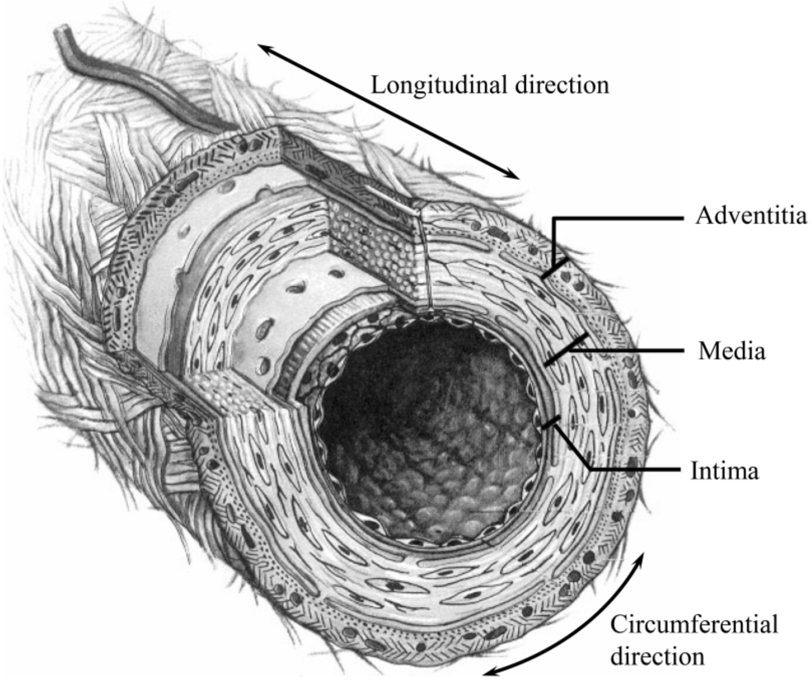

Figure 2.3: Micro-structure of aortic wall (adapted from [26])

2.3 Epidemiologic study of BAR

The first record of BAR-resulted death, caused by an equestrian accident, dates back to the 15th century. Nowadays, BAR is predominantly an injury resulting from road traffic accidents. It accounted for about 15% of the deaths due to MVCAs before seatbelts and airbags were introduced [27, 28]. BAR is the second most common cause of death in blunt trauma patients, after traumatic brain injury [29]. Previous studies estimated that 7500-8000 victims suffered from BAR annually in North America [30, 31]. In the United States, the national BAR incidence was 0.3% among all trauma admissions, with 20-30 persons per million sustaining BAR each year [32]. Autopsy studies suggested 57%-80% of BAR victims die at the accident scene or before arriving at the hospital and more than one-third of the rest survive only for 4 hours under the hospital care [33, 34].

Early studies suggested the frontal impact should be the primary directional force leading to BAR in MVCAs [8, 28] while further researches indicated lateral collisions could also cause significant thoracic injury and BAR [35, 36]. In a prospective study including 274 BAR cases, MVCAs leaded to 81% of the injuries, among which 72% were frontal impacts and 24% side impacts [29]. Previous collision scene investigations found a total velocity change higher than 32km/h and a vehicle intrusion more than 38cm were the two most significant risk factors for MVCAs [37]. Meanwhile, the use of restraint systems was found not to affect BAR incidence [37]. However, later crash data including 15074 occupants during 1998-2006 contradicted the effect of seatbelts on aortic injury [38]. The BAR risk was found to decrease for belted occupants. The risk increased with equivalent impact speed, vehicle intrusion and the occupant's age regardless of the impact direction. In this research, BAR occurred in 1.2% of all the cases and was responsible for 21.4% of all fatalities, with BAR incidence in lateral crashes (2.4%) higher than in frontal impacts (1.1%).

Apart from MVCAs, the other causes of BAR include motorcycle crashes, vehicle-pedestrian impacts, falls and other, the corresponding ratios of which were reported as 13%, 6%, 7% and 6% in another trauma study of 196 patients [39]. Falls from heights greater than 9m could lead to a BAR risk approximately equivalent to that of a 48km/h crash [40]. Deployment of airbags in low speed crashes (16km/h) was also found to cause BAR for passengers not wearing seatbelts [41].

Previous studies proved the victims of BAR always suffered from other accompanied injuries. Among the 274 patients of the prospective study, 51% had closed head injury, 46% multiple rib fractures, 38% lung contusion and 31% pelvic injury [29]. In a study on 63763 patients with blunt trauma, 8.1% of the population had pelvic fractures and 441 persons (1.6%) sustained aortic ruptures [42]. Eighty-six victims suffered from both BAR and pelvic fracture. The incidence of BAR in the pelvic fracture population was twice higher than that in the overall BAR cases.

Aortic injury could occur in various regions. Parmley et al. [27] reported 23% of BAR cases were at AA, 8% at aortic arch and 45% at the peri-isthmus. Creasy et al. [43] suggested a much higher incidence (90%) at the aortic isthmus distal to the origin of the left subclavian artery. Later studies further proved the victims with classic isthmus laceration accounted for up to 94% of all BAR, among which 93% were complete transection [36].

2.4 Aortic injury mechanisms

There are numerous mechanisms proposed in literature for BAR, including inertia-based, pressure-based, stretch-based and other hypothesis.

2.4.1 Inertia-based

Letterer et al. [44] were the first to propose inertial loading as a possible mechanism of aortic rupture. They postulated the downward traction of the heart due to inertia during falls leaded to the aortic root avulsion. Hass et al. [45] further suggested the differential acceleration of different thoracic organs within the mediastinum caused BAR in aircraft accidents. However, Roberts et al. [46] argued against inertia mechanism since great vessel ruptures were also found in cases without acceleration loadings. This argument was further supported by other following studies in which victims withstood accelerations higher than 45g without aortic injuries during sled tests [47] or racecar competition crashes [48]. In a more recent study, Forman et al. [12] conducted a series of high-speed sled tests with minimal thoracic compression (maximum value 7.0±3.1%). The tests resulted in spinal accelerations up to 80g for 20ms while no macroscopic aortic injuries were found, seemingly reinforcing the idea that inertial loading should not be considered as a primary mechanism for BAR.

2.4.2 Pressure-based

Multiple researches have been conducted to back up pressure being a primary mechanism. In a 100-year-ago study, Oppenheim et al. [49] concluded the overpressure (400kPa) in aorta was responsible for aortic tears. Following researches speculated the pressure elevation resulting from acceleration could cause fluid shock wave in the aorta and finally vessel explosive outburst [50, 51]. Lundevall et al. [8] proposed water-hammer (see Figure 2.4) as another pressure-related mechanism, speculating the sudden occlusion of blood flow leaded to significant pressure arise in aorta. Bass et al. [11] made a series of aortic burst experiments in vivo and in situ with an average rate of 730kPa/s, resulting in longitudinal aortic tears in more than half of the samples. With their Weibull survival analysis against burst pressures, they proposed a 50% aortic tear risk at pressure 101kPa for overall populations (67.7±12.7) and 120kPa for subjects younger than 68 years. However, these pressure-resulted mechanisms were also contradicted by other researches. Shah et al. [52] and Hardy et al. [10] considered overpressure unlikely to cause clinical related BAR since typical failure of aorta was a transverse tear rather than a longitudinal tear, primary failure pattern in aortic bursts. Moreover, in some cadaver sled tests [12] or pendulum-impact tests [15], no BAR was recorded even with intra-aortic pressure levels up to 160kPa which was much higher than the assumed pressure level of 50% injury risk [11]. These arguments appear to indicate the excessive blood pressure could be a secondary BAR mechanism at most.

2.4.3 Stretch-based

Rindfleisch [53] proposed for the first time stretch deformation as a significant factor for aortic trauma after analyzing the data of horse-riders falling accidents. Almost 90 years later, Mohan and Melvin [54] reproduced aortic failure in biaxial stretch tests with an average failure stress of 1.97MPa. In the in situ human cadaver tests under dynamic and quasi-static configurations, Hardy et al. [10] reproduced all the aortic injuries at peri-isthmus. To be noted, they inverted the cadavers during the experiments to generate their so-called anatomically correct positions for the mediastinal organs. They proposed the tethering of DA by the pleura to be the primary contribution to BAR in the study rather than the aortic intraluminal pressure or the body acceleration. In the tensile tests with entire thoracic aortas conducted by Shah [55], longitudinal tensile stretch was deemed to cause aortic ruptures, since the most frequent transverse aortic tears coincided with the predominant injury direction in MVCAs. Hardy et al. [9] conducted additional cadaver tests under various blunt loadings with human trunk inverted, the same as their previous experimental configurations [10]. Seven out of the eight cadavers resulted in clinically relevant BAR. The authors concluded the aortic longitudinal stretch resulting from thoracic compression to be the primary cause of BAR, even though they did not validate their so-called anatomically realistic positions of thoracic organs with cadaver-inverting protocols. Furthermore, it is also questionable whether the inversion configurations would impose pre-loading on aortic arch and increase BAR risks.

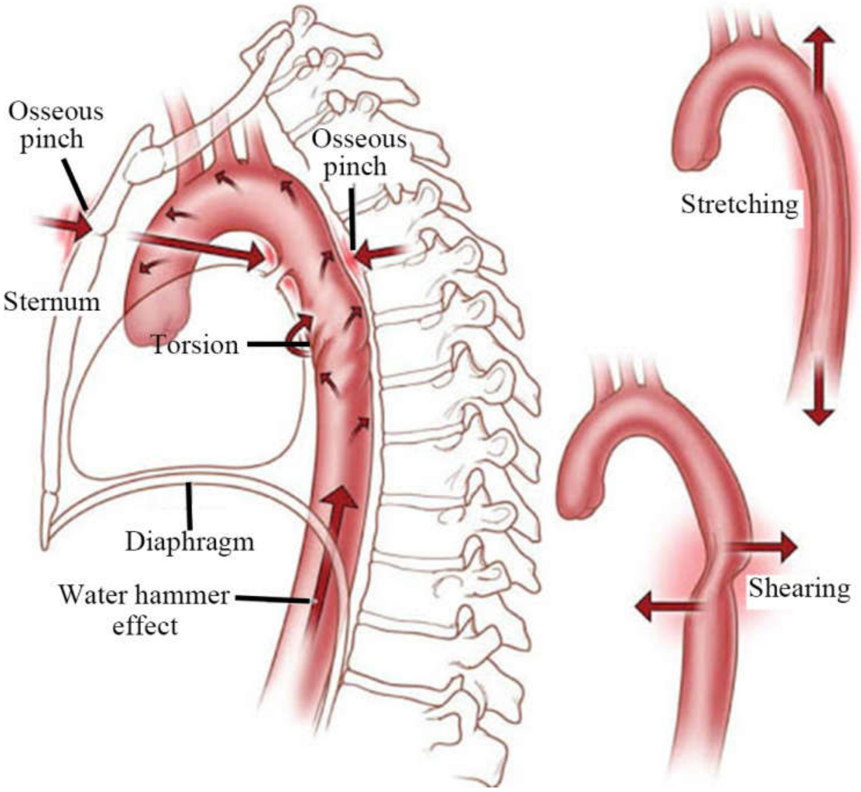

Figure 2.4: Schematic diagram of BAR mechanisms (adapted from [7])

2.4.4 Others

Besides the three categories of BAR hypothesis, Marshall [56] proposed the squeezing of aorta by pleura due to impact as an alternative mechanism of BAR in MVCAs. Cammack et al. [57] postulated the torsional force of aorta would result from differential motions among the mediastinal organs and should contribute to BAR under the deceleration loadings recorded in collisions (see Figure 2.4). Gotzen et al. [58] proposed the impact direction to the chest and the resulting thoracic deformation should be determinant to BAR mechanisms. They found that the heart and aortic arch would be forced to move upwards posteriorly and to the left, if the impact to the chest oriented from right ventro-caudal to left dorso-caudal. The relative motion between the heart and DA could lead to stretching and shearing of the aorta at isthmus (see Figure 2.4). Crass et al. [59] proposed the osseous pinch theory, indicating the aortic circumferential tears could result from the impingement between the upper ribs and thoracic spine due to sudden deceleration and thoracic compression (see Figure 2.4). Contradicting with this hypothesis, the BAR incidence did not seem to vary regardless of rib or sternum fractures [60, 61]. Sevitt et al. [62] postulated the ligamentum arteriosum should be critical to BAR since peri-isthmus, the location where ligamentum arteriosum tethers the aortic arch with pulmonary artery, is the most frequent site of aorta. In contrast, Shah et al. [52] and Hardy et al. [10] suspected the significant contribution of ligamentum arteriosum to BAR, since pulmonary artery did not turn to be as vulnerable as peri-isthmus in MVCAs.

2.5 Previous research approaches to simulate BAR mechanisms

2.5.1 Experimental studies

Multiple experiments were conducted with animal or human cadaver samples. Coermann et al. [63] conducted frontal sled impacts on 6 unembalmed human cadavers at an average speed of 15.5m/s to produce typical aortic isthmus laceration. Two aortic ruptures succeeded to happen during the experiments when a less energy absorbing steering wheel and a thinner hub were utilized. Nevertheless, only one of the aortas was ruptured at isthmus with the other one injured at proximal peri-isthmus. Another set of frontal impacts were designed by Kroell et al. [13], where 23 unembalmed human cadavers were impacted at their mid-sternums with a mass of 19.5kg or 23.1kg at a speed range of 4.0-10.0m/s (displayed in Figure 2.5). Before the tests, the aortas were pressurized without pressure levels reported. Despite a considerable intra-aortic pressure (up to 210kPa) recorded during impacts, only two aortic failures were reproduced. In another pendulum impact test at a velocity of 5m/s on a primate chest, a substantial chest compression with high intra-thoracic organ deformations was witnessed in flash X-ray cinematography [64]. The entrapment of aorta by heart and spine was postulated to cause aortic tears in this study.

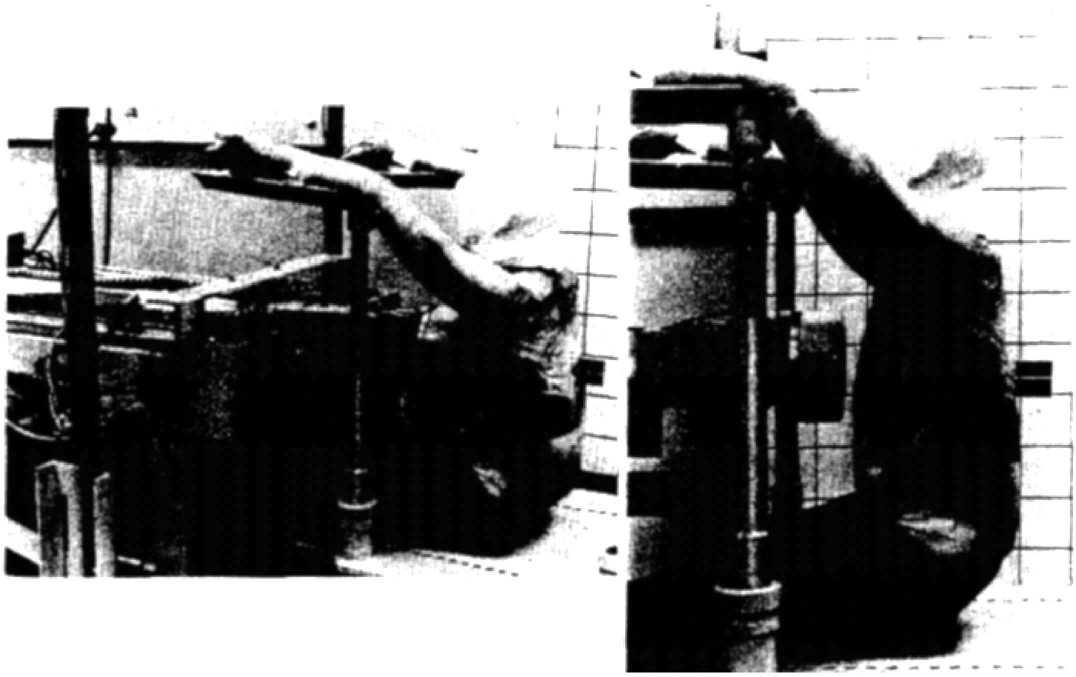

Figure 2.5: Experimental setup for frontal impact at mid-sternum of human cadaver (adapted from [13])

Aortic injuries were reproduced at aortic root and superior branches in the experiments with live anesthetized canines, which was impacted by a hydraulic hammer with speeds up to 14m/s [65](see Figure 2.6). Frontal impact on sternum resulting in chest compression and downward heart motion was considered necessary to reproduce aortic trauma in this study. Viano et al. [14] conducted 44 blunt lateral impacts on the chests and abdomens of 14 unembalmed human cadavers. A pendulum of 150mm diameter and 23.4kg mass was launched with speeds of 4.5, 6.7 or 9.4 m/s to initiate the impacts. No aortic injury was reported, though the objective of this study was achieved by generating the human thoracoabdominal response corridors in blunt side impacts.

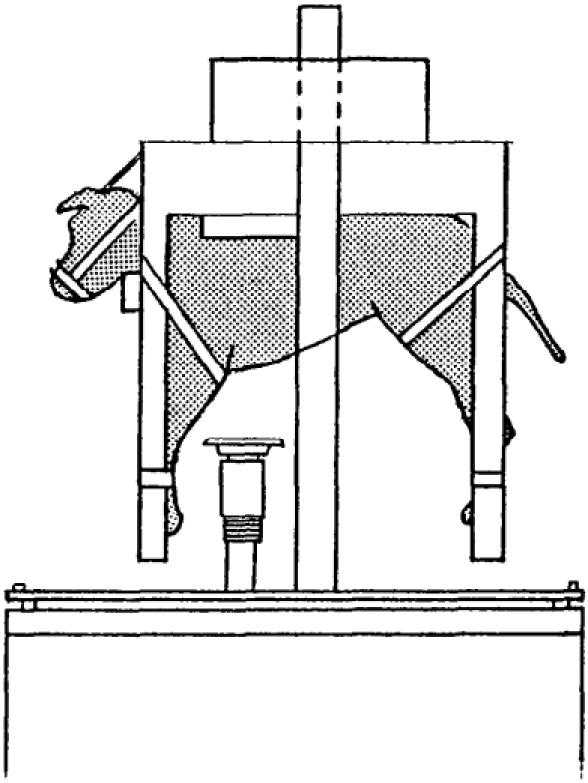

Figure 2.6: Initial experimental configuration for canine thoracic impact (adapted from [64])

Cavanaugh et al. [66, 67] recorded 5 aortic traumas in 17 sled side impacts for thoracic injury tolerance studies. In these studies, the aortas were pressurized to 100mmHg and the sleds were accelerated to speeds of 6.7 to 10.5m/s. It was postulated that the relative motion between mobile AA and constrained DA should result from the inertial loading due to substantial deceleration and result in aortic tears at isthmus. Cavanaugh et al [68] reanalyzed their previous tests to assess possible injury indexes and their predictive abilities. By multivariate analysis, the best predictors of BAR were considered to result from the combination of upper sternum postero-anterior acceleration with average spine acceleration [67] and T12 vertical acceleration with VCmax [69], Cmax[13] , and average spine acceleration. By logistic regression analysis, BAR presence was found to correlate well average spine acceleration, peak acceleration of the eighth rib on the unstruck side and VCmax.

Bass et al. [11] designed in vivo and in situ pulsatile pressure tests on 11 entire human aortas (displayed in Figure 2.7) with pressure loading rates obtained in 4 deceleration sled tests. These sled tests were conducted at a velocity of 13m/s on human cadavers, during which the aortas were pressurized with a pressure of 16kPa and the pressure change due to collisions were also recorded. In this study, Bass et al. [11] concluded a 50% risk of aortic failure at a stress of 852 kPa and 426 kPa in the circumferential and longitudinal direction. They also forwarded an intra-aortic pressure threshold of 101 kPa for 50% BAR risk.

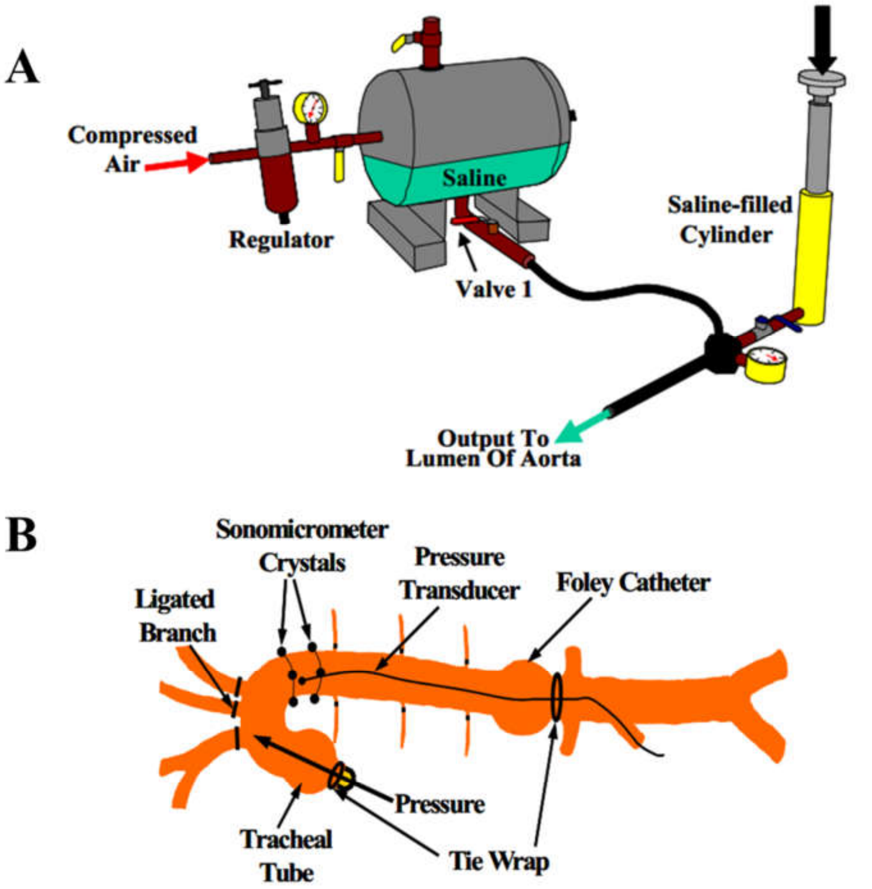
A
Compressed Air
Regulator
Saline
Valve 1
Saline-filled Cylinder
Output To Lumen Of Aorta
B
Sonomicrometer Crystals
Pressure Transducer
Foley Catheter
Ligated Branch
Pressure
Tracheal Tube
Tie Wrap

Figure 2.7: Experimental setup of entire aorta burst: A) schematic of pressurization apparatus; B) Schematic of instrumented whole aorta for in vitro pressure impulse testing (adapted from [11])

Forman et al. [12] investigated the inertial mechanism for BAR by conducting 9 sled tests with human cadaver trunks. All the cadavers were placed in drums filled with beads to limit thoracic deformation so as to isolate the inertial loadings. Despite the averaged peak accelerations up to 169g, no aortic tear occurred in the tests, in which maximum chest compression and intra-aortic pressure were 7% and 177kPa. The authors postulated chest compression was necessary for reproducing BAR. As previously mentioned, Hardy et al. [9] carried out various blunt impacts on

8 unembalmed human cadavers which were inverted during the tests. They assumed the mediastinal organs were located at more anatomically correct positions with the upside-down configuration. High-speed bi-plane x-ray was used to visualize and record the aortic motions within the trunk. Seven out of the 8 cadavers were subjected to aortic injuries, all of which occurred transversely at aortic isthmus. The authors concluded that thoracic deformation should be the principal cause of BAR with intra-aortic pressure or whole body acceleration secondary at most. More recently, Viano et al. [15] reanalyzed their pendulum impact tests on 11 unembalmed human cadavers which were performed in 1986. They owed the absence of BAR to the unrealistic aortic positions since the cadavers were not inverted as Hardy et al. [9] invented. However, no further efforts were made to provide any experimental data to validate the hypothesis. Probably, the cadaver inversion might induce artificial pre-loadings to the aorta through aortic branches, resulting in higher risks of BAR under this condition.

The possible limitations of experimental simulations:

- *Tremendous economical and time expenses;*
- *Absence of human physiological activities (e.g. cardiac cycle);*
- *Difficulty in reproducing MVCA-relevant BARs;*
- *Difficulty in providing injury-related indexes (e.g. aortic stress and strain).*

2.5.2 FE human body models

FE human body modeling is another method to investigate BAR mechanisms in addition to cadaver tests. Shah et al. [70] developed a 50 percentile human thoracic model (displayed in Figure 2.8) with detailed internal organs to BAR studies. The aorta in this work was modeled as hollow tube and with linear elastic material. Aortic blood pressure was included by imposing an uniform intro-aortic pressure. Pendulum thoracic impacts from various directions were performed and the aortic isthmus was suggested as the most vulnerable site of BAR regardless of impact direction. The right-sided impact was postulated to cause higher levels of aortic injuries compared to other impact directions. Following their previous studies, Shah et al. [71] developed a whole human body model, the so-called ‘WSHBM’ model (displayed in Figure 2.9), by integrating a detailed thorax model, an abdomen model and a shoulder model. After the WSHBM model was validated against experimental data of thoracoabdominal impacts [71], it was used to reconstruct a real-world car-to-car crash accident involving BAR and archived in the Crash Injury Research and Engineering Network (CIREN) center [72]. Similar approaches were used to reconstruct another four collision accidents related to BAR with the WSHBM model [18]. Aortic peri-isthmus displayed highest maximum principal strain and longitudinal stress in lateral collision simulation while junction between ascending segment and aortic arch resulted in highest maximum principal strain and longitudinal stress in frontal crashes. Although the FE modelling above displayed its advantages over cadaver tests in investigating BAR mechanisms under various loading conditions, these FE models still remained to be validated in more detailed organ levels before being considered to be reliable.

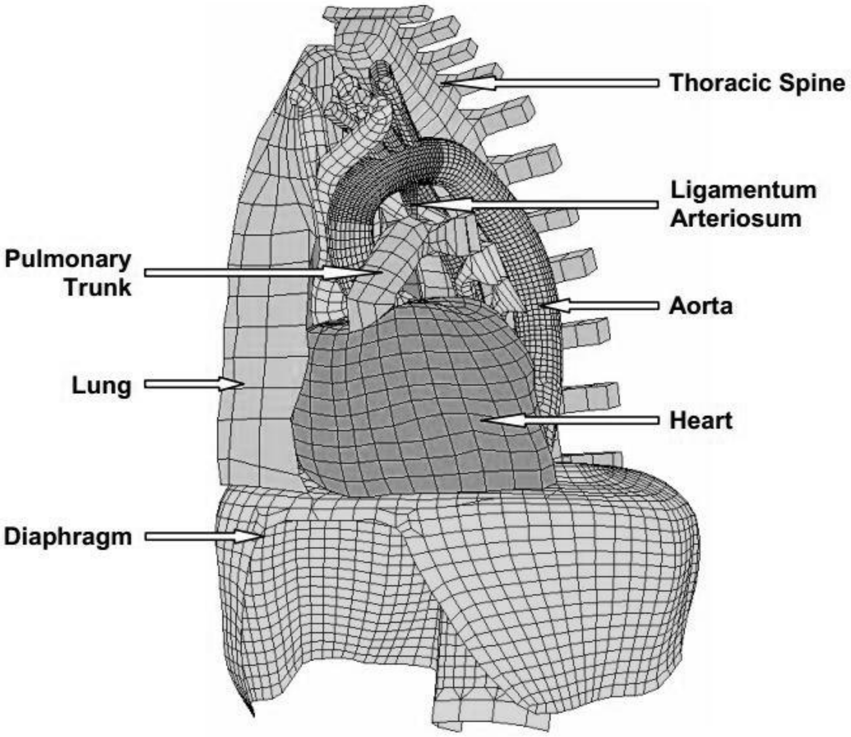

Figure 2.8: Thoracic FE model by Shah et al. (adapted from [70])

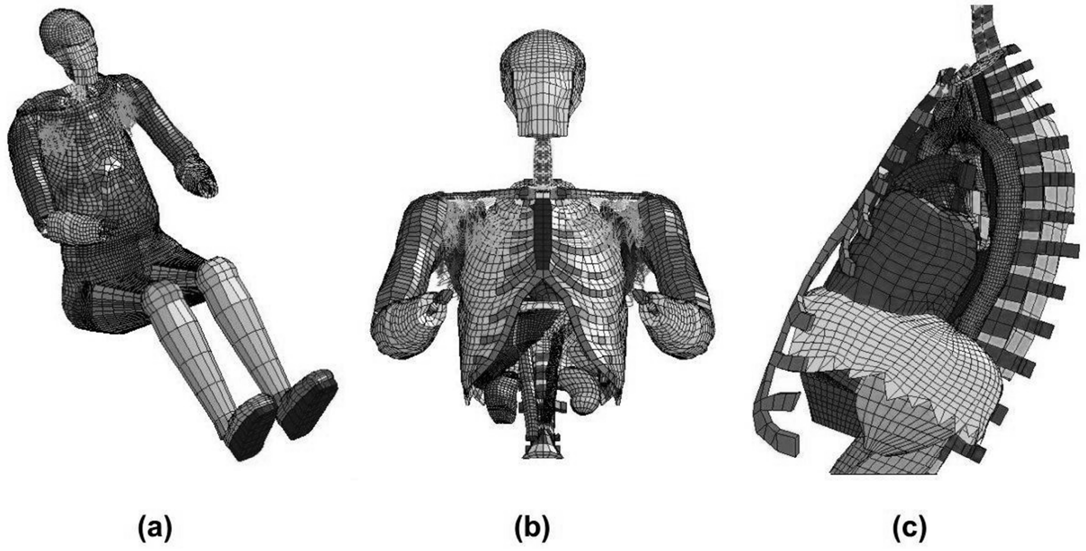

Figure 2.9: The Wayne State Human Body Model (WSHBM): (a) global view of the model, (b) upper trunk (c) sagittal section of the chest with the shoulder, ribcage and the left lung removed to view the mediastinum contents (adapted from [71])

Lee and Kent [22] used an isolated aortic FE model (displayed in Figure 2.10) to evaluate the blood hydrodynamic effects on BAR with FSI approach. The aortic wall was modeled with an anisotropic viscoelastic material consisting of 2 sets of fibers, the constitutive parameters of which were reconstructed from experimental data. A physiological pulsatile blood flow was applied to the aortic inlet, branches and outlet as mechanical quantity references, while parametric impact pulses obtained from frontal sled tests were prescribed as aortic boundary conditions. A maximum pressure of 280kPa was recorded in the simulation and postulated to cause BAR alone at ascending aorta. The abrupt blood flow was suggested to initiate aortic intimal tears at the dynamic self-pinch region. The tears were oriented transversely due to the high shear flow of blood.

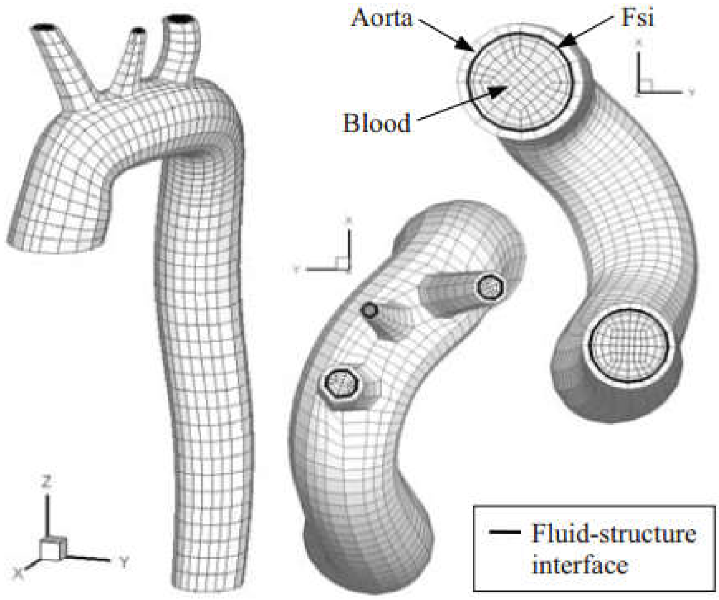

Figure 2.10: In vitro FE model of human aorta (adapted from [22])

More recently, Aditya [21] reconstructed 8 vehicle crash cases involving BAR (see Table 2.1) and obtained from CIREN with a similar approach in [72]. In seven of the eight reconstructions, aortic injury was located at the isthmus with the average peak tensile isthmic strain 18±6% at 20±7 mm distal to the left clavian artery. Furthermore, a design of computer experiments was performed to study the effects of key factors on aortic average maximum principal strain and the maximum intra-aortic pressure. The key factors included principle direction of force, impact position, impact angle, impact velocity and the striking vehicle's bumper profile. The aortic strain was found to decrease significantly with increasing principal direction of force but to increase with increasing impact velocity. The force direction of 270 degrees resulted in highest aortic strain while the intra-aortic pressure decreased with increasing principal force direction (from 270 degrees).

The possible limitations of previous numerical simulations:

- *Ignoring human physiological cardiac function;*
- *Being unable to simultaneously include both injury contributions to BAR (e.g. either the aortic blood flow or the intra-thoracic aortic interactions were ignored).*

Table 2.1 Summary of simulation setup in the 8 nearside lateral impact reconstructions (adapted from [21])

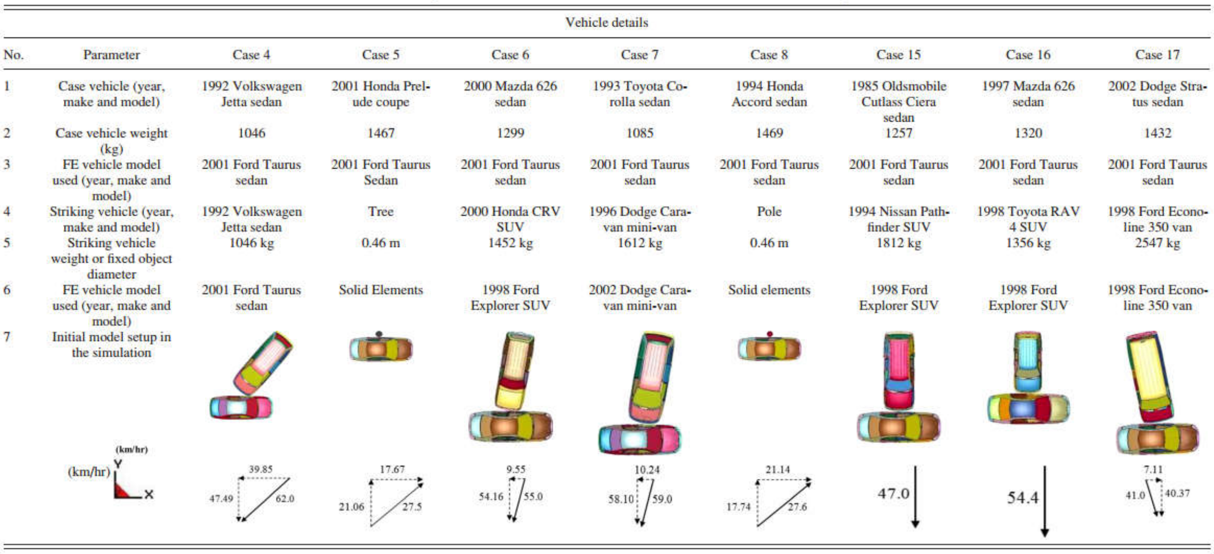

		Vehicle details							
No.	Parameter	Case 4	Case 5	Case 6	Case 7	Case 8	Case 15	Case 16	Case 17
1	Case vehicle (year, make and model)	1992 Volkswagen Jetta sedan	2001 Honda Prelude coupe	2000 Mazda 626 sedan	1993 Toyota Corolla sedan	1994 Honda Accord sedan	1985 Oldsmobile Cutlass Ciera sedan	1997 Mazda 626 sedan	2002 Dodge Stratus sedan
2	Case vehicle weight (kg)	1046	1467	1299	1085	1469	1257	1320	1432
3	FE vehicle model used (year, make and model)	2001 Ford Taurus sedan	2001 Ford Taurus Sedan	2001 Ford Taurus sedan	2001 Ford Taurus sedan	2001 Ford Taurus sedan	2001 Ford Taurus sedan	2001 Ford Taurus sedan	2001 Ford Taurus sedan
4	Striking vehicle (year, make and model)	1992 Volkswagen Jetta sedan	Tree	2000 Honda CRV SUV	1996 Dodge Caravan mini-van	Pole	1994 Nissan Pathfinder SUV	1998 Toyota RAV 4 SUV	1998 Ford Econoline 350 van
5	Striking vehicle weight or fixed object diameter	1046 kg	0.46 m	1452 kg	1612 kg	0.46 m	1812 kg	1356 kg	2547 kg
6	FE vehicle model used (year, make and model)	2001 Ford Taurus sedan	Solid Elements	1998 Ford Explorer SUV	2002 Dodge Caravan mini-van	Solid elements	1998 Ford Explorer SUV	1998 Ford Explorer SUV	1998 Ford Econoline 350 van
7	Initial model setup in the simulation								
	(km/hr)	39.85 47.49 62.0	17.67 21.06 27.5	9.55 54.16 55.0	10.24 58.10 59.0	21.14 17.74 27.6	47.0	54.4	7.11 41.0 40.37

CHAPTER 3 AORTIC STRESS LEVEL DURING CARDIAC CYCLE

3.1 Introduction

Aortic wall stress was often used as an index to quantify the aortic failure threshold in previous studies. Mohan et al. [73] performed a series of uniaxial tension tests with the samples obtained from human descending mid-aorta aortas. The aortic ultimate (failure) stress was reported respectively for longitudinal and transverse direction during quasi-static and dynamic stretch tests. The reported data were listed in Table 3.1. Mohan et al. [54] also performed biaxial inflation tests with human aortic samples. The ultimate stress was reported as 1.14±0.32MPa and 1.96±0.6MPa respectively for quasi-static and dynamic tests. Shah et al. [52] conducted dynamic equibiaxial stretch tests with cruciate samples which were excised from the human ascending, peri-ishtmic and descending aortas. The aortic failure stress was reported as 2.07±1.11MPa and 1.95±0.89MPa respectively for the 1-m/s and 5-m/s stretch test series. García-Herrera et al. [74] performed uniaxial quasi-static stretch tests with fresh human aortic samples Figure 3.1. The aortic failure stress was reported as 4.10±0.27MPa and 1.91±0.44MPa respectively for circumferential and longitudinal directions.

Table 3.1 Summary of aortic ultimate stress for longitudinal and transverse direction during quasi-static and dynamic stretch tests [73]

Ultimate stress (MPa)	Quasi-static		Dynamic (~100 sec.$^{-1}$)	
	Longitudinal	Transverse	Longitudinal	Transverse
Mean	0.147	0.172	0.359	0.507
S.D	0.091	0.089	0.204	0.329

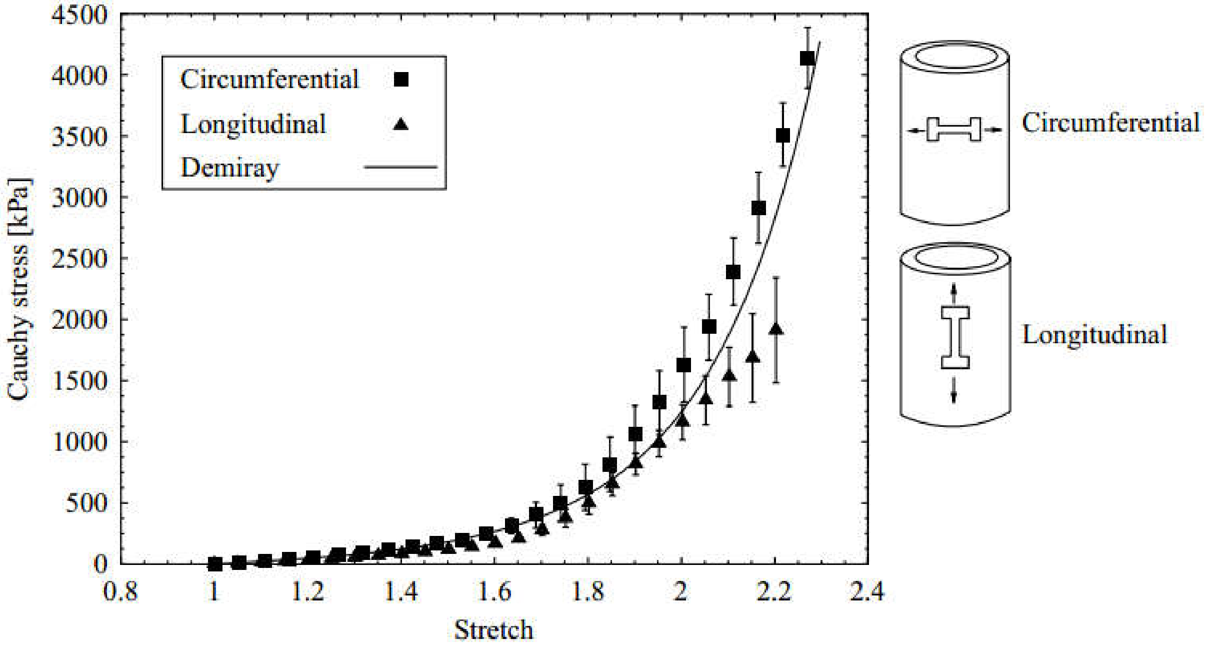

Figure 3.1 Experimental and computed results of Cauchy stress versus stretch during aortic uniaxial stretch test (adapted from [74])

Aorta was enclosed in thoracic cavity by other surrounding organs, but aortic stress level is challenging to be recorded experiment with intact mediastinum anatomy for MVCAs or equivalent loading conditions. Thanks to FE modeling approach, aortic stress loading under MVCAs was reported in a limited number of studies. Richens et al. [17] simulated a chest impact with a simplified thoracic model where the DA was fixed on the rigid spine without superior aortic suspendings. The aortic blood was modeled with an elastic material and with Lagrange solid elements. A peak VonMises stress of 1.5MPa was observed at the peri-isthmic region. Siegel et al. [19] reconstructed 10 cases of vehicle lateral impacts with full scale vehicle FE models and a whole human FE model (see Figure 3.2). The aortic blood was not modeled but an airbag of 120mmHg was filled in the aortic lumen to mimic the blood pressure. The aortic isthmus maximum stresses ranged from 1.1~3.2MPa and the aortic longitudinal strains ranged from 8.2%~48.5% for the group of reconstructed accident cases. Han et al. [75] investigated aortic stress levels for aged populations during thoracic frontal and lateral impacts. The aorta was simulated with shell elements and a linear-elastic material. Aortic blood pressure was ignored in the model. The aortic peak stresses ranged from 0.92~1.29MPa and 0.62~0.83MPa respectively during frontal and lateral impacts (displayed in Figure 3.3).

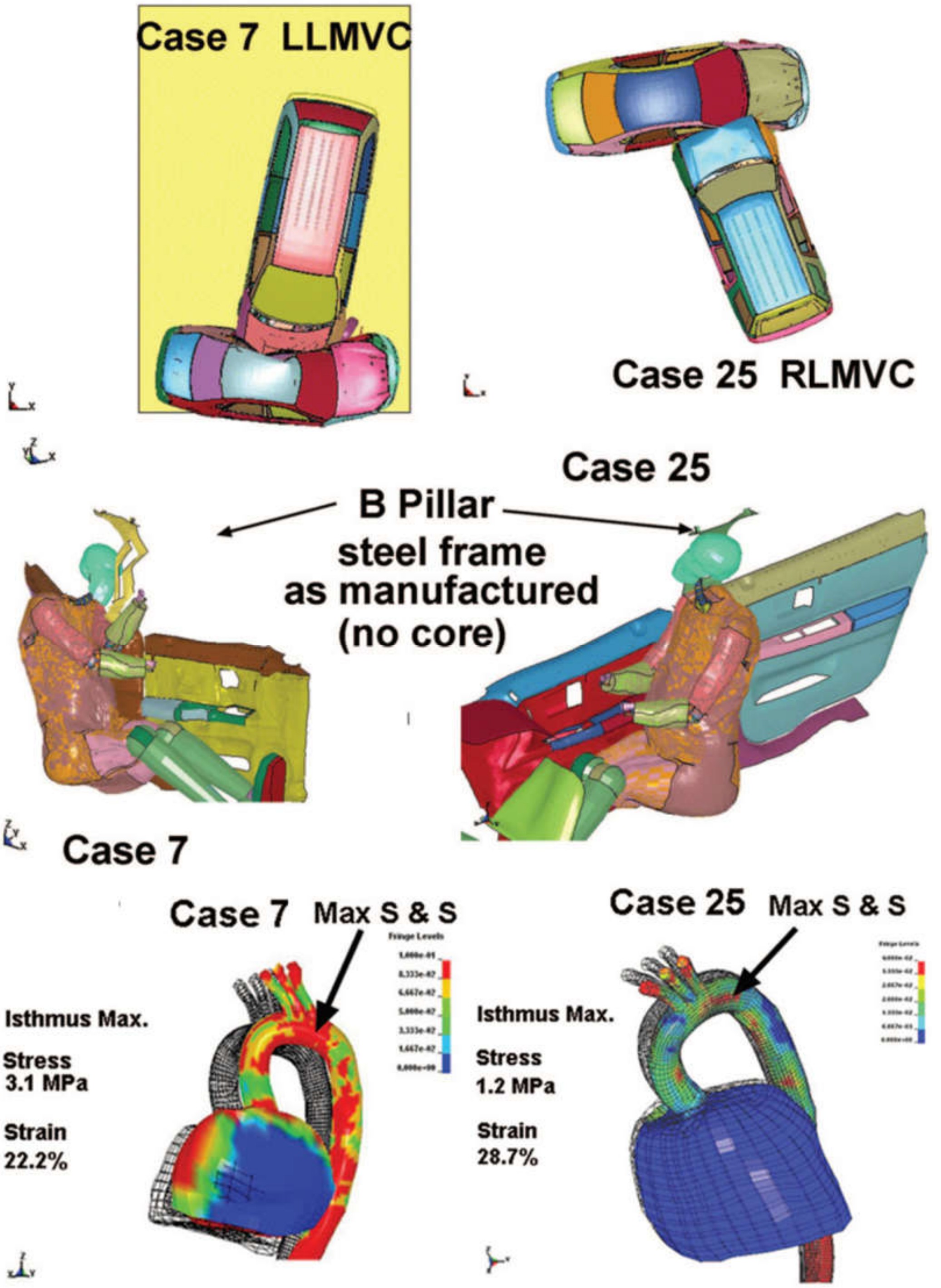
Case 7 LLMVC
Case 25 RLMVC
Case 25
B Pillar
steel frame
as manufactured
(no core)
Case 7
Case 7 Max S & S
Fringe Levels
Isthmus Max.
Stress
3.1 MPa
Strain
22.2%
Case 25 Max S & S
Isthmus Max.
Stress
1.2 MPa
Strain
28.7%

Figure 3.2 Aortic stress levels reconstructed from vehicle lateral impact cases (adapted from[19])

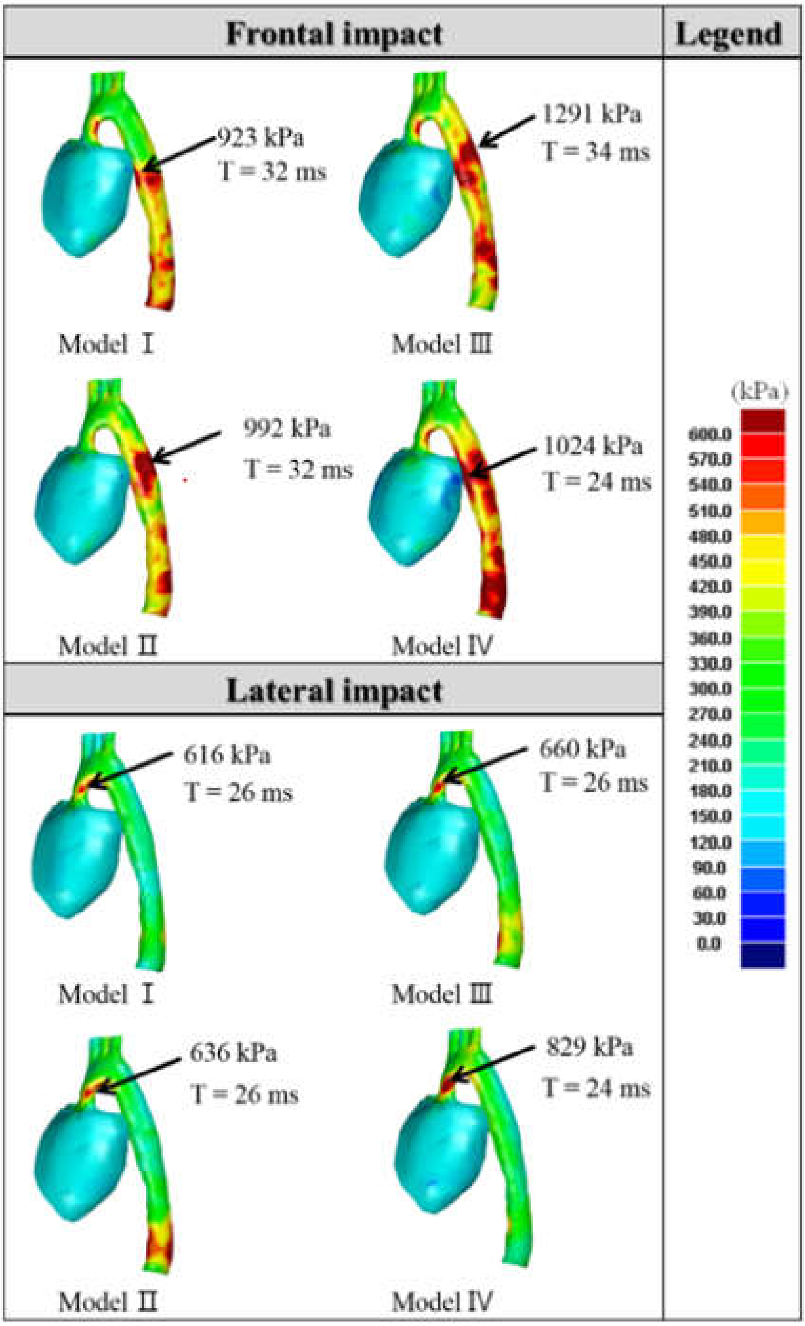
Frontal impact
Legend
923 kPa
T = 32 ms
1291 kPa
T = 34 ms
Model Ⅰ
Model Ⅲ
992 kPa
T = 32 ms
1024 kPa
T = 24 ms
Model Ⅱ
Model Ⅳ
Lateral impact
616 kPa
T = 26 ms
660 kPa
T = 26 ms
Model Ⅰ
Model Ⅲ
636 kPa
T = 26 ms
829 kPa
T = 24 ms
Model Ⅱ
Model Ⅳ
(kPa)
600.0
570.0
540.0
510.0
480.0
450.0
420.0
390.0
360.0
330.0
300.0
270.0
240.0
210.0
180.0
150.0
120.0
90.0
60.0
30.0
0.0

Figure 3.3 Maximum principal stress contours of the heart and the aorta at the time when the maximum stress was generated in each model (adapted from [75])

Among these available studies to quantify aortic loadings, realistic cardiac cycle was never simulated. In other words, the aortic stress level resulting from cardiac function was commonly ignored during these previous BAR researches. The aortic responses due to cardiac cycle can be attributed to the effects of blood pressure and heart traction. However, these previous works failed to quantify the aortic stress level from cardiac cycle and to answer whether the stress level was ignorable for BAR prediction compared with that from impact loadings. The following sections will deal with these issues by quantifying the aortic stress level under the effects of blood pressure and ventricular traction.

3.2 Article #1: Investigating Heartbeat-Related In-Plane Motion and Stress Levels Induced at the Aortic Root

This article "Investigating Heartbeat-Related In-Plane Motion and Stress Levels Induced at the Aortic Root" was submitted to the International Journal of Cardiovascular Imaging on 21th March, 2018. It was still under review at the time this thesis was written.

Wei Wei[1,*], Morgane Evin[1], Stanislas Rapacchi[2], Frank Kober[2], Monique Bernard[2], Alexis Jacquier[2], Cyril J.F. Kahn[1], Michel Behr[1]

[1] *Aix-Marseille Université, IFSTTAR, LBA UMR T24, Marseille, France*

[2] *Aix-Marseille Université, CNRS, CRMBM UMR 7339, Marseille, France*

Abstract

Purpose: The axial motion of aortic root (AR) due to ventricular traction was previously suggested to contribute to ascending aorta (AA) dissection by increasing its longitudinal stress, but AR in-plane motion effects on stresses have never been studied. The objective is to investigate the contribution of AR in-plane motion to AA stress levels.

Methods: The AR in-plane motion was assessed on magnetic resonance imagining data from 25 healthy volunteers as the movement of the AA section centroid. The measured movement was prescribed to the proximal AA end of an aortic finite element model to investigate its influences on aortic stresses. The finite element model was developed from a patient-specific geometry using LS-DYNA solver and validated against the aortic distensibility. Fluid-structure interaction (FSI) approach was also used to simulate blood hydrodynamic effects on aortic dilation and stresses.

Results: The AR in-plane motion was 5.5±1.7mm with the components of 3.1±1.5mm along the direction of proximal descending aorta (PDA) to AA centroid and 3.0±1.3mm perpendicularly under the PDA reference system. The AR axial motion elevated the longitudinal stress of proximal AA by 40% while the corresponding increase due to in-plane motion was always below 5%. The stresses at proximal AA resulted approximately 7% less in FSI simulation with blood flow.

Conclusions: The AR in-plane motion was comparable with the magnitude of axial motion. Neither axial nor in-plane motion could lead to AA dissection. It is necessary to consider the heterogeneous pressures related to blood hydrodynamics when studying aortic wall stress levels.

Keywords: Aortic Root Motion, Magnetic Resonance Imagining, Aortic Stress, Finite Element, Fluid-Structure Interaction

3.2.1 Introduction

Aortic dissection is rare but a potentially life-threatening illness. Apart from hypertension and aortic dilation [76], the aortic root (AR) motion has also been proposed to be another factor leading to dissection [77, 78]. During the cardiac cycle, the aortic annulus is towed due to ventricular traction in systole and is relaxed in diastole. The traction force induces a spatial movement of the aortic annulus and is transmitted to the ascending aorta (AA). The AR motion has been proved to alter in parallel with such cardiovascular pathologies as left ventricular hypokinesis and aortic insufficiency [77]. Since supra-aortic vessels were relatively constrained compared to AA, different AR motions would bring about different levels of aortic wall stress, which was proposed as a risk prediction index for aortic dissection [79] and aortic aneurysm [80].

A mean value of 8.9mm (range 6.4-11.3mm) for aortic motion was observed along the lumen longitudinal direction with cine-magnetic resonance imaging (MRI) studies in healthy subjects [81]. The aortic downward displacement was also reported to range between 0% and 49% of the sino-tubular junction diameter in patients with coronary artery diseases [77]. In contrast, the mean in-plane (perpendicular to the lumen) displacement of AA was respectively reported as 5.2±1.7mm for patients with chronic aortic dissection type B [82] and 6.7±1.8mm for the young healthy volunteers [83]. However, the component displacements in the anterior-posterior or the lateral direction were not mentioned in both studies.

Aortic finite element (FE) models were previously used to evaluate the AR downward [77, 78, 84] and twisted [77, 78] motion effects on proximal AA stress levels. Studying the influences of AR in-plane movement is however limited. A lack of model validation against physiological data might also undermine the accuracy of aortic stress. Moreover, an uniformly distributed loading was assumed on the aortic wall in these previous studies while the simulation fidelity could benefit from considering the inhomogeneous pressure ambient due to blood flow.

Therefore, the aim of our study was threefold. Firstly, in order to add additional knowledge to AR physiological motion, the in-plane components of heartbeat-related AR displacement will be evaluated in healthy volunteers with MRI data. Secondly, the fluid-structure interaction (FSI) will be simulated between the aortic wall and blood to assess the fluid dynamic effects on aortic stress levels. Finally, to determine the in-plane motion effects on AA dissection risks, the AA stress levels will be studied under different AR motions with a validated FE model.

3.2.2 Materials and methods

Volunteers

The study was approved by the local ethics committee (CPP Sud Méditerranée I, Marseille, ID RCB 2012-A01093-40) and the written informed consent was granted by each volunteer. Twenty-five volunteers (15 men and 10 women, mean age 30.4±9.7 years, mean height 175.8 ± 7.6cm, mean weight 65.8±13.0kg) were recruited into this evaluation and the candidates had to match the following criteria: no history of cardiovascular disease, hypertension, diabetes or hypercholesterolemia.

Image acquisition and evaluation

The image acquisition was performed for all the subjects during a breath-hold with a 1.5T MRI scanner (Avanto VB17, Siemens, Erlagen, Germany) under a protocol as previously described in [85]. A stack of segmented steady-state free precession (SSFP) bright blood images were acquired in axial and oblique sagittal planes (Figure 3.4) to assess the aortic slice segmentation.

SSFP cine images were subsequently obtained at three different levels (AA together with the proximal descending aorta (PDA) at the level of pulmonary trunk, the distal descending aorta 3cm above the diaphragm (DDA) and above the coeliac trunk (CA)) perpendicular to the aortic lumen (Figure 3.4) with the following parameters: TR=21.7ms to 24.7ms, TE=1.36ms to 1.55ms, α=65°, recFOV=210mm×263mm to 280mm×340mm, slice thickness=7mm, pixel size=1.26mm×1.26mm to 1.68 mm×1.68mm. It is worth noting that only the images at AA section were used to evaluate the AR in-plane motion.

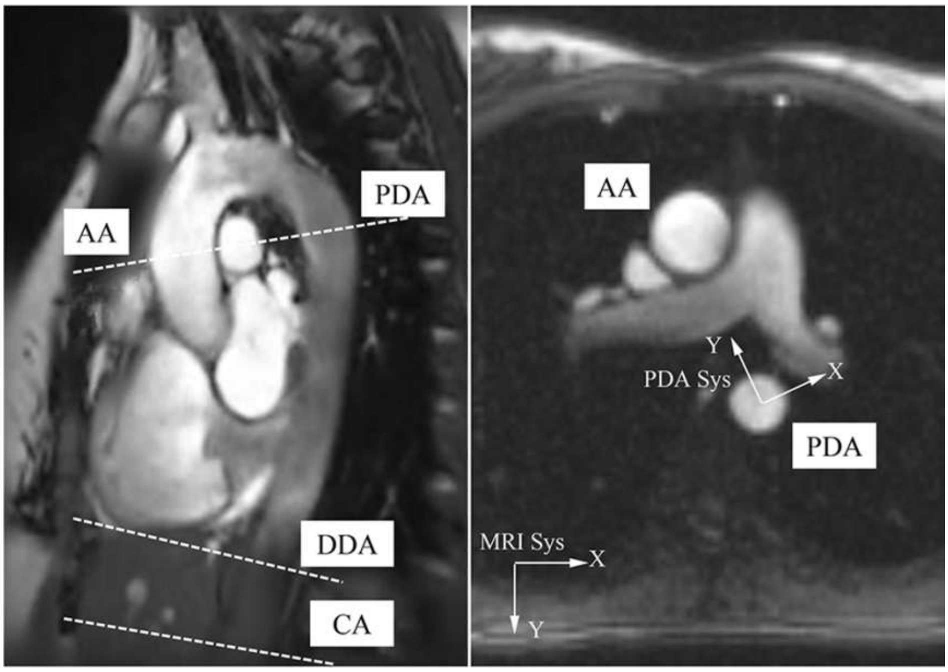

Figure 3.4: Oblique sagittal MRI image showing the locations of different aortic sections, the corresponding slice at AA for measuring its in-plane motion, the MRI reference system (MRI Sys) and the PDA system (PDA Sys)

Dynamic datasets were loaded into a semi-automatic tool, Argus (Siemens, Erlangen, Germany), in which the region of interest (ROI) was created and the aortic lumen boundary was detected based on the intensity gradient. After being manually adjusted, the ROI was propagated and adapted for each phase of the cardiac cycle. The Cartesian coordinates of the points on the aortic contour could be provided by this software application. The ROI geometric centroid was obtained by averaging the coordinates of the aortic contour. The AA in-plane displacement was defined as the distance between the centroid at the ending of diastole (initial) and the centroid on the analyzed image. The mean value and the standard deviation among all the subjects were then calculated from the maximum in-plane displacement of each time series. A PDA system was constructed with its origin at the PDA centroid at the ending of diastole, with the positive Y direction from the origin to AA centroid and with positive X normal to Y axis pointing to the left (Figure 3.4).

Reconstruction of the aorta

The aortic lumen was detected from end-diastolic 2-dimensional (2D) stack of SSFP images of a randomly-selected volunteer (25 years, male) using the in-plane region-growing method on Mimics software (Marterialise, Louvain, Belgium). The sinus of valsalva was not reconstructed since the AR was not the focus of the aortic wall stress analysis. As the 3-dimensional (3D) surface evolution was run through the stack of segmented contour, the aortic geometry was then extracted, smoothed and exported with stereolithography (STL) version for later processing.

FE modelling and material properties

LS-Prepost (LSTC, Livermore, CA, USA) was used to discretize the final aortic geometry with 4-node shell elements, which were subsequently offset with a uniform thickness of 1.6mm to generate the hexahedral elements. The assumed uniform aortic thickness was compatible with the reported ranges in literature [86] and was also commonly performed as in previous works [77, 84]. In order to determine the aortic model size, a mesh convergence analysis was performed with a pure structural simulation. A pressure of 80mmHg was imposed on aortic exterior walls of three models which were respectively discretized with 30,000, 100,000 and 300,000 brick elements. The aortic wall stresses were compared among these models. Since the initial aortic geometry was reconstructed at end-diastole instead of a zero-pressure condition, its stress-free configuration was achieved by extracting the resulting deformed mesh from mesh convergence simulation, as previously done in [24]. In order to simulate the blood flow and study the hydrodynamic effects, a fluid domain (Figure 3.5) was constructed to immerse the stress-free aorta. The fluid part was discretized with 250,000 hexahedral Eulerian elements. This size was also decided after a mesh convergence analysis against the section-averaged blood velocity with a 1% threshold.

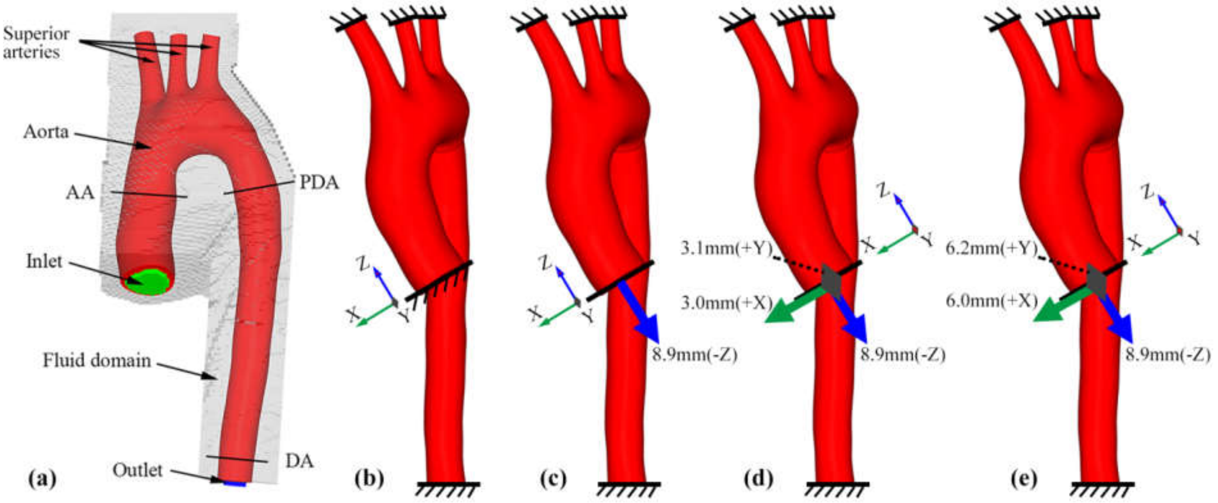

Figure 3.5: Aortic FE model and boundary conditions: aortic FE model for structural and FSI simulation (a); boundary conditions for SA-Pre (b), SA-Down (c), SA-XY (d) and SA-2XY (e). AA, PDA and DDA correspond to the sections of distensibility assessment

The aortic wall was assumed to be transversely isotropic and incompressible hyperelastic material [87], the parameters of which came from previously published data [88]. The fluid Eulerian mesh was subdivided in two domains and defined as multi-material: the first domain was blood initiated inside the aorta; the second domain was the fluid part outside of the aortic wall and defined as vacuum. The two fluid domains always updated as the FSI interface (i.e. aortic wall) moved or deformed, maintaining the blood inside the aorta and vacuum outside. For simplification, the blood was assumed as Newtonian fluid [24] with a density of 1050kg/m^3, a dynamic viscosity set to 4.5e-3Pa•s and a bulk modulus of 2.5GPa [24].

Aortic FE model validation

In order to validate the bio-fidelity of the aortic FE model, a structural simulation was performed on the stress-free configuration with three cycles of physiological time-dependent pressure [89] distributed on the inner surface of aortic wall. The aortic diameters of AA, PDA and DDA (see Figure 3.5a) were recorded during the simulation and those during the third cycle were used to assess the aortic distensibility. The distensibility was calculated with the Eq. (3.1) [90]:

$$\text{Distensibility}\ (10^{-3}mmHg^{-1}) = \frac{A_{max}-A_{min}}{A_{min}} \times P_{pulse} = [(\frac{D_{max}}{D_{min}})^2 - 1] \times P_{pulse} \quad (3.1)$$

where A_{max} and A_{min} represent the maximal and minimal aortic cross-sectional areas during the cycle, P_{pulse} is the pulse pressure and D_{max} and D_{min} are respectively the maximal and minimal aortic diameters.

Boundary and loading conditions

Four simulations were performed for structural analysis and two for FSI simulations, all of which were conducted on the stress-free configuration. The distal ends of the superior arteries and the descending aorta were constrained during all the simulations. The proximal end of AA was fully constrained only for the simulations without AR motion prescribed (Figure 3.5b-e).

For FSI analysis, a penalty coupling interface was defined between the aortic wall and the fluid domain as previously done in [24]. The inlet and outlet (Figure 3.5a) fluid parts were applied with a constant pressure of 120mmHg for a static analysis (hereafter referred as *FSI-Sta*). Another hydrodynamic simulation was conducted by pressurizing the inlet with 120mmHg and prescribing an outflow of 300mL/s at the outlet (referred as *FSI-Flow*). The reason why a constant pressure and flow rate rather than a pulsatile blood flow was chosen to apply in FSI analysis was to better compare the aortic stress levels in FSI and in structural analysis.

For the structural analysis, a Cartesian coordinate system was constructed to prescribe the AA motion (Figure 3.5) according to the local PDA system for AA in-plane measurement (Figure 3.4). A pressure of 120mmHg inside the aortic wall was the only loading for the control model (referred as *SA-Pre* and see Figure 3.5b). Besides 120mmHg pressurized inside the aortic wall, a displacement of 8.9mm along –Z was applied to AA proximal end to simulate AR downward traction (referred as *SA-Down* and see Figure 3.5c). The corresponding displacements (3.0mm-X, 3.1mm-Y) obtained from the cine MRI analysis were further imposed on the AA proximal end to evaluate the effects of AA in-plane displacement (referred as *SA-XY* and see Figure 3.5d). Finally, considering the hypothesis of AA in-plane displacement equal with AR motion, the AA proximal end was prescribed with twice magnitudes (6.0mm-X, 6.2mm-Y) of the in-plane displacement in another simulation (referred as *SA-2XY* and see Figure 3.5e) to aggressively estimate its influences.

All of the simulations (mesh convergence, FSI and structural analysis) were performed with the solver LS-DYNA 971 R7.1.1 (LSTC, Livermore, CA, USA) on an Intel Xeon (2.57 GHz) workstation with 40 processors.

3.2.3 Results

AA in-plane motion

Mean value (±standard deviation) of AA in-plane maximal resultant displacement was 5.5±1.7mm with X and Y components respectively: 3.1±0.9mm and -4.4±1.7mm (Figure 3.6a) under the MRI reference coordinate system. When measured in local PDA system, the X and Y components were correspondingly 3.0±1.3mm and 3.1±1.5mm (Figure 3.6a). AA in-plane motion had two phases: the displacement increased and oriented left-anteriorly during systole and then regressed to its origin in diastole (Figure 3.6b).

Mesh convergence analysis

Despite similar VonMise stress distributions, the stress magnitudes differed among the three models. The difference of peak aortic stress was less than 5% between the models of 30,000 and 100,000 elements while the difference was below 1.0% between the models of 100,000 and 300,000-elements. Accordingly, the aortic model of 100,000 elements was chosen for the following simulations.

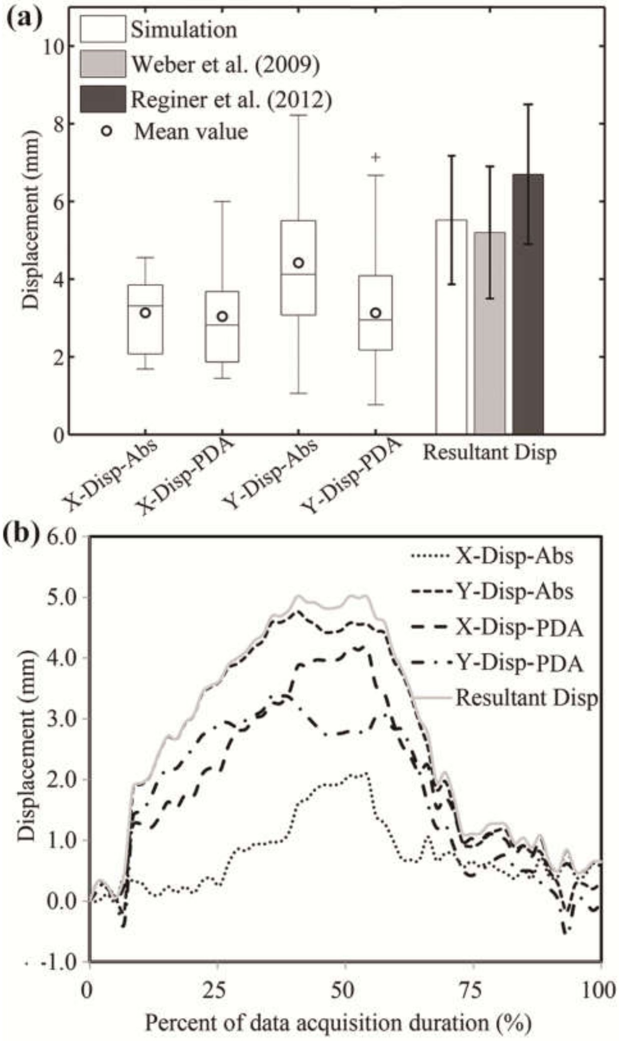

Figure 3.6: In-plane motion of AA section. AA maximal in-plane motion in absolute value averaging among the volunteers (a); time-history of in-plane resultant and component displacements of a volunteer (25 years, male) (b). X-Disp-Abs and X-Disp-PDA: X component motion under MRI and PDA reference system; Y-Disp-Abs and Y-Disp-PDA: Y component motion under MRI and PDA reference system; Resultant Disp: in-plane resultant displacement

Aortic distensibility

During numerical validation, the diameters of AA, PDA and DDA were 11.7mm, 8.5mm and 7.5mm respectively at the beginning of systole and 13.8mm, 9.4mm and 8.2mm at the ending of systole (Figure 3.7a). The distensibility was correspondingly 8.8e-3mmHg^{-1}, 5.3e-3mmHg^{-1} and 3.9e-3mmHg^{-1} for AA, PDA and DDA (Figure 3.7b).

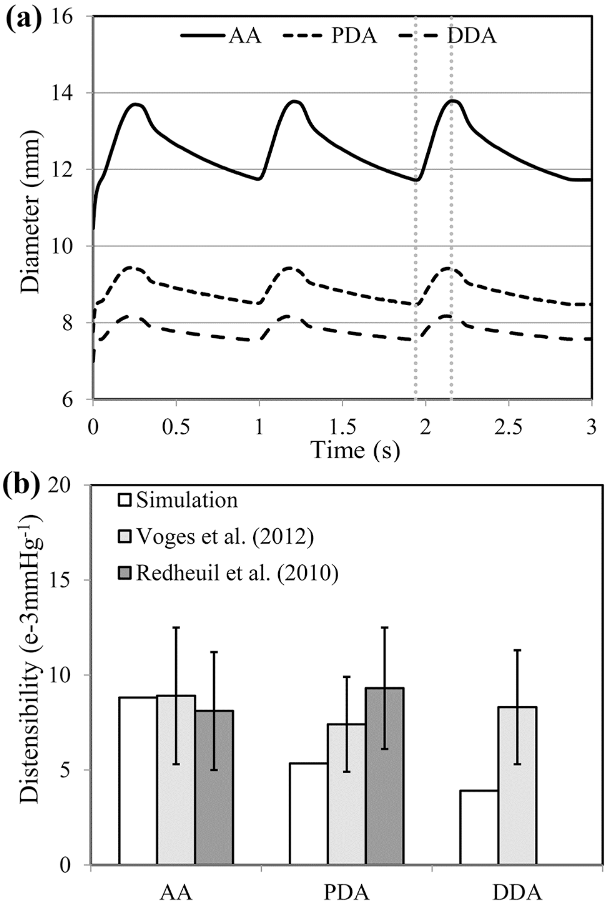

Figure 3.7: Aortic diameters and distensibility for AA, PDA and DDA: diameter time-history under the three-cycle pressure loading (a); aortic distensibility in simulation comparing with the literature data (b). The vertical dotted lines indicate the moments when the diameters were recorded for distensibility analysis

FSI and structural analysis

The distributions of VonMises, circumferential and longitudinal stress (see APPENDIX A) were similar among the control model (*SA-Pre*) and the FSI simulations (*FSI-Sta* and *FSI-Flow*). The peak VonMises and circumferential stress occurred at the interior curvature of aortic arch with the corresponding values of 0.24MPa and 0.48MPa for *FSI-Sta* and 0.22MPa and 0.47MPa for *FSI-Flow*. The peak longitudinal stress was 0.43MPa for static *FSI-Sta* and 0.42MPa for *FSI-Flow*, both located at the superior artery intersection. In Table 1 were displayed the aortic luminal volumes, AA, PDA and DDA sectional diameters in control and FSI simulations. The averaged stress levels, which were evaluated at the proximal AA section 2cm above the AR, were also displayed in Table 3.2.

Table 3.2: Aortic volumes, diameters of different sections and the averaged stress at the proximal AA section 2cm above the AR in control model and FSI simulations

	Volume (ml)	Diameter (mm)			Stress (e-2 MPa)		
		AA	PDA	DDA	VonM	Circum	Long
SA-Pre	163.1	29.9	19.8	16.9	9.3	14.4	6.0
FSI-Sta	163.0	29.9	19.8	16.9	9.3	14.3	6.0
FS-Flow	158.3	29.6	19.4	16.4	8.7	13.3	5.6
Diff-Sta (%)	-0.1	0.0	0.0	0.0	0.0	0.0	0.0
Diff-Flow (%)	-3.0	-1.1	-2.0	-2.9	-6.6	-7.5	-6.4

The Diff-Sta represented the result difference (in percent) between SA-Pre and FSI-Sta; Diff-Flow represented the result difference (in percent) between SA-Pre and FSI-Flow; VonM, Circum and Long were abbreviations respectively for VonMises, Circumferential and Longitudinal stresses.

The VonMises and circumferential stress contours were similar among all the structural simulations (Figure 3.8), with the corresponding peak values approximately 0.25MPa and 0.50MPa located at the interior curvature of aortic arch distal to AA. The longitudinal stress distributions (Figure 3.8) were also similar under different loadings with the superior artery intersection region always subjected to a peak stress of 0.43-0.51MPa. The peak circumferential stretch ratio of aortic wall (not shown) was 1.48 for all the structural simulations. The peak longitudinal stretch ratio (not shown) was 1.37 for *SA-Pre* and 1.41 for the other 3 structural simulations with AR motions (*SA-Down*, *SA-XY* and *SA-2XY*). The averaged stress levels at proximal AA section 2cm above AR were displayed in Table 3.3 for the structural simulations.

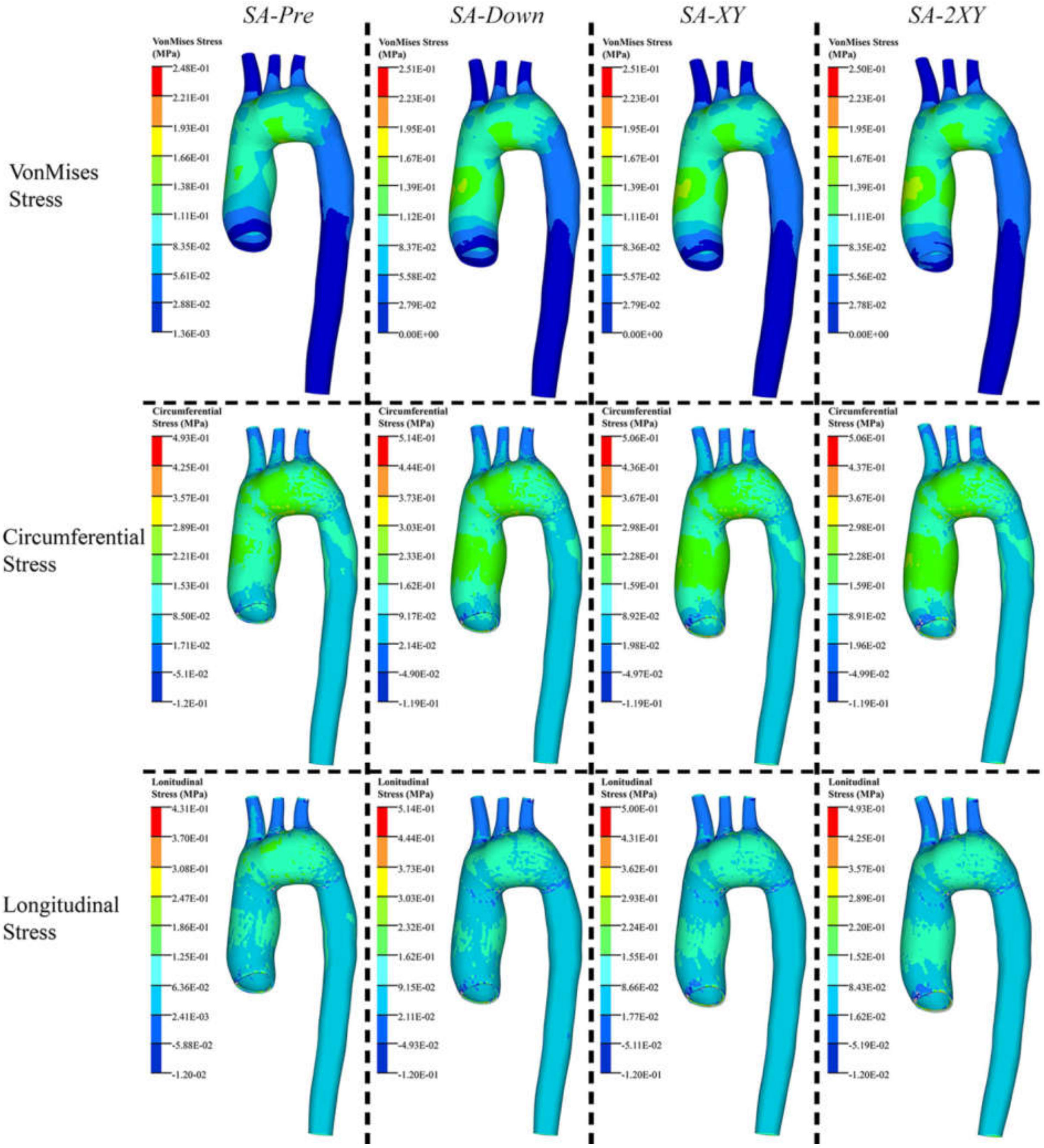
SA-Pre
SA-Down
SA-XY
SA-2XY
VonMises Stress
Circumferential Stress
Longitudinal Stress
VonMises Stress (MPa)
2.48E-01
2.21E-01
1.93E-01
1.66E-01
1.38E-01
1.11E-01
8.35E-02
5.61E-02
2.88E-02
1.36E-03
VonMises Stress (MPa)
2.51E-01
2.23E-01
1.95E-01
1.67E-01
1.39E-01
1.12E-01
8.37E-02
5.58E-02
2.79E-02
0.00E+00
VonMises Stress (MPa)
2.51E-01
2.23E-01
1.95E-01
1.67E-01
1.39E-01
1.11E-01
8.36E-02
5.57E-02
2.79E-02
0.00E+00
VonMises Stress (MPa)
2.50E-01
2.23E-01
1.95E-01
1.67E-01
1.39E-01
1.11E-01
8.35E-02
5.56E-02
2.78E-02
0.00E+00
Circumferential Stress (MPa)
4.93E-01
4.25E-01
3.57E-01
2.89E-01
2.21E-01
1.53E-01
8.50E-02
1.71E-02
-5.1E-02
-1.2E-01
Circumferential Stress (MPa)
5.14E-01
4.44E-01
3.73E-01
3.03E-01
2.33E-01
1.62E-01
9.17E-02
2.14E-02
-4.90E-02
-1.19E-01
Circumferential Stress (MPa)
5.06E-01
4.36E-01
3.67E-01
2.98E-01
2.28E-01
1.59E-01
8.92E-02
1.98E-02
-4.97E-02
-1.19E-01
Circumferential Stress (MPa)
5.06E-01
4.37E-01
3.67E-01
2.98E-01
2.28E-01
1.59E-01
8.91E-02
1.96E-02
-4.99E-02
-1.19E-01
Lonitudinal Stress (MPa)
4.31E-01
3.70E-01
3.08E-01
2.47E-01
1.86E-01
1.25E-01
6.36E-02
2.41E-03
-5.88E-02
-1.20-02
Lonitudinal Stress (MPa)
5.14E-01
4.44E-01
3.73E-01
3.03E-01
2.32E-01
1.62E-01
9.15E-02
2.11E-02
-4.93E-02
-1.20E-01
Lonitudinal Stress (MPa)
5.00E-01
4.31E-01
3.62E-01
2.93E-01
2.24E-01
1.55E-01
8.66E-02
1.77E-02
-5.11E-02
-1.20E-01
Lonitudinal Stress (MPa)
4.93E-01
4.25E-01
3.57E-01
2.89E-01
2.20E-01
1.52E-01
8.43E-02
1.62E-02
-5.19E-02
-1.20E-02

Figure 3.8: VonMises, circumferential and longitudinal stress distribution for structural simulations with different AA motions

Table 3.3: Averaged VonMises, circumferential and longitudinal stress for proximal AA 2cm above the AR in structural simulations

Loadings Stress(MPa)	SA-Pre	SA-Down	SA-XY	SA-2XY
VonMises	0.093	0.128	0.131	0.134
Circumferential	0.144	0.191	0.195	0.199
Longitudinal	0.060	0.084	0.086	0.083

3.2.4 Discussion

Ascending aortic in-plane motion assessment

In this study, the AA in-plane motion was analyzed under MRI and PDA reference system. Although seeming to be more explicit under MRI system, the in-plane displacement under PDA system might be more meaningful with the specific anatomic reference at PDA. The component motions under PDA system were mostly alike, while the Y component mean value was 42% higher than the X component under MRI system resulting in a left-anteriorly oriented motion. Similarly, the AA in-plane motion was reported to be left-anterior in 58% cases and to be anterior in 43% [91]. Moreover, the Y component was found to be nearly twice of the X component [91]. The resultant in-plane displacement in our study was also consistent with the published values 5.2±1.7mm [82] and 6.7±1.8mm [83], all of which were comparable with the magnitude of downward motion (8.9±1.8mm) [81]. This also justified the necessity to study the in-plane motion effects on aortic stresses.

Weber et al. [91] indeed studied the aortic 4-dimensional displacement with computed tomography angiography, but the final temporal resolution as well as the temporal reconstruction methods lacked of description. In CT scan, the normal range of temporal resolution was around 83-125ms according to another research [92]. In contrast, the time resolution of our MRI dataset was about 15ms, enabling to capture a more detailed in-plane motion during a 300ms-long systole. Admittedly, the influences of AA through-plane displacement on its in-plane measurement had to be ignored due to the limited computational capabilities to analyze the 4-

dimensional dataset. Besides, the AR in-plane displacement also had to be assumed equal to the AA motion with the current data accessible. Despite the hypothesis above, our AA in-plane motion analysis could still add to the knowledge of aortic 3D motion related to the cardiac pulsatility.

Model assessment against aortic distensibility

Before studying the AA in-plane motion effects, the distensibility of the model was analyzed to evaluate its bio-fidelity. Although lower than the published mean values [90, 93], the distensibility for AA and PDA was within their standard deviations. The DDA of the model seemed to be less compliant than reported [90]. The fixed boundary at distal DDA could have limited the radial inflation of DDA. The aorta was assumed to be of 1.6mm uniform thickness in this study for modelling convenience and the difficulties to detect the aortic thickness with our available MRI data. However, the descending aorta has been suggested about 15% thinner than AA [94]. The relative thicker descending aorta in the simulation was speculated to induce its lower distensibility. Still, the reproduced circumferential stretch ratios at peak systole of AA, PDA and DDA were respectively 1.32, 1.21 and 1.17, which coincided with the published ranges 1.08-1.47 (median value 1.26) obtained with the same pressure level inflation tests [86]. Therefore, to some extent, this aortic FE model was still believed to reflect the realistic aortic compliance under physiological conditions.

Necessity to consider fluid-structure interactions

Fluid dynamic effects on aortic responses were also analyzed by comparing the results of the control model and the FSI simulation with or without a constant blood flow. The differences against the control model were always no more than 0.1% in terms of aortic luminal volumes, diameters or stresses when a static pressure was imposed on the inlet and outlet. However, when the blood flow was simulated in the aorta, the aortic stresses, luminal volume and radial dilation were respectively reduced by 6.4-7.5%, 3.0% and 1.1-2.9%. In fact, the continual blood flow was maintained by the pressure gradient along the aortic course. In other words, further along the aortic pathway, lower the luminal pressure became. This could explain why the stresses and aortic diameters in FSI simulation with flow were lower compared to control model and this tendency seemed to be more significant for the descending aorta (Table 3.2).

Considering the different results between simulations with or without blood flow, it was necessary to mimic the non-uniform hydrodynamic pressure ambient in the aorta as a consequence of the flowing blood. The wall stress resulting from blood pressure could be 0.48MPa, while the wall shear stress (WSS) due to the blood flow was less than 1.5Pa at different aortic sections (see APPENDIX B). In other words, WSS was negligible in terms of its magnitude compared to wall stress. Although WSS could not lead to aortic dissection directly, its variable distributions have been suggested to induce aortic aneurysm progression and aortic tissue remodelling through a complex interplay between vascular cellular migration and extracellular matrix homeostasis [95-97]. Therefore, it was still essential to simulate the blood flow and its interaction with the aortic wall while studying the WSS effects on aortic pathologies and diseases.

Relative contribution of aortic root motions to ascending aorta dissection

Both effects of AR axial and in-plane motion on aortic responses were evaluated by imposing downward and in-plane displacement on proximal AA end. Similar with other researches [77, 84], the peak aortic VonMises and circumferential stress were always located at the superior artery branches. Since the AR traction was previously postulated to increase proximal AA transection risk by elevating its longitudinal stress [77, 84], the stress levels were also evaluated by respectively averaging the VonMises, circumferential and longitudinal stresses of the AA section 2cm above the AR under different loading conditions (Table 3.3). The AR axial motion contributed to 40% increase of AA longitudinal stress, in spite of the previously reported higher values 50%-150% [77, 84]. However, the longitudinal motion elevated the AA VonMises and longitudinal stress by 37.6% and 32.6% in our study, which contradicted with its negligible influences on these stresses in [77, 84]. Another difference was the location of peak aortic longitudinal stress, which was always at the aortic arch interior curvature in our study but at the superior artery intersections previously [77, 84]. These discrepancies could be attributed to two reasons.

On one hand, both researches [77, 84] assumed aortic wall to be linear elastic material with a Young's modulus of 3MPa. Aorta is actually a complex fiber-reinforced composite structure displaying highly nonlinear responses. Previous aortic uniaxial stretch tests [74, 98] suggested the stiffness of young healthy samples continuously increase as the stretch ratio was higher than 1.20.

With a luminal pressure of 120mmHg, the peak aortic stretch ratio reached 1.36 previously in [98] and 1.48 in our study. Therefore, the aortic stiffness under the pressure of 120mmHg with or without AR motion should not be defined as constant. Moreover, the elastic modulus of 3MPa in these two studies [77, 84] might be stiffer compared to the dynamic stiffness of healthy aorta, which was found less than 1.5MPa at the stress level of 74kPa corresponding to a stretch ratio range of 1.18-1.49 [99]. Admittedly, the transversely isotropic material was a limitation of our study, but the behavior of healthy aortic wall was proved practically isotropic with the stretch ratio less than 1.8 [74, 98]. The transversely isotropic hyperelastic material, the parameters of which were previously obtained by fitting aortic stretch curves [86, 88], was considered a good approximation to the aortic responses within the loading levels of our study (maximal stretch ratio less than 1.50).

On the other hand, a toroidal coordinate system was constructed to convert the global stresses into local circumferential and longitudinal stress in both previous researches [77, 84]. However, this approach might be questionable since the complex geometry of the aorta was beyond the ability of a single global system to convert into local stresses. In this work, each element axis was oriented along the aortic longitudinal direction (see APPENDIX C) during the model discretization process. The circumferential or longitudinal stress could be converted according to each local element system in post-processing. In this way, the conversion of the circumferential and longitudinal stresses could avoid being affected by the aortic geometry.

The circumferential stress at AA in our work was always less than 0.20MPa with the longitudinal component only half of its magnitudes and less than 0.09MPa (see Table 3.3). All the stresses in this study were found to be negligible compared with the yield stress (1.18±0.12MPa in circumferential and 1.21±0.09MPa in longitudinal directions) reported in [100] or the tensile rupture stress (1.27MPa) of thoracic aorta published in [98]. Furthermore, the peak stretch ratio of AA, was always less than 1.50 under all loading conditions and was also well below the previously recorded stretch failure of 2.1 [98]. Therefore, despite its effects of increasing AA longitudinal stress, the conclusion that AR downward motion associated with heart traction were enough to induce aortic transverse dissection or add the injury risks [77, 84] should be further pondered since our results were obtained with healthy subjects (normal aortic material, morphology and hemodynamics).

Compared with the downward motion, the AR in-plane displacement did not seem to alter the aortic stresses especially for the AA segment, which was still true even with the in-plane displacement magnitudes doubled. Although comparable with AR axial displacement (8.9±1.8mm), the AR in-plane motion (5.5±1.7mm) was inappreciable versus the distance (130mm in our model) between the AR and brachiocephalic artery. Thus, the in-plane motion could barely change the aortic length (longitudinal deformation). Since aortic inflation was mainly the consequence of luminal pressure, the in-plane motion hardly induced circumferential deformation, either. Without longitudinal or circumferential deformation, the stress level would not be modified.

Although the AR axial or in-plane motion didn't seem to elevate the aortic dissection risks in this study, additional mechanisms should account to aortic dissection. This injury should still be related to the factors increasing aortic wall stress and reducing aortic strength. The aortic stress could be enhanced by such factors as hypertension and aortic dilation. Cardiovascular diseases like aortic insufficiency would increase AR axial motion through ventricular compensation [77]. This increased motion could additionally elevate the aortic wall stress in subjects with higher aortic stiffness attributed to higher ages and vascular diseases (e.g. Marfan syndrome and atherosclerosis). Moreover, in these vascular diseases, the aortic strength would also be jeopardized with the aortic tissue remodeled. When the local aortic stress exceeds what the aortic tissue can resist, the aortic dissection might occur.

3.2.5 Conclusions

The AR in-plane motion was analyzed with the MRI data from 25 volunteers. The in-plane displacement increased during systole and regressed in diastole. The in-plane movement was found to be comparable to the axial motion, with its mean value (±standard deviation) 5.5±1.7mm. The X and Y components of in-plane motion were respectively 3.1±0.9mm, -4.4±1.7mm under MRI reference system and 3.1±1.5mm, 3.0±1.3mm under PDA system. Blood flow should be simulated with FSI approach considering the lower values of aortic diameters, volumes and stresses as a result of hydrodynamics. The AR downward displacement did not improve AA's vulnerability to dissection since the resulting 40% increase of longitudinal stress was still trivial against the aortic yield stress. With inducing negligible aortic circumferential or axial deformation, AR in-plane motion had no effect on aortic stress levels.

3.3 Aortic stress level against stress thresholds

The aortic stress level during cardiac cycle was evaluated in Chapter 3.2 by applying a systolic intra-aortic pressure and a 3D aortic root motion. The magnitudes of the peak aortic stretch and VonMises stress did not depend whether the simulations included AR 3D motions or not. The peak values of aortic stretch stress were 1.48 and 1.41 for circumferential and longitudinal direction. The peak VonMises stress of aortic wall was 0.25MPa. The peak stretch and VonMises stress were always located at the interior curvature of aortic arch distal to AA during all the simulations. The AR longitudinal or in-plane motion displayed quite limited effects on aortic wall stress distribution. Although AR longitudinal motion increased the aortic longitudinal stress, the proportion of stress elevated by AR motion (i.e. 0.08MPa) was far below the aortic longitudinal stress threshold of 1.80±0.24MPa [100]. Therefore, the aortic responses under cardiac loadings mainly result from the aortic luminal pressures.

The peak aortic stresses and stretch ratio due to cardiac loadings were listed in Table 3.4 with the corresponding values published in literature for MVCAs and aortic tensile tests. To briefly review the data in MVCAs [17, 19, 21, 101], the aortic stresses were obtained with numerical reconstruction of MVCAs. The cardiac cycle was not modeled in these previous studies and the stress levels due to the ventricular traction or blood flow were not thus considered. The aortic stresses during cardiac cycle were comparable with the corresponding magnitudes reconstructed in MVCAs. The circumferential and longitudinal stresses under cardiac cycle were 28.3% and 29.8% of the failure thresholds. Furthermore, the stretch ratios under cardiac function were 67.1%~70.5% of the failure thresholds. In other words, BAR in MVCAs should result from not only the aortic loadings due to crashes but also the contribution of human cardiac function including ventricular traction and intra-aortic pressure. Therefore, the cardiac function needs to be simulated in BAR studies for MVCAs to consider the aortic physiological loadings which result primarily from aortic luminal pressure and secondarily from ventricular traction.

Table 3.4 Peak stresses and stretch ratio of aortic wall during cardiac cycle, MVCAs [17, 19, 21, 101] and tensile failure tests[98, 100]

	Stress (MPa)			Stretch ratio	
	VonMises	Circumferential	Longtudinal	Circumferential	Longtudinal
Cardiac	0.25	0.51	0.51	1.48	1.41
Pressure	0.25	0.51	0.43	1.48	1.41
MVCA	0.13~3.1 [17, 19, 21, 101]	--	--	--	--
Threshold	1.27 [98]	1.80±0.24[100]	1.71±0.14[100]	2.1 [98]	

CHAPTER 4 INTRA-AORTIC PRESSURE IN MVCA

4.1 Introduction

We presented in Chapter 3 that it is necessary to simulate cardiac cycle especially intra-aortic pressure during MVCA reconstruction for BAR research. Intra-aortic pressure had been proposed as one of the numerous BAR mechanisms in MVCAs, but its effects on aortic injury became controversial in some studies and remains unclear [9-12].

Forman et al. [12] performed 9 sled tests with human cadaver thoraces (see Figure 4.1) which resulted in minimal chest compression and a peak mid-spine acceleration of 169±35.0g. The maximum intra-aortic, tracheal and esophageal pressures reached 177kPa, 112kPa and 156kPa while no macroscopic BAR was observed. They postulated that thoracic acceleration could not cause BARs alone and the differential pressure across the aortic wall was still below the injury tolerance despite the high intra-aortic pressure. Bass et al. [11] performed burst tests on human entire aorta samples with the pressure loading rate similar as that recorded in cadaveric sled tests. The pressure values at aortic failure were used to construct the Weibull survival risk curve (displayed in Figure 4.2). A pressure of 101kPa was reported to cause a 50% risk of failure for all the aortic samples while a pressure of 120kPa for the subjects below 68 years. Hardy et al. [9] reproduced clinically relevant BARs with 8 human cadavers which were tested with dynamic blunt loading modes (i.e. frontal impact, side impact, submarining and combined loading) (Figure 4.3). The cadavers were inverted during the tests and the aortas were perfused. The aortic pressure reached 165kPa for only one test but other tests had a peak pressure less than 85kPa. They concluded that thoracic deformation was critical to BAR and the contribution of intra-aortic pressure to BAR was limited.

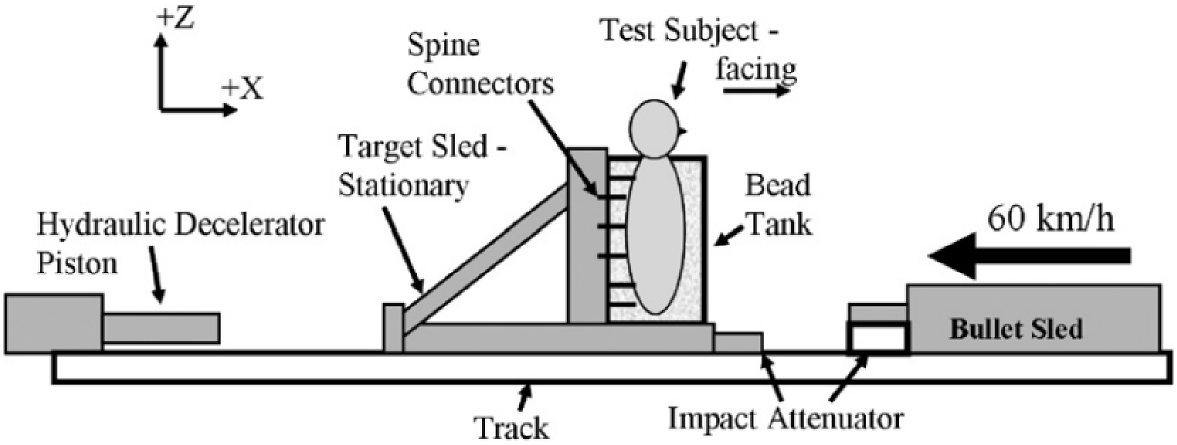
+Z
+X
Spine Connectors
Test Subject - facing
Target Sled - Stationary
Bead Tank
Hydraulic Decelerator Piston
60 km/h
Bullet Sled
Track
Impact Attenuator

Figure 4.1 Schematic illustration of the sled test system to reproduce BAR with limited thoracic deformation (adapted from [12])

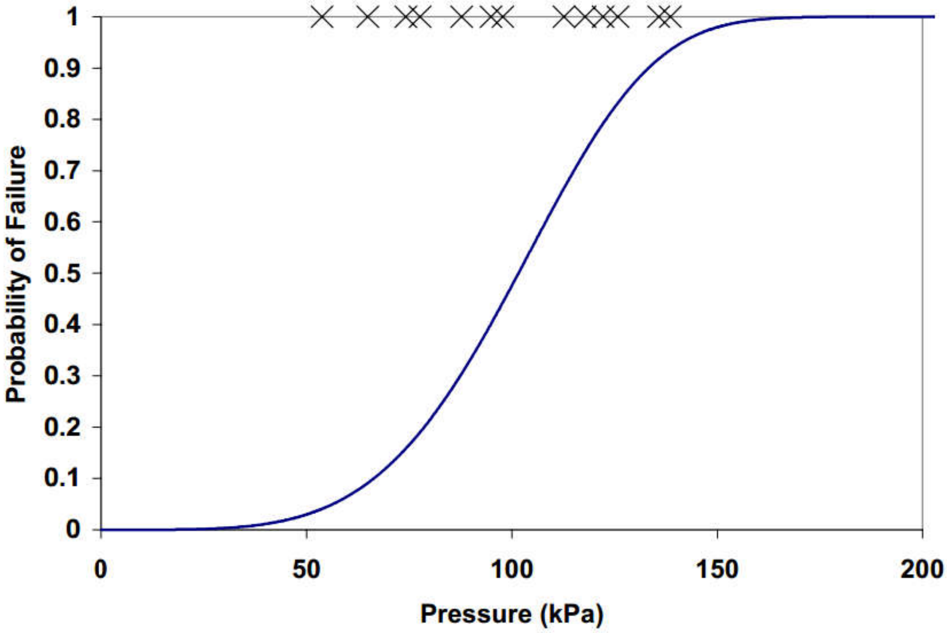

Figure 4.2 Weibull injury risk for aortic bust tests under pressure impulse loading (adapted from [11])

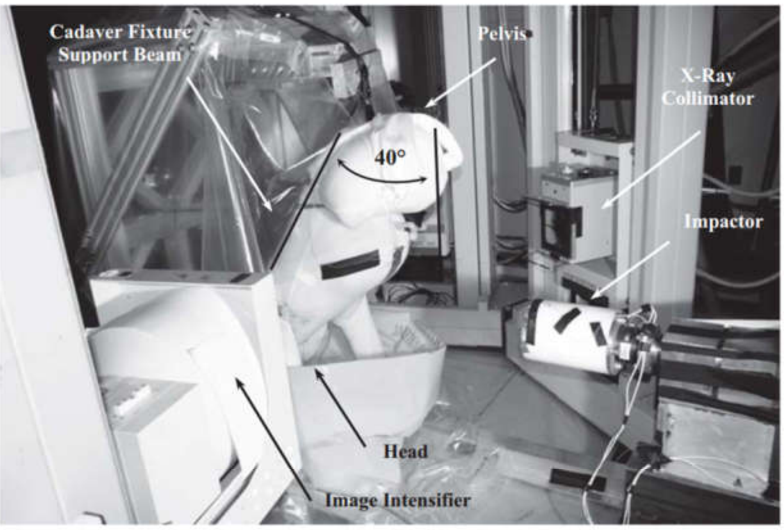
Cadaver Fixture Support Beam
Pelvis
X-Ray Collimator
40°
Impactor
Head
Image Intensifier

Test XR2, Frontal impact

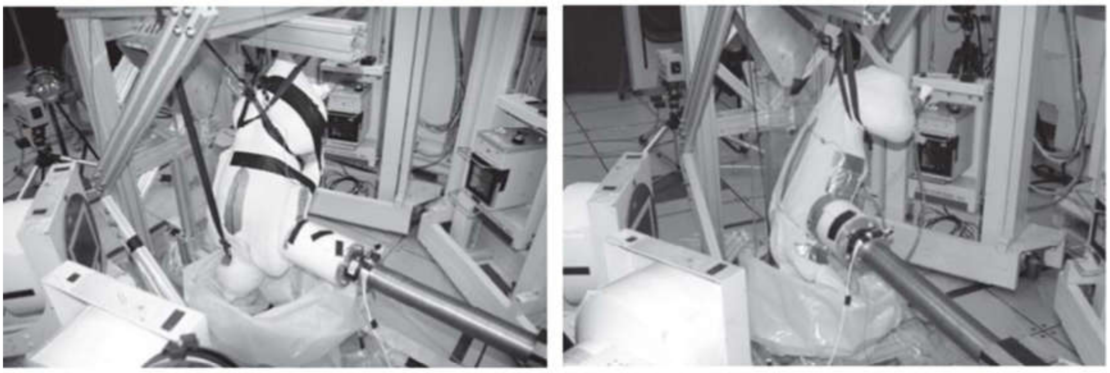

Test XR4, Arm side Impact

Test XR5, Rib side impact

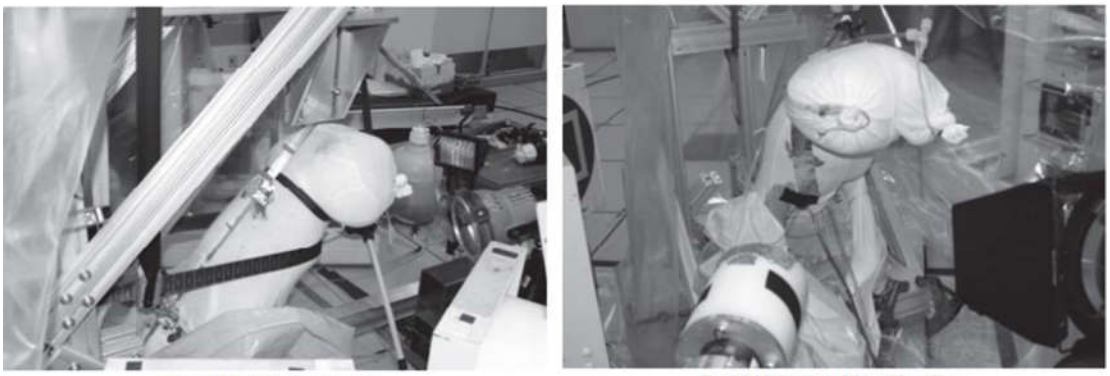

Test XR7, Submarining

Test XR8, Combined loading

Figure 4.3 Representative frontal impact (top), side impact, with and without arm engagement (middle left and right, respectively), submarining simulation (bottom left), and oblique impact (bottom right) configurations (adapted from [9]).

The simulation approaches to consider the pressure effects on aortic loadings also differed in previous studies [17, 19, 21, 22, 75, 102]. In the simplified thoracic model proposed by Richens et al. [102], the aortic blood was modeled with an elastic material and Lagrange solid elements to consider the intra-aortic pressure. In this study, the blood flow could not be modeled and the so-called ‘pressure’ resulted from the deformation of elastic blood material. In a more complex human FE model, the aortic luminal pressure was simulated by defining an airbag filled with linear elastic fluid [19, 21]. The intra-aortic pressure was quantified by a uniform monitored volume (airbag type) pressure and the pressure modification due to blood flow occlusion was not taken into account in this study. In another human thoracic model previously used to study the effects of aging factors on thoracic injury risk, the aortic lumen was kept empty without blood filling [75]. In this case, aortic stress levels only resulted from the material deformation due to aortic interactions with the surrounding organs. Blood flow and blood interaction with the aortic wall were simulated in an isolated aorta FE model during traumatic rupture conditions [22]. The aorta was modeled as a single-layered thick wall composed of two fiber families with viscoelastic material. Blood flow and WSS modifications due to aortic deformations were reproduced but the blood pressure or aortic interactions with the surrounding thoracic organs were not considered. In other words, the aortic stress levels were limited to those resulting from the prescribed aortic deformations, without considering the effects of intra-aotic pressure or aorta-chest interactions.

This chapter aims to identify the necessity of considering intra-aortic pressure during MVCA-related BAR studies.

4.2 Article #2: Intra Luminal Pressure as a Determinant Factor in Blunt Aortic Rupture: an Experimental Ex-Vivo Study

This article entitled “Intra Luminal Pressure as a Determinant Factor in Blunt Aortic Rupture: an Experimental Ex-Vivo Study” was submitted to the Journal of Trauma and Acute Care Surgery on 4th April, 2018. It was still under review at the time this thesis was written.

Aurélien Culver MD[a,b,*], **Wei Wei** PhD[a,*], Marc Leone MD, PhD[b], Thierry Bege, MD, PhD[a], Michel Behr PhD[a]

[a] *Aix-Marseille University, IFSTTAR, LBA UMR T24, Marseille, France*

[b] *Aix-Marseille University, Department of Anesthesiology and Intensive Care Medicine, the North Hospital, AP-HM, Marseille, France*

Abstract

Background: Blunt aortic injury is responsible for a high mortality rate in motor vehicle crash accidents, and can occur in even relatively low-speed impact conditions. High levels of intravascular pressure during shock were previously postulated to initiate such injuries although the exact mechanism seems complex, multi factorial, and remains unclear. Moreover, its complexity makes it difficult to reproduce in experimental studies. Our study was aimed to determine a luminal aortic pressure triggering threshold leading to aortic wall rupture in low-speed car crash conditions.

Methods: Thirteen human aortas were dissected in this study. The samples were mounted on a hydraulic loop experimental setup and pressurized with a compressor delivering a continuous airflow. The intra-aortic pressures were continuously measured by two pressure sensors while the trials were filmed by a high-speed camera to capture the rupture locations. A pressure-induced risk curve of aortic rupture was also generated according to the recorded failure pressures.

Results: Nine out of the thirteen human aortas were used for the aortic burst tests, since four specimens were excluded due to the poor tissue quality. The mean value of the failure pressures was 131.8 ± 11.7 kPa (989 ± 88 mmHg) and 44% of all the samples were ruptured at aortic isthmus. From the injury risk curve, a pressure of 133.5 kPa (1001 mmHg) corresponds to a 50% risk of aortic failure.

Conclusions: An aortic luminal pressure injury triggering threshold of 133.5kpa was proposed, that could lead to blunt aortic ruptures in relatively low-speed car accident conditions. This value could provide data basis for better predicting aortic injury risk in the field of road safety.

Level of evidence: III, economic & value-based evaluations.

Keywords: Blunt aortic rupture, Intra-aortic pressure, Experimental, Injury risk, Vehicle crash accidents

4.2.1 Background

Blunt aortic rupture is the most common injury among large mediastinal vessels [103] and the second leading cause of death in motor vehicle crash accidents (MVCAs) (15 to 30%) [104-107]. The onset conditions are always high-energy situations, as MVCAs were considered to contribute to 80-90% of the blunt aortic ruptures (BAR) [38, 39, 108, 109]. Other circumstances include motorcycle accidents, high falls and horse-riding accidents [7]. Despite the vast diversity of accident scenarios, the aortic injury at peri-isthmus was found in 90% of the cases in clinical studies and 62% of the cases in cadaveric studies [43, 102].

Several injury mechanisms of BAR have been proposed, mainly based on observations from autopsies after MVCAs, followed by animal [110, 111] and human body ex-vivo experiments [7, 106, 112]. However, the exact role of certain factors that may influence these mechanisms, such as the conditions and timing of the accident or the victim's characteristics, remain unclear. Especially the interactions among these factors cannot be excluded and are difficult to reproduce in the laboratory. Currently, there are two distinct injury mechanisms in literature. One incorporates the notion of inertia: antero-superior projection of the heart-aorta block during sudden deceleration would cause the aortic junction to be stretched or sheared, particularly in the isthmic area [7, 8, 106, 112]. On one hand, this site corresponds to an anatomical zone of fragility due to the lowest aortic parietal thickness (closure area of the arterial canal). On the other hand, the location of isthmus at the junction between the aortic arch "movable" and the "fixed" descending thoracic aorta makes this region more vulnerable. The second proposed mechanism was related to blood hydrodynamics [7, 113]: abdominal compression by the seat belt and/or steering wheel during impact, as well as compression of the thoracic wall, would be responsible for a sudden increase in intra-aortic pressure ("Water Hammer" effect). This intravascular high blood pressure would cause the transverse rupture of the wall with the parietal tension reaching its limit value.

In this second potential mechanism, it is crucial to know precisely the threshold pressure level that the aortic wall would be able to withstand, for example in the context of developing human body models able to predict aortic injury risks in the context of road safety research. To our knowledge, there is only one previous experimental study aimed to determine this threshold on human aortas [11], performed at a loading rate corresponding to high speed impact conditions. It was suggested that this mechanism be compatible with the overpressure conditions expected in a car crash situation.

In this context, the objective of this work is to perform ex-vivo experiments on human aortic samples to determine an injury criterion that could be considered in even relatively low-speed car impact conditions.

4.2.2 Methods

The study was performed from January to June 2017. Human aortas were used to study the maximum level of pressure prior to aortic rupture. They were dissected from 13 un-embalmed corpses before the tests. The samples would be excluded from this study if failing the following criteria: no anatomical abnormity, pathology or severe degeneration. The whole process of dissection and sampling was performed in the pathological anatomy laboratory (Medicine school, La Timone, Marseille) and met the ethical standards of Aix-Marseille University. After opening the thoracic cage and extracting the lungs by sections of the hiles, the descending aorta was revealed and then cut at the level of the diaphragmatic hiatus. It was gradually removed from the spinal column in a retrograde manner, to the aortic junction, where the left subclavian artery, left common carotid, and brachiocephalic trunk are successively sectioned. The intercostal arteries were severed during progression. The ascending aorta was cut off at the aortic valve in order to maintain maximum vascular tissue. Forward, the pulmonary artery was removed from the aortic arch by a prudent arterial ligament section (aortic isthmus), and backward, the aorta was separated from the other mediastinal elements by progressive fascia detachment. Once retrieved, the aorta was permeabilized again by expelling blood clots that obstructed its lumen. The sections of the superior aortic branches and the coronary arteries were then sutured. After dissection, the fat and peri-aortic tissues were removed, so that the aortic wall was completely cleansed of its surrounding tissues. All the specimens were soaked in saline water and stored with a rapid freezing technique (3-5°C).

In order to apply pressure, a circuit consisting of low-compliance polyvinyl chloride pipes reinforced with high tenacity textile braids was utilized. At the end of the circuit was mounted a metal valve which was closed during pressurization. When being fixed on the circuit, the aortas were always ensured to have their anatomical posture to avoid any twist preloading before pressurization. The schematic of the experimental set up is shown in Figure 4.4. Complete tightness, especially with air, was difficult to achieve for high pressures during preliminary tests, despite the vascular sutures (0.5 mm in diameter). Therefore, an equivalent technique to an "inner tube" was used: a very thin medical latex sheath (0.1 mm thick) was fit inside the aortic lumen. Since the compliance of this membrane is far superior to that of the aortic wall, we hypothesized that its mechanical contribution was negligible compared with the aortic wall. Using latex sheath (see Figure 4.5) is our original approach to better prevent leakage during pressurization period compared to the traditional way of solely making sutures [11], which often suffers from leakage under high pressure levels. The fixation of the aortas and the latex sheath on the circuit was achieved by using metal clamps inside with foam pads were also fitted to prevent any pre-trauma on the aortic wall. The aorta was pressurized until failure with an air pump (LH2055; Lehua, Ningbo, China), which was pre-calibrated to generate air flow at a rate of 1000 mL/s. The air pressure in the aorta was recorded by two pressure sensors (EPX, TE connectivity, Schaffhuasen, Switzerland) and the aortic inflation was captured by a high-speed camera (Fastcam SA3 model 120; Photron, Tokyo, Japan) with 1000 Hz image frequency. Primary outcome was the maximum pressure level before failure measured in the aorta. Maximum pressures of all the aortas were used to generate the pressure-induced injury risk curve with 2-parameter Weibull analysis as previously done and detailed in Bass et al. [11]. After the aortic burst tests, a single latex sheath, the same as the one previously fitted inside the aorta, was mounted to the burst test system and inflated with the same protocols. The pressure time-history was recorded and compared to those of aortic burst tests. To be noted, the pressure time-history presented here was acquired by filtering the recorded raw signals using a low-pass first-order filter and 180 Hz cut-off frequency with Matlab (The Mathworks, Natick, MA, USA).

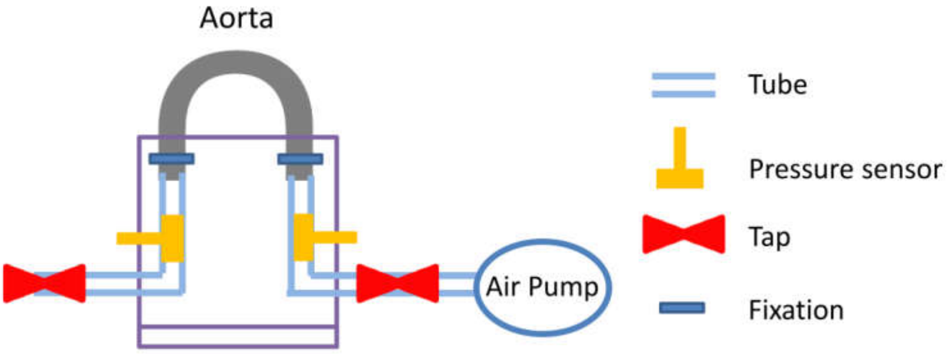

Figure 4.4: System configuration for aorta pressurization

4.2.3 Results

Thirteen human aortas were dissected for the experiments. They came from subjects aged 66 to 96 (average age 88 years), including 5 females and 4 males. Calcification plaques were present in the arterial wall of each aorta. Four aortas were excluded from the protocol immediately after dissection for tissue quality issues: 2 aortas had major anatomical abnormalities; 2 others showed macroscopic necrosis, suggesting underlying aortic pathology or poor specimen preservation after death.

An example of the test procedure at different moments was displayed in Figure 4.5. The maximum intra-aortic pressures before rupture for each aorta and the rupture locations are given in Table 4.1. The rupture location was peri-isthmic in 44% of cases (4 out of 9 aortas). The mean value of aortic rupture pressures was 131.9 ± 11.8 kPa (989 ± 88 mmHg) (Table 4.1). The mean pressure versus time before aortic rupture and the corresponding experimental corridors (Figure 4.6) were acquired with the same approach as previously reported by Lessley et al. [114]. The pressure time-history of latex sheath inflation test was also displayed in Figure 4.6. The pressure transition curve of the latex sheath was considerably inferior to those of the aortas, indicating the negligible contribution of the latex sheath to the aortas' strength during pressurization. The pressure-induced injury risk curve which was generated with the aortic maximum pressures (listed in Table 4.1) was presented in Figure 4.7.

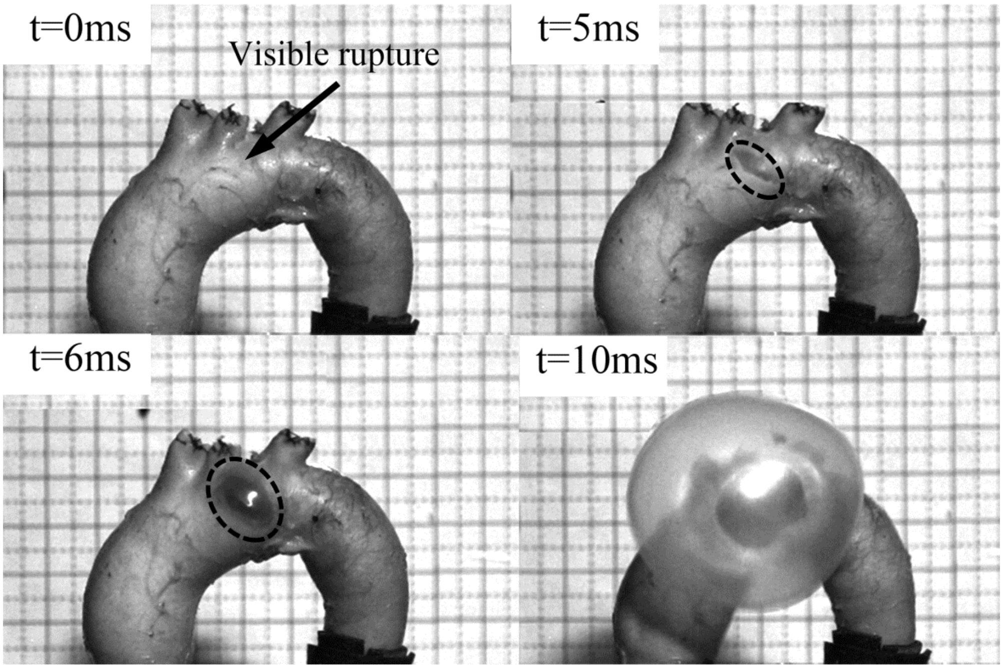

Figure 4.5: High-speed photos of Aorta-3 burst test at different moments: the first moment of visible rupture (defined as t=0ms), complete aortic rupture (t=5ms), the beginning of latex inflation (t=6ms) and complete latex inflation (t=10ms).

Table 4.1: Summary of specimen parameters, burst pressures and rupture locations

ID	Gender	Age (Year)	Pressure (kPa)	Rupture location
Aorta-1	F	96	117.3	A
Aorta-2	F	85	123.2	B
Aorta-3	F	92	134.4	B
Aorta-4	F	87	139.2	C
Aorta-5	F	91	121.3	B
Aorta-6	M	89	112.0	A
Aorta-7	M	66	134.9	A
Aorta-8	M	90	146.0	B
Aorta-9	M	96	158.0	C

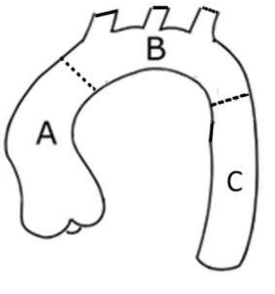

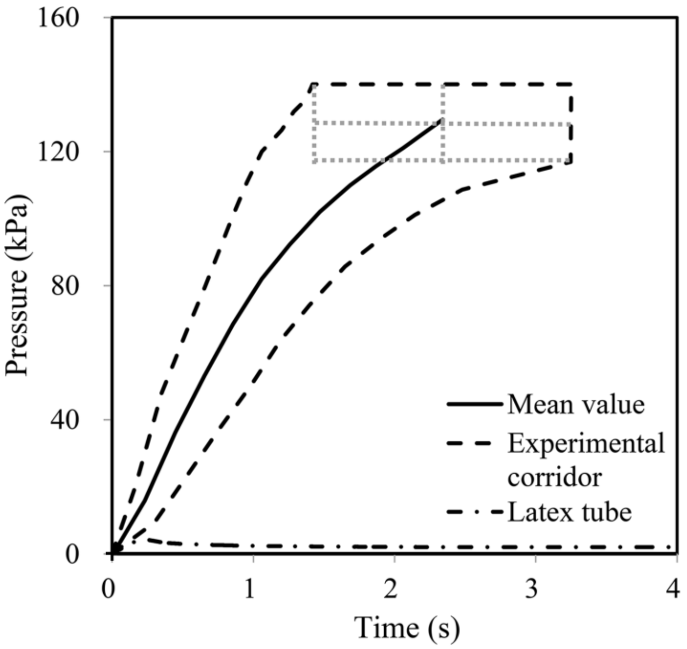

Figure 4.6: Mean value of pressure versus time recorded in aortic burst tests along with the experimental corridor and the pressure time-history of the latex tube inflation test. The grey dotted lines correspond to the range of variation for different points on the average curve, which was used to obtain the experimental corridor as previously detailed [114].

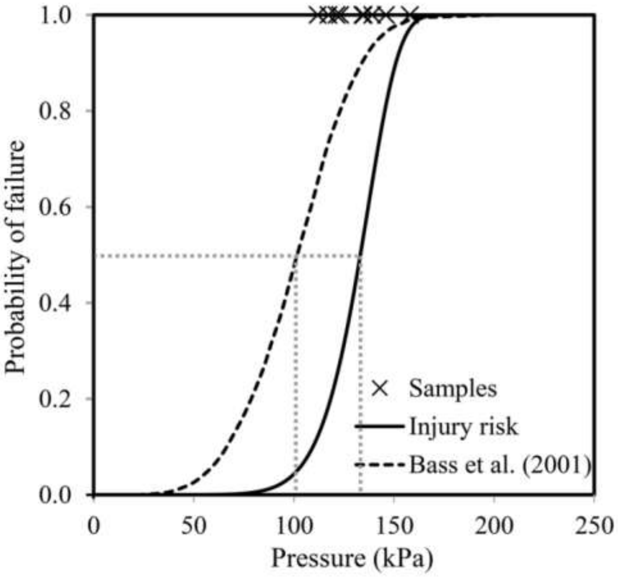

Figure 4.7: Weibull injury risk of aorta for pressure loadings compared with the same curve reported by Bass et al. [11].

4.2.4 Discussion

The aim of this study was to determine the reproducible intra-aortic hydrostatic pressure value leading to rupture. An average threshold of 131.9 ± 11.8 kPa (989 ± 88 mmHg) was observed, with the small standard deviation showing that the resistance of aortic vascular tissue was substantially homogenous among subjects. The rupture location was most often found at the peri-isthmic region (44% of cases), confirming the vulnerability of the wall in this anatomical area. The Weibull distribution function provides a probability curve of rupture risk as a function of blood pressure. As shown in the Figure 4.7, beyond a blood pressure of 133 kPa (1001 mmHg), the risk of rupture becomes higher than 50%.

During the aortic burst tests performed in this study, an innovative way was used to prevent leakage by fitting a thin-layered latex tube in the aortic lumen. As previously reported [12], leakage is tough to avoid under physiological pressures solely with sutures and can be quite a problem under higher loadings. On one hand, our combined utilization of latex tube with sutures minimized leakage with a simple and reproducible procedure. On the other hand, the latex sheath has no significant influence on the accuracy of failure pressure measurement due to its much higher compliance than aortas (Figure 4.8 and Figure 4.6).

The mean value of aortic rupture pressures found in our study was 33.6 kPa higher than the previous value reported by Bass et al. [11]. The current Weibull injury risk for intraluminal pressure was also found more aggressive, with a 50% threshold pressure 32.5 kPa higher in our study. This was unexpected since the mean age of current subjects was 20.3 years higher, while the failure pressure of the same risk was previously suggested to be higher for younger populations [11]. To be noted, the time to aortic failure pressure in current tests averaged to be 2.3 s with a rate of 56.5 kPa/s (see Fig. 3), which was significantly lower than the rate of 720 kPa/s applied by Bass et al. [11]. Although the rate sensitivity of aortic failure pressure has never been studied, the failure stress was reported to increase with the increasing strain rate in previous aortic stretch tests [54, 55, 115]. The lower pressure rate resulting in lower strain rate in our study should have leaded to lower failure pressure than that in previously experiment [11], which nevertheless contradicted with our case. Additional aortic burst tests of the same age populations under different pressure rates may help to verify the data repeatability and the rate sensitivity of the failure pressure.

Conversely, in another experimental study using ten fresh porcine aortas, Pearson et al. [113] found much higher burst pressures than that obtained in our study. The burst tests were performed on the ascending aorta, aortic arch and descending aorta. The mean values of burst pressures for these segments were respectively 300 kPa, 287 kPa and 273 kPa, with no significant differences between each group. The differences observed may be mainly due to the tissue conservation methods (fresh tissue versus embalmed cadavers). Indeed, the compliance of fresh biological tissue has been suggested to be altered by the preservation method [116].

Subsequently, the question that can be raised is whether the threshold value measured here, 133 kPa (1001 mmHg), is a value that can happen in traffic accident situations. The answer to this question would provide more insights to the reasonability of the pressure-related BAR mechanism. In another experimental study, Hardy et al. [9] succeeded to reproduce BAR under a similar loading levels as MVCAs. Eight cadavers were infused at physiological pressure and impacted at an energy level equivalent to a MVCA at 30 km/h. Seven BAR resulted in the 8 tests, with the recorded intra-aortic pressure up to 165 kPa. This result therefore confirms the pressure level of 124 kPa can be reached in MVCAs. However, several factors that could increase BAR risks but were difficult to isolate during in situ tests include subject position, direction of shock, impact location, abdominal and thoracic compression [37, 117]. Our study avoids these uncertainties and isolates the stretching of the aortic wall due to inner pressure increase alone.

Our study has also several limitations:

> In our experiments, no blood flow was simulated and aortic wall was loaded with a uniform pressure of a limited increasing rate. The obvious advantage here is that the nature of the fluid exerting the loading on the wall has no influence on the loading magnitude and should only be seen as a loading medium, thus allowing us to use air instead of blood or any equivalent fluid. Still the threshold must only be considered as rather representative of the intrinsic characteristics of the aortic wall under hydrostatic conditions. The possible effect of fluid flow on aortic injuries should be the purpose of a further study, in order to fulfill the understanding of aortic injury mechanisms.

The aortas came from elderly subjects, probably with co-morbidities, and had multiple vascular calcifications. The biomechanics of the aged population could differ from those of the younger population without co-morbidities. Indeed, the aged population are less frequently injured than the younger in MVCAs, but the BAR of the elderly can cause higher mortality [106]. In addition, vascular senescence is characterized by thickening of the walls due to collagen proliferation, fragmentation of elastin fibers and mucopolysaccharides alteration, leading to vascular fibrosis. The resulting change in mechanical properties of the aorta probably underestimates our maximum pressure figures [118].

The preservation durations prior to dissection were not consistent from one cadaver to the other and were able to vary by up to several days. The effect of this duration on the aortas' biomechanical properties (elasticity, compliance) was difficult to exclude in our work.

A higher number of samples will make it possible to better characterize factors affecting results variability, such as gender or age. The locations of mechanical weakness, such as the isthmus that was found ruptured in this study in 44% of the cases would also be confirmed. Using fresh human aortas, obtained for example in the context of multi-organ donation, would also make it possible to avoid tissue conservation issues.

4.2.5 Conclusion

This study is a part of a larger project aiming at characterizing aortic injury mechanisms during high-speed body trauma. These injury mechanisms are complex, interacting with each other both in space and time. Excessive intra-aortic pressure is considered as among one of them and was explored in this study. The aortic rupture risk was found significantly high (higher than 50%) over a pressure of 133 kPa (1001 mmHg). This threshold was previously reported to be reachable in MVCAs. This injury mechanism is therefore probably playing a major role in the onset of traumatic aortic ruptures. In the field of fast growing virtual traumatology, injury criteria such as the here-proposed pressure threshold seem to be essential in order to make the models reliable and efficient in predicting aortic injury risk under impacts.

4.2.6 Author contribution

A.Culver and W.Wei contributed to study design, data collection, analysis, interpretation, writing and critical revision. M.Leone and T.Bege contributed to study design, writing and critical revision. M.Behr contributed to study design, analysis, interpretation, writing and critical revision.

4.3 Article #3: Intraluminal Pressure Should be Considered for Blunt Aortic Rupture Prediction in Car Crash Accidents: a Numerical Analysis

This article entitled "Intraluminal Pressure Should be Considered for Blunt Aortic Rupture Prediction in Car Crash Accidents: a Numerical Analysis" was submitted to the Traffic Injury Prevention Journal on 8th April, 2018. It was still under review at the time this thesis was written.

Wei Wei[1,*], Aurélien Culver[1], Morgane Evin[1], Cyril J.F. Kahn[1], Michel Behr[1]

[1] *Aix-Marseille Université, IFSTTAR, LBA UMR T24, Marseille, France*

Abstract

Objective: The role of fluid-structure interactions in blunt aortic rupture (BAR) in car crashes remains unclear. Moreover, blood pressure is often neglected or over-simplified when predicting the risk of BAR in literature. In this study, the necessity of considering pressure for an accurate prediction of BAR risk in car crashes was investigated.

Methods: In a preliminary step, the possible influence of pressure on aorta mobility was assessed, as mobility and BAR risk may be related according to recent literature. Thus, mini-sled tests were performed with 7 cadaveric aorta specimens on a custom platform. The aortas were pressurized at two different levels: a low physiological level of 50mmHg and a high physiological level of 200mmHg. Then, a single oblique-frontal real car crash case involving BAR was extracted from the CIREN database and reconstructed. The reconstructed accelerations were imposed as boundary conditions in a finite element simulation involving a car environment and the GHBMC human model. The consistency of the models was evaluated by comparing car intrusions and occupant injuries recorded in the simulation with the case records. Finally, the intraluminal pressure was recorded and compared with the pressure threshold expected to induce aorta failure as reported in literature.

Results: In the preliminary tests, mini-sled accelerations were found reproducible for all the aortas, and aortic deflections were found significantly affected by the initial pressure level. The frontal car intrusions reconstructed from the car crash simulation were consistent with the real case report. The occupant model predicted bilateral rib fractures and lung contusion, which was also consistent with the case injury report. A peak blood pressure of 135kPa was predicted in the aorta, corresponding to an estimated BAR risk of 91%.

Conclusion: Intraluminal pressure had significant effects on the aortic mobility. The intraluminal pressure occurring in BAR-related accidents could induce significantly high BAR risks. Intraluminal pressure is therefore a critical factor to be considered for BAR prediction in car crash accidents and is a relevant parameter to be used in BAR risk criteria definition.

Keyword: Blunt aortic rupture, Intraluminal pressure, Aortic mobility, Injury risk, Car crash accidents

4.3.1 Introduction

Blunt aortic rupture (BAR) is the second leading cause of death following blunt trauma in motor vehicle crash accidents (MVCAs) [4]. The majority of BARs occurring in MVCAs were found in vehicle occupants (53.5%), followed by pedestrians, motorcyclists, bicyclists and truck occupants [3]. BAR often leads to fatality with 85% of the victims deceased at the collision scene [5]. If untreated, 30% of the remaining injured will decease within 24 hours [5]. Various aortic injury mechanisms have been previously proposed and can be categorized into two sources of contribution: intraluminal pressure [8] and aortic distraction [6, 7]. The aortic distraction is related to aortic motions resulting from thoracic compression and was postulated to be a primary BAR mechanism [9, 10]. However, the pressure effects on BAR remain to be controversial. Bass et al. [11] proposed a pressure-based injury index with a 101kPa threshold for 50% BAR risk. Forman et al. [12] suggested intraluminal pressure should only be a secondary mechanism due to the limited pressure gradient across the aortic wall during sled tests. Hardy et al. [9] further argued blood pressure seemed unlikely to cause BAR alone considering the typical transverse rupture in MVCAs and Young-Laplace equation [119].

In previous numerical researches, discrepancies also existed in the choices of accounting for blood pressure effects. Richens et al. [17] did not consider the contribution of blood pressure to aortic wall stress levels in crash simulation. Siegel et al. [19] assumed a static blood pressure uniformly distributed inside the aorta and got a maximum pressure of 176.3kPa in lateral crash simulation. Their approaches of simulating blood pressure were simplified to some extent, since the pressure profile is pulsatile during cardiac cycle and inhomogeneous in the aortic lumen. However, it is difficult to judge whether this simplification impaired the BAR prediction in the simulation before we ascertained the effects of intraluminal pressure on BAR in MVCAs.

In this context, the role of fluid-structure interactions in blunt aortic rupture (BAR) in car crashes remains unclear. Here, the relevance of considering pressure for an accurate prediction of BAR risk in car crashes was investigated. In particular, preliminary experiments were performed by comparing the aortic deflections in mini-sled tests under two pressure levels. Then, an oblique-frontal real crash case involving BAR was reconstructed to acquire aortic blood pressure information in MVCAs and estimate whether pressure is a relevant risk factor or not.

4.3.2 Methods

Preliminary tests

Seven fresh cadaveric aortas (2 males and 5 females; mean age 88±9 years; detailed sample information in Table O1 of APPENDIX O) from aortic root to T8 vertebra level were harvested as a part of a protocol for body donation to science approved by the Ethics Committee of the Faculty of Medicine of Marseille (France). The subjects had no reported cardiovascular disease or trauma history. All the specimens were soaked in saline water and stored with a rapid freezing technique. The extra-aortic tissue was removed after the samples were thawed to room temperature prior to testing. Surgical sutures (0.5mm in diameter) were made at the incisions of coronary, supra-aortic and intercostal arteries. A medical latex tube (0.1mm thick) was fit inside the aortic lumen. Using latex tube (see Figure 4.9) is an original approach to better prevent fluid leakage during pressurization period as compared to the traditional way of solely making sutures

[11] which often suffers from leakage under high pressure levels. More detailed information (diameters and lengths) of the harvested aortas is summarized in Table O1 of APPENDIX O.

Each aorta was fixed on a mini-sled (Figure 4.9) at the aortic root level with its physiological posture to avoid pre-deformation. After air was removed from the system (displayed in Figure 4.9) by water circulation with the flow pump (10-00-00 heart pump, Stockert Instrument, Freiburg, Germany), all the taps except 2 and 4 were closed. The aorta sample was first pressurized at 6.7kPa, corresponding to a low (50mmHg) physiological pressure level. This pressure was adjusted by varying the vertical water column height and checking the pressure sensors (EPX, TE connectivity, Schaffhausen, Switzerland),. After ensuring no leakage in the system, tap 2 and 4 were also closed. The pendulum was released from a specific height (corresponding to 20° on the dial, hereafter referred as *Impact-20°*). This pendulum initial height was set arbitrarily after several height values were tested, because it would lead to reasonably great deflections. The mini-sled acceleration was recorded by a triaxial accelerometer (EGAS model, TE connectivity, Schaffhausen, Switzerland) while the aortic deflection along the sled travelling direction (hereafter referred as deflection for simplification) was captured by a high-speed camera (Fastcam SA3 model 120K, Photron, Tokyo, Japan). The whole process was then repeated with an initial pressure of 26.7kPa, corresponding to a high (200mmHg) physiological pressure level.

In order to confirm the possible effect of pressure even for low impact energy levels, the trial was then repeated with the same aorta sample, at both initial pressure levels, for a lower pendulum height (corresponding to 10° on the dial and hereafter referred as *Impact-10°*). For both impact energy levels, aortic arch deflections under the two pressure levels were compared to evaluate the pressure effects on aortic mobility. Peak accelerations of the mini-sled under 50mmHg and 200mmHg were always verified to be equivalent within a range of 1% for the same aorta under the same impact energy level. Otherwise, another trial was conducted until a reasonable match was achieved for the peak accelerations. In this way, the potential deflection modifications caused by acceleration discrepancies could be excluded or reduced as possible.

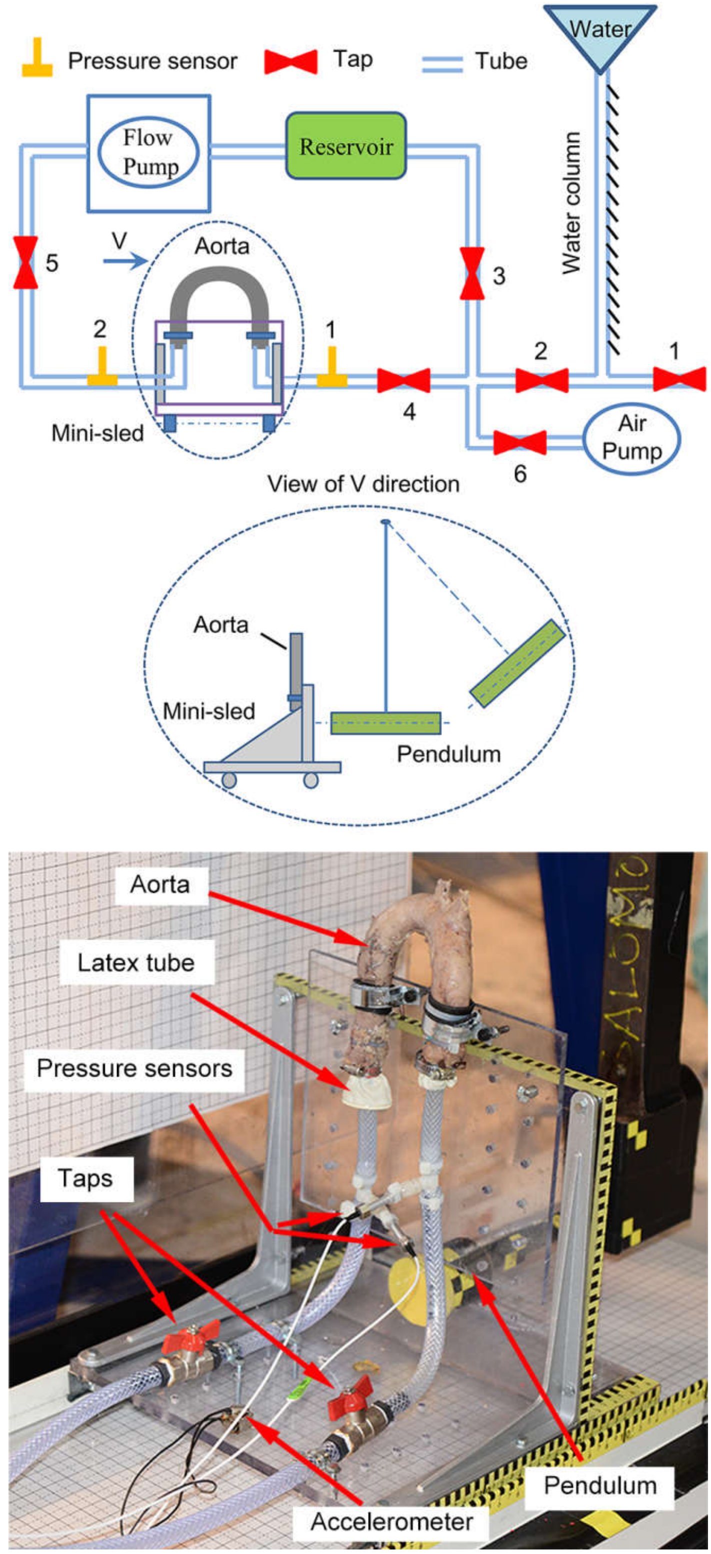
Pressure sensor
Tap
Tube
Water
Flow Pump
Reservoir
Water column
V
Aorta
5
2
1
3
2
1
4
Mini-sled
Air Pump
6
View of V direction
Aorta
Mini-sled
Pendulum
Aorta
Latex tube
Pressure sensors
Taps
Pendulum
Accelerometer

Figure 4.9: Platform configuration of mini-sled test

BAR case reconstruction

One oblique-frontal crash case involving BAR was selected and obtained from the Crash Injury Research and Engineering Network (CIREN) database. In the real case, the vehicle (2004 Honda Civic) impacted a concrete traffic barrier at its front bumper at an estimated speed of 55km/h, with a principal direction of force of 340 degrees. The victim (36 year-old male, 173cm and 64kg) was seated at the second row left and restrained by a 3-point seatbelt without airbag available in the accident. He survived but suffered from aortic arch transection, lung contusions and/or laceration, bilateral rib fractures, and skin contusions (see Table D1 in APPENDIX D). The reason for choosing this case was the car type and occupant morphology were similar to those of the available vehicle and occupant finite element (FE) models, i.e. respectively a 1996-year Dodge Neon and the Global Human Body Model Consortium (GHBMC). See Table D1 and Table D2 in APPENDIX D for details of these 2 models.

The case reconstruction analysis was performed in two stages: vehicle-barrier crash simulation followed by the sub-simulation of occupant interacting with the restraint system. For stage 1, the FE models of 1996-year Dodge Neon and concrete barrier, released and validated by the National Highway Traffic Safety Administration (NHTSA), were used to simulate the collision scene (see Figure 4.10). The vehicle imposed initial velocity was set to 55km/h according to the case description. Initial velocity was preferred to the change in velocity (delta-V) as delta-V of the vehicle could not be estimated in the accident, since the initial vehicle-barrier relative position or the post-impact barrier movement was uncertain. Since the initial vehicle-barrier relative position was not reported, the FE simulation was iteratively repeated, tuning the barrier-vehicle angle until a reasonable match was obtained for the case vehicle deformations measured according to the collision deformation classification (11FDEW03) [120]. The acceleration time-history was recorded by the tri-axial accelerometer fixed at the left-rear passenger seat and was used as input for stage 2 simulation.

For stage 2, the GHBMC M50 human model (V4.4; Elemance, Winston-Salem, USA) was positioned and belted in a car cockpit environment, firstly dropped onto the deformable seat under gravity loading. This simulation terminated until equilibrium in contacts between the occupant and the vehicle components (seat and floor) was reached. A seatbelt with 6kN-load-limit retractor was then created and fit to the occupant’s chest and abdomen as previously described in [121]. The crash acceleration loadings obtained from stage 1 were finally applied to restrained occupant model (Figure 4.10). Meanwhile, the initial stresses due to occupant-seat/floor contact were also inherited from the previous occupant drop simulation.

The occupant impact simulation was evaluated against the case injury descriptions in terms of stress and strain for the thoracic organs (e.g. aorta, lungs and ribs). The simulated aortic blood pressure was also compared with the reported pressure threshold inducing aortic rupture [11] to estimate the pressure-resulted BAR risk in this case. All of the simulations were performed with the solver LS-DYNA 971 R7.1.1 (LSTC, Livermore, CA, USA).

For practical reasons, because the Dodge Neon model used here had no detailed interior components, the seat and floor models were extracted from a 2012-year Toyota Camry FE model also released by NHTSA. It is assumed that the geometry of this interior is similar to that of the case vehicle (Honda Civic), as both cars are of the same category. In order to further compare injuries with the case medical report, stress and strain levels in the thoracic organs (e.g. aorta, lungs and ribs) were recorded in the simulation. The simulated aortic blood pressure was also compared with the reported pressure threshold inducing aortic rupture previously reported in [11] to estimate the pressure-resulted BAR risk in this case. All of the simulations were performed with the LS-DYNA 971 R7.1.1 solver (LSTC, Livermore, CA, USA).

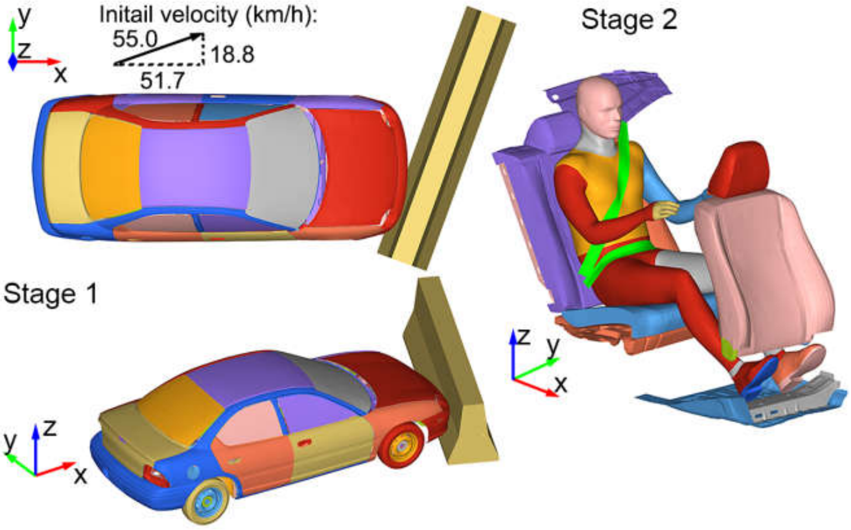

Figure 4.10. Simulation setup for car crash reconstruction: vehicle-barrier crash (stage 1) and occupant-seat impact model (stage 2)

4.3.3 Results

Preliminary tests

The average pendulum velocity at the moment of impact was 1.5±0.1m/s for Impact-20° and 0.7±0.1m/s for Impact-10°. Considering the mass and the post-impact velocity of pendulum, the impact energy resulted in 10.8±2.3J for Impact-20°and 2.4±0.5J for Impact-10°, which was nearly the energy transferred directly to the sled and aortas. The mini-sled mean accelerations versus time and the corresponding experimental corridors for *Impact-20°* and *Impact-10°* were displayed in Figure E1 (APPENDIX E), which were acquired with the same approach as previously reported in [114] and based on accelerations filtered from the raw experimental data with SAE CFC 180. The mini-sled accelerations were reproducible for all the aortas, with the mean values of the peak accelerations recorded as 16.0±2.1g and 7.2±0.8g 16.0±2.1g and 7.2±0.8g respectively for *Impact-20°* and *Impact-10°*.

The *deflection* time-history under 50mmHg and 200mmHg during *Impact-20°* and *Impact-10°* was displayed in Figure 4.11a for Aorta-3 and in Figure F2 (APPENDIX F) for the other aortas. The *deflection* measuring approach was detailed in APPENDIX F. During sled tests, the aorta experienced two phases: the bending phase due to inertia and the rebounding phase due to aortic elasticity. The peak deflections of all the aortas were displayed in Figure 4.11b for *Impact-20°*and Figure 4.11c for *Impact-10°*. For *Impact-20°*, the mean values of peak deflections were 3.7±1.8cm and 2.4±0.9cm respectively under 50mmHg and 200mmHg. For *Impact-10°*, the corresponding values were 1.9±1.0cm and 1.1±0.5cm under 50mmHg and 200mmHg. In both impact energy levels, the aortic deflections under 50mmHg were correlated (r=0.953 for *Impact-20°* and p= 0.907 for *Impact-10°*) with and significantly higher than the deflections under 200mmHg (p=0.010 for *Impact-20°* and p= 0.013 for *Impact-10°*), which were results of paired t-tests against pressure levels.

Oblique-frontal crash reconstruction

In stage 1, the simulated vehicle deformations (Figure G1 in APPENDIX G) were compared with the case vehicle damage profiles. Table 4.2 displayed the frontal intrusions which were referred as C1-C6 and were measured with the same protocols (11FDEW03) as reported in CIREN database. The acceleration time-histories recorded at the left-rear seat of stage 1 were displayed in Figure G2 (APPENDIX G) which were applied as the input of stage 2.

In stage 2, the lungs and the aorta were found to reach their peak value of maximum principal strain and VonMises stress respectively at the same time t=100ms (displayed in Figure 4.12). The effective plastic strains of ribs at t=100ms are displayed in Figure 4B. The aortic blood pressure also came to the peak value of 135kPa (displayed in Figure 4.12B) at t=100ms. The strain, stress and pressure displayed here are averaged values of the surrounding elements sharing a common node.

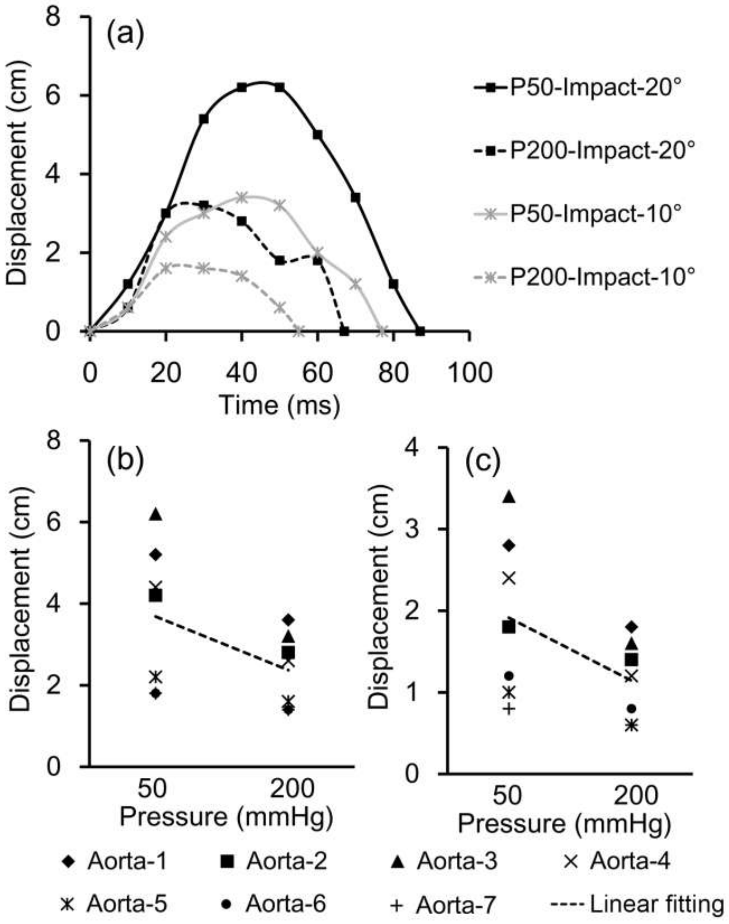

Figure 4.11. Aortic deflections in mini-sled tests: deflection time-history of Aorta-3 (a) where P-50 and P-200 correspond to pressure 50mmHg and 200mmHg; peak deflections of all the aortas for *Impact-20* (b) and for *Impact-20°* (c)

Table 4.2. Intrusions of frontal crash reconstruction compared with case vehicle crush profiles

Deformation (cm)	C1	C2	C3	C4	C5	C6	Average difference (%)
Case	20	28	41	49	50	55	--
Simulation	25	31	43	48	52	54	--
Difference (%)	25.0	10.7	4.9	-3.2	2.0	-1.8	8.5

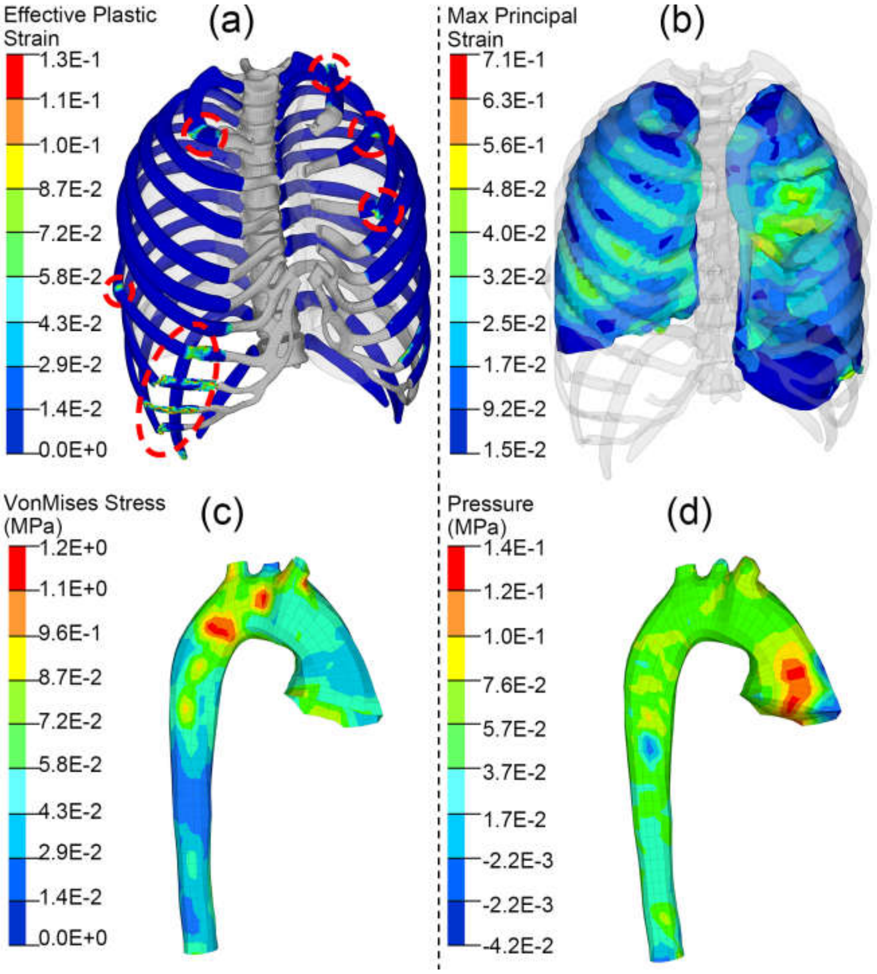

Figure 4.12. Simulation results of occupant injuries: contour plots of effective plastic strains for ribs (a), max principal strain for lungs (b), VonMises stress for aorta (c) and blood pressure recorded in aorta (d) at t=100ms in stage 2

4.3.4 Discussion

Aortic mobility modification

For *Impact-20°* or *Impact-10°*, the aortic deflections were found higher under 50mmHg than the deflections under 200mHg (see Figure A3). The mean values of peak deflections under 50mmHg were 54.2% (for *Impact-20°*) and 72.7% (for *Impact-10°*) higher than those under 200mmHg. Of course these deflection magnitudes should not be considered as those experienced by aortas in real intra-thoracic conditions, for two main reasons: there are no surrounding organs limiting (or increasing) somehow the movements of the aortic arch; the tests do not reflect the realistic anatomic constraints of aorta (e.g. tethering from the superior aortic branches and ligamentum arteriosum).

Apart from the deflection magnitudes, the durations of deflection pulses were also 5-32ms (*Impact-20°*) and 5-30ms (*Impact-10°*) longer under lower pressure than those under higher pressure. In other words, the aortic mobility was significantly modified by the pressurization levels. This was attributed to the nonlinear hyperelastic material properties of aorta, which displayed higher stiffness at higher strains [74, 86]. This is also supported by results reported in [122], where the slope of the pressure-strain curve was found to be 10 times greater at 27kPa than at 7kPa in conditions of aortic pressure-inflation tests.

Among the studies having investigated BAR mechanisms in MVCAs, some researchers speculated the sudden stretch of aorta due to relative displacements among different aortic segments should account for the injuries [16, 59, 123]. Other studies further proposed the thoracic deformation leading to aortic distraction was critical for reproducing BAR in experimental environments [9, 10]. These previous studies altogether indicated the difference in mobility between the relatively free aortic arch and the constrained descending aorta played an important role in BAR. To some extent, our finding of aortic mobility modified by intraluminal pressures could indirectly justify the aortic pressurization should be considered when studying BAR in MVCAs. Indeed, previous researches focused on the aortic stress levels directly imposed by intraluminal pressure loadings [19, 21] while our study might also provide another perspective in analyzing pressure effects on aortic kinematics for BAR research.

The preliminary tests have several limitations. First of all, the initial pressures correspond to a low and a high physiological value, but are far from those values expected in MVCAs, in particular such as that recorded during the oblique-frontal crash simulation (135kPa). Aorta tissue was very vulnerable in the conditions of our tests and the risk of leakage in the suture region was found very high with pressures greater than 200mmHg. In order to avoid misreading of the pressure values due to possible leakage in the system, it was therefore decided to limit our observations to a maximum pressure of 200mmHg. Still, what could be observed at low pressures, i.e. the aortic arch deflection inversely correlated to pressure, is assumed to remain true for higher pressure values.

Second, the sample group of 7 aged aortas (88±9 years) is another limitation in this study. Since the aortic wall stiffness was previously reported to increase with age [124, 125], the aortic deflections in this study only mimic the aortic mobility of the aged population (above 70 years), instead of young adults, under the experimental scenarios. The aortic deflections should be higher for the young populations under the same conditions as the current mini-sled tests. However, if this limitation probably affects the deflection magnitude, aortic mobility should still be considered to be significantly modified by pressure, independent of age.

Pressure-resulted BAR risk

To evaluate the BAR risk induced by intraluminal pressure, the first step would be to estimate what peak pressure could be expected in MVCA conditions. This can be achieved by reconstructing real accidents with numerical simulations. Lateral collisions involving BAR were previously reconstructed with the mean value of peak pressures reported as 153.2kPa in [19] and 117.0kPa in [21]. BAR was reported to occur in both frontal and lateral collisions, although it is still uncertain whether BAR occurs more frequently in one particular impact direction [19, 21, 126]. To supplement intraluminal pressure information for frontal crashes, an oblique-frontal crash case involving BAR was reconstructed in our study.

In reconstruction stage 1, the simulated frontal deformations were similar with the case deformation patterns (Figure A4) with an average intrusion difference of 8.5% and a maximum difference of 25.0% (Table 1). The simulated crush profiles were considered to reasonably match the case vehicle damage according to the previous evaluation for later collisions [21].

The passenger injuries were evaluated in stage 2 under the acceleration pulses with a peak resultant magnitude of 28.9g captured in stage 1. The GHBMC M50 model reproduced multiple rib fractures (e.g. left rib 1-3, right rib 1 and 7-9) (Figure 4) due to excessive seatbelt contact force and chest compression. The peak max principal strain of 0.71 occurred at the left lung root where pulmonary arteries start, indicating this area had high risks of contusion according to the pulmonary injury thresholds proposed in [127, 128]. The peak stress of 1.24MPa at the posterior aortic arch suggested a higher BAR vulnerability at this region, referring to the aortic stress levels reproduced in lateral collisions[19] and the failure stresses recorded in dynamic stretch tests [52]. All the injuries detailed here above and predicted by the model agree well with the case injury descriptions of bilateral rib fractures, pulmonary contusion and aortic arch transection.

As previously mentioned, the peak intraluminal pressure of this case was predicted to occur at the aortic root with a value of 135kPa. This peak pressure was within the ranges reported for lateral impacts [19, 21]. Bass et al. [11] proposed a pressure-based injury risk curve, hereafter refereed as Bass curve, with a 101kPa threshold for 50% BAR risk. Similarly, another unpublished study of our project obtained a 133.5kPa threshold for 50% risk. According to Bass curve, the BAR risk corresponding to an intraluminal pressure of 135kPa is 91%.

On one hand, the value of 135kPa recorded in our simulation may be slightly underestimated (and consequently, the BAR risk underestimated as well) due to the lack of actual blood flow, suppressing the so-called water hammer effect [129]. The water hammer effect is due to sudden blood flow occlusion and could cause a pressure elevation of up to 36.8kPa according to the Joukowsky equation [130] if assuming average blood velocity 1.0m/s, upstream aortic length 0.2m, blood pressure 16.0kPa and aorta occluded within 50ms. This added pressure may be insufficient to cause BAR alone but would help to elevate the injury risk from 91% to 99% in our accident case.

On the other hand, the Bass curve was built with old cadaver specimens, whereas it is admitted that risk is lower in younger population [11]. In our case report, the victim was 38 years old, which means that we may be, on the opposite, overestimating the BAR risk, in a proportion difficult to quantify due to the lack of data on young subjects.

Extra-aortic pressure might be another factor conducive to counteracting luminal pressure and reducing BAR risks as reported in [12] where the intra-thoracic pressure was recorded for the first time in sled tests. However, their using tracheal and esophageal pressures to represent extra-aortic pressure remains to be discussed, mostly due to experimental protocol limitations such as sensors locations, initial pressurization and inhomogeneity of the thoracic cavity.

The possible high pressure-induced BAR risks in frontal and side impacts justified the necessity of considering intraluminal pressure for BAR mechanism studies. This should be achieved ideally by simulating cardiac blood flow instead of imposing a uniform static pressure in the aorta to involve both hydrostatic pressure and water hammer effect. Even if intraluminal pressure was proved to be offset by comparable extra-aortic pressure in collisions, it is still essential, in authors' opinion, to consider pressure distributions inside and outside aorta for BAR researches.

4.3.5 Conclusions

Mini-sled tests were performed with seven cadaveric aorta samples (88±9 years) under two pressure conditions, both for two impact energy levels resulting in sled acceleration ranges of 11.7-20.2g for *Impact-20°* and 5.6-8.8g for *Impact-10°*. The peak aortic deflections were 1.9±1.0cm and 1.1±0.5cm respectively under 50mmHg and 200mmHg for *Impact-10°,* while the corresponding values were 3.7±1.8cm and 2.4±0.9cm for *Impact-20°*. The aortic deflections under 50mmHg pressurization were correlated with and significantly higher than the deflections under 200mmHg for both impact energy levels. Although the aortic deflections only represented the aortic mobility for the aged population under the experimental conditions, the significant effects of pressure levels on aortic mobility should remain true for the young adults.

One oblique-frontal car crash involving BAR from CIREN database was also reconstructed with the vehicle model frontal intrusions consistent with the case report. The occupant model predicted bilateral rib fractures and lung contusion, also consistent with the case injury report. A peak intraluminal pressure of 135kPa was predicted in this oblique-frontal impact case. The estimated intraluminal pressures in current oblique-frontal case and previous lateral collisions could induce high risks of BAR according to the Bass curve. Combining the aortic mobility modified by pressurizations and the high BAR pressure-related risks in collisions, intraluminal pressure should be paid attention to during BAR studies for MVCAs. This viewpoint would not be impaired even if the extra-aortic pressure was proved to counteract the intraluminal loadings, since the pressure distributions should be considered for both interior and exterior aorta in this condition.

4.3.6 Conflict of interest

None

4.3.7 Acknowledgements

The authors would like to thank GHBMC for providing the academic license for using GHBMC model.

CHAPTER 5 FSI SIMULATION OF AORTIC BLOOD FLOW DURING CARDIAC CYCLE AND MVCA

5.1 Introduction

The aortic loading responses during cardiac cycles were evaluated in Chapter 3. To briefly review, the peak VonMises stress of aortic wall was 0.51MPa while the peak stretch ratio was respectively 1.48 and 1.41 for circumferential and longitudinal directions. The aortic stress under cardiac function was comparable with the corresponding magnitudes reconstructed in car crash simulations [17, 19, 21, 101]. The aortic stress and stretch ratio were also respectively 28.3%~29.8% and 67.1%~70.5% of the aortic failure thresholds according to the data in literature [98, 100]. Therefore, the aortic loadings due to cardiac cycle should be considered (and therefore not neglected) in MVCA-related BAR mechanism researches.

The necessity of considering intra-aortic pressure during BAR researches for MVCAs was also emphasized in Chapter 4 from two perspectives. On one hand, different luminal pressure levels were found to affect aortic mobility significantly in Chapter 4.3. The aortic mobility is relevant with the commonly admitted BAR mechanism of aortic distraction resulting from thoracic compression in MVCAs. In other words, intra-aortic pressure level could also affect the possibility of aortic injury by influencing aortic mobility during MVCAs. On the other hand, the intra-aortic pressure was found to reach 135kPa in a reconstructed BAR case with a human FE model which simplified aortic blood modeling without simulating blood flow. Compared to the pressure levels (133.5kPa obtained in Chapter 4.2 and 101kPa in [11]) leading to a BAR risk of 50%, the aortic luminal pressure, which was considerably elevated by impact loadings, could induce a high risk of BAR. Furthermore, the possible water hammer effect due to sudden blood flow occlusion was also estimated, together with which the aortic injury risk resulting from intra-aortic pressure alone would reach up to 99%.

Combining the context above, a promising way to consider intra-aortic pressure for MVCA-related BARs is to simulate the aortic blood flow during the cardiac cycle instead of filling the entire aorta with an uniform static pressure as previously done in [19, 21]. Before developing the aortic FE model to simulate the cardiac blood flow, it is necessary to have more knowledge of cardiac-related anatomy and physiology as well as the simulation approaches available in the commercial solver of LS-DYNA.

5.1.1 Anatomy

Heart

The heart is a valved muscular organ in humans and other animals. The heart pumps blood through the blood vessels of the circulatory system to supply the body with oxygen and nutrients as well as to remove metabolic wastes.

The heart is located in the middle of the mediastinum above the diaphragm behind the breastbone in the chest, at the level of thoracic vertebrae T5-T8 (see Figure 5.1). The large part of the heart is usually slightly shifted to the left, though the heart may sometimes be shifted to the right. Since the left part of heart pumps to all body parts and it is stronger, the heart is usually felt to be on the left side. The left lung in turn is smaller than the right lung because it has to accommodate the heart. The heart is supplied by the coronary circulation and is enclosed in the pericardial sac.

The pericardium encloses the heart and also attaches to the mediastinal fascia, thus ensuring anchorage to the heart. The back surface of the heart lies near to the vertebral column, and the front surface sits deep to the sternum and costal cartilages. The base of the heart (i.e. the upper surface of the heart), which is located at the level of the third costal cartilage, attaches the great veins, the superior and inferior venae cavae, and the great arteries, the aorta and pulmonary trunk. The heart apex (i.e. the lower tip of the heart) lies close to the left of the sternum between the junction of the fourth and fifth ribs near their articulation with the costal cartilages. The right side of the heart is deflected forwards with the left side deflected to the back.

The heart has two upper atria and two lower ventricles which respectively receive blood from the veins and discharge into the arteries (see Figure 5.2). The atria are connected to the ventricles by the atrioventricular valves and are separated by the coronary sulcus. The right atrium receives deoxygenated blood from the body and the left atrium receives oxygenated blood from the lungs. The right atrium and the right ventricle, which are separated by tricuspid valve, constitute the right heart. The left atrium and the LV, which are separated by mitral valve, constitute the left heart. The left and right hearts are separated by the atrioventricular septum. As two independent functional units, the left heart pumps to the systemic circulation and the right heart pumps to the pulmonary circulation.

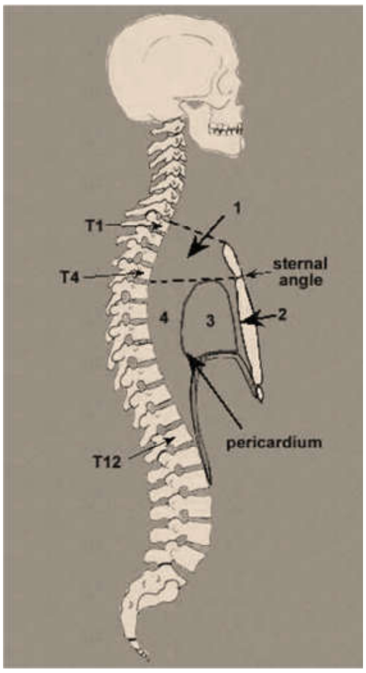

Figure 5.1 Subdivision of mediastinum as seen on sagittal section: (1) superior mediastinum (2) anterior mediastinum (3) medial mediastinum (4) posterior mediastinum (adapted from https://home.comcast.net/~wnor/thoraxlesson3.htm)

Brachiocephalic trunk

The brachiocephalic trunk is also referred as brachiocephalic artery or innominate artery. It is the first and the largest branches of the aortic arch. It arises from the commencement of aortic arch slightly posteriorly and to the right. The brachiocephalic trunk divides into the right common carotid artery and the right subclavian artery at the level of the upper edge of the right sternoclavicular joint. These arteries mainly supply blood for the right arm and the right side of head and neck.

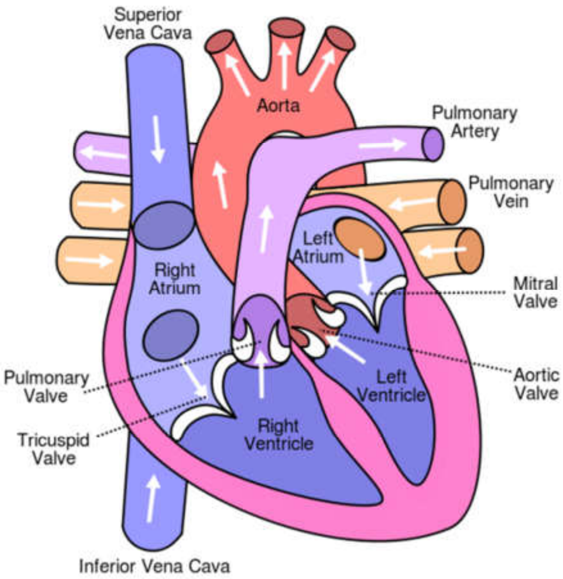
Superior Vena Cava
Aorta
Pulmonary Artery
Pulmonary Vein
Left Atrium
Right Atrium
Mitral Valve
Aortic Valve
Pulmonary Valve
Left Ventricle
Right Ventricle
Tricuspid Valve
Inferior Vena Cava

Figure 5.2 Schematic of the heart showing valves, arteries and veins (The white arrows shows the normal direction of blood flow) (adapted from http://en.wikipedia.org/wiki/Heart)

Left common carotid artery

The left common carotid artery is the second branch of aortic arch. It arises from the aortic arch in the thoracic region, immediately to the left and slightly posterior to the brachiocephalic trunk, and ascends through the superior mediastinum along the left side of the trachea. The left common bifurcates into the external and internal carotid arteries at the upper border of the thyroid cartilage around the level of the fourth cervical vertebra (C4), supplying oxygenated blood for the left side of the head and neck.

Left subclavian artery

The left subclavian artery is the third branch of aortic arch. It arises from the arch immediately to the left of and slightly posterior to the left common carotid artery. It then ascends through the superior mediastinum along the left side of the trachea. The left subclavian artery receives oxygenated blood from the aorta and supplies to the left arm.

Ligamentum arteriosum

The ligamentum arteriosum (also referred as arterial ligament) is a small ligament connecting the superior surface of the left pulmonary artery with the proximal DA. It is a nonfunctional vestige of the ductus arteriosus, which closes soon after birth. This ligament was postulated to play a role in major trauma, since it fixes the aorta in place during rapid decelerations recoil and consequently causes BARs in MVCAs.

Coronary arteries

Coronary arteries are the vessels that convey oxygen-rich blood to the myocardium, which is an important part of coronary circulation. There are two kinds of coronary arteries, the left and right coronary artery, running on the surface of the heart. Both kinds of coronary arteries originate at AR, just after the aorta extends from the LV (see Figure 5.3). The left coronary artery commences at the left aortic sinus, while the right one begins at the right aortic sinus.

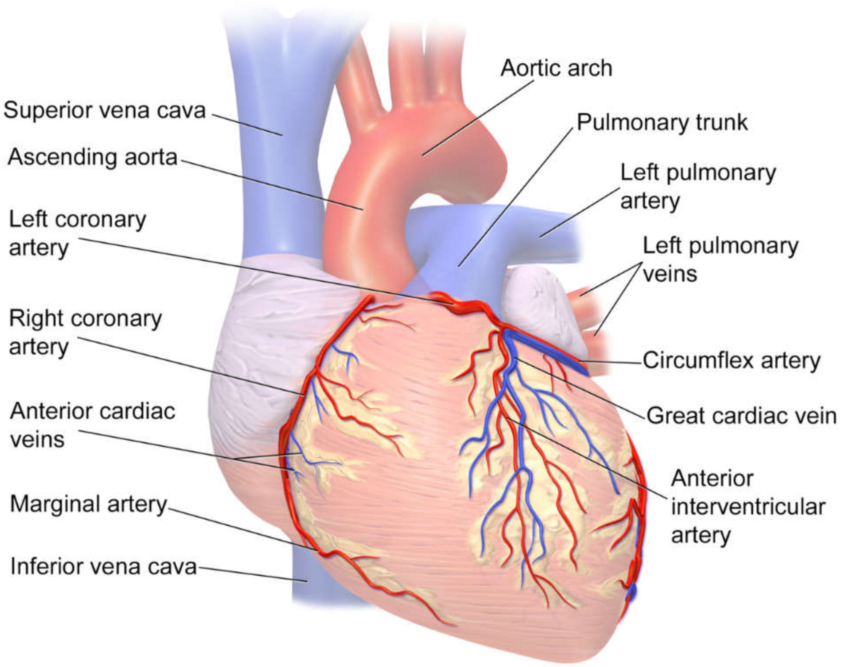
Aortic arch
Superior vena cava
Pulmonary trunk
Ascending aorta
Left pulmonary artery
Left coronary artery
Left pulmonary veins
Right coronary artery
Circumflex artery
Great cardiac vein
Anterior cardiac veins
Anterior interventricular artery
Marginal artery
Inferior vena cava

Figure 5.3 Anterior views of coronary circulation (adapted from http://en.wikipedia.org/wiki/ Coronary_ circulation)

5.1.2 Physiology

A cardiac cycle consists of two basic phases: diastole and systole. Diastole corresponds to the duration when the ventricles are relaxed (not contracting). During most of the diastole, the blood flows through mitral and tricuspid valves from the left atrium and right atrium into the LV and right ventricle, respectively (see Figure 5.4). The right atrium receives venous blood from the body through the superior vena cava and inferior vena cava. The left atrium receives oxygenated blood from lungs through four pulmonary veins that enter the left atrium. At the end of diastole, both atria contract to push an additional amount of blood into the ventricles.

Systole corresponds to the duration when LV and right ventricle contract to eject blood into the aorta and pulmonary artery through the aortic and pulmonic valves, respectively. During systole, mitral and tricuspid valves are closed to prevent blood from entering the ventricles while the blood continues to enter the atria though the vena cava and pulmonary veins.

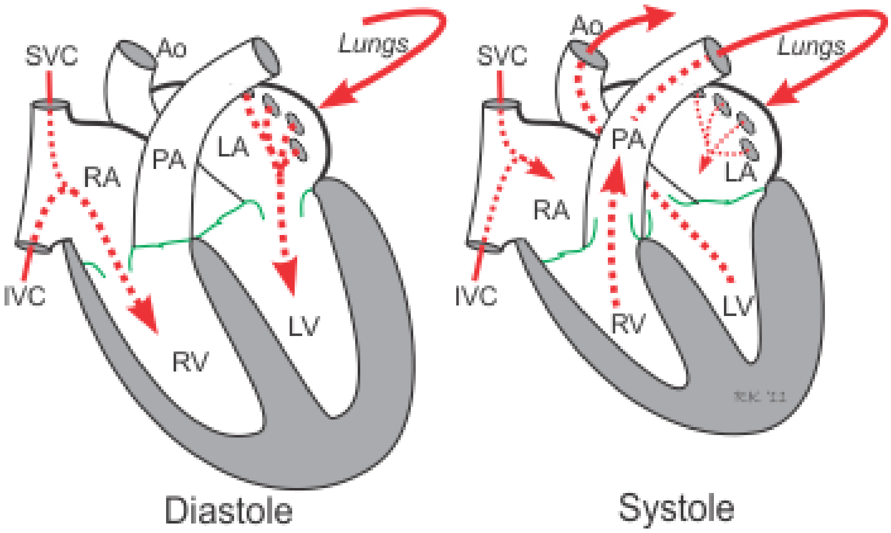

Figure 5.4 Blood flow patterns of cardiac cycle (adapted from http://www.cvphysiology.com/Heart%20Disease/HD002.htm). Ao: aorta; IVC: inferior vena cava; LA: left atrium; LV: left ventricle; PA: pulmonary artery; RA: right atrium; RV: right ventricle; SVC: superior vena cava.

As presented in Figure 5.5, the aortic pressure, left ventricular pressure, left atrial pressure, LV volume and heart sound always change during the cardiac cycle. These changes are related in time to the electrocardiogram. A single cardiac cycle can be divided into seven phases:

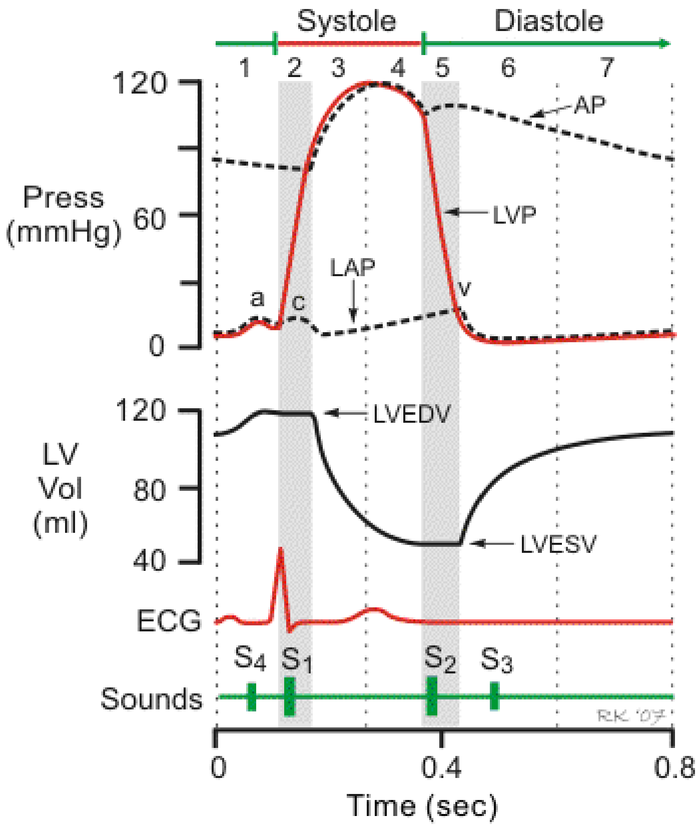

Figure 5.5 Time history of blood pressure and volume during a single cardiac cycle (AP: aortic pressure; LVP: left ventricular pressure; LAP: left atrial pressure; LVEDV: the left ventricular end-diastolic volume; LVESV: the left ventricular end-systolic volume; ECG: electrocardiogram) (adapted from http://www.cvphysiology.com/Heart%20Disease/HD002.htm)

- Phase 1-Atrial Contraction (mitral and tricuspid valves Open; aortic and pulmonic valves closed);
- Phase 2-Isovolumetric Contraction (all valves closed);
- Phase 3-Rapid Ejection (aortic and pulmonic valves open; mitral and tricuspid valves remain closed);
- Phase 4-Reduced Ejection (aortic and pulmonic valves open; mitral and tricuspid valves remain closed);
- Phase 5-Isovolumetric Relaxation (All Valves Closed);

- Phase 6-Rapid Filling (mitral and tricuspid valves open, aortic and pulmonic valves remain closed);
- Phase 7-Reduced Filling (mitral and tricuspid valves open, aortic and pulmonic valves remain closed).

More detailed information about the seven phases of cardiac cycle could be found on the website: http://www.cvphysiology.com/ Heart%20Disease/HD002.htm.

5.1.3 FSI approaches in LS-DYNA

FSI is one of the three numerical simulation categories (i.e. structural analysis, computational fluid dynamics (CFD) and FSI) which LS-DYNA can perform [131]. These simulation approaches have their particular applications and focus, depending on targeted media. Structural analysis is commonly used to understand and predict the behavior and response of a solid system during its whole duration when it is exerted to loads. CFD is widely to solve the problems dealing with a geometrically fixed fluid domain. CFD has difficulties in obtaining accurate results when the geometry of the fluid domain changes or when the fluid-structure interfaces move (e.g. blood flow in the aorta, heart valve functions). Only a single media is modeled for either structural analysis or CFD without interaction between the media and its surroundings. However, FSI is the approach taking into account two or more media together with their mutual interactions simultaneously.

Arbitrary Lagrangian Eulerian method (ALE) is one of the most frequently implemented methods in FSI analysis. The various forms of ALE procedures include operator split, unsplit FE, finite difference advection method, interface tracking, momentum advection, coupled FE calculation, remapping and rezoning and mixture theory. These procedures are different in their governing equations describing the fluid domain motion and in their domain configuration strategies [131]. However, the fundamentals of the procedures are similar, which are the ALE coordinate reference systems to solve the large deformation problems. Three independent coordinate systems are introduced in an ALE formulation to identify the nodal locations in the continuum: the spatial reference (SR), the material reference (MR) and the computational reference (CR). The SR is a fixed system representing the Eulerian aspect of ALE formulation and the MR is deformable with the material based on Lagrangian formulation. The CR is a reference to the SR and MR moving arbitrarily in the continuum. The SR and MR describe the field quantities respectively in fluid and structural domain. However, these field configurations for an ALE formulation are computed in CR. Thus, the SR and MR need to be associated with each other, which can be performed by calculating the time derivative of the change in the sample state variable (physical quantity) $\Psi(\vec{x}, t)$ at point N (relative to the MR) in the MR and CR. The state variable is assumed to change in an infinitesimally small time step of $\Delta \mathrm{t}$.

In the MR, the time derivative of the state variable $\Psi(\vec{x}, t)$ can be described as:

$$\frac{D\Psi}{Dt} = \lim_{\Delta t \to 0} \frac{1}{\Delta t} [\Psi(\vec{x} + \mathrm{d}\vec{x}, \mathrm{t} + \Delta \mathrm{t}) - \Psi(\vec{x}, \mathrm{t})] \qquad (5.1)$$

$$\frac{D\Psi}{Dt} = \lim_{\Delta t \to 0} \frac{1}{\Delta t} [\Psi(\vec{x} + \mathrm{d}\vec{x}, \mathrm{t} + \Delta \mathrm{t}) - \Psi(\vec{x}, \mathrm{t}) - \Psi(\vec{x}, \mathrm{t} + \Delta \mathrm{t}) + \Psi(\vec{x}, \mathrm{t} + \Delta \mathrm{t})] \qquad (5.2)$$

If replacing “$\Psi(\vec{x} + \mathrm{d}\vec{x}, \mathrm{t} + \Delta \mathrm{t}) - \Psi(\vec{x}, \mathrm{t} + \Delta \mathrm{t})$” with “$d\vec{x} \cdot (\nabla\Psi)$”, the equation will be:

$$\frac{D\Psi}{Dt} = \lim_{\Delta t \to 0} \frac{1}{\Delta t} [d\vec{x} \cdot (\nabla\Psi) + \Psi(\vec{x}, \mathrm{t} + \Delta \mathrm{t}) - \Psi(\vec{x}, \mathrm{t})] \qquad (5.3)$$

$$\frac{D\Psi}{Dt} = \vec{\vartheta} \cdot (\nabla\Psi) + \frac{\partial\Psi}{\partial \mathrm{t}} |_{\vec{x}} \qquad (5.4)$$

$D\Psi Dt{=}\vartheta{\cdot}\nabla\Psi{+}\partial\Psi\partial \mathrm{t}/x$ (5.4), ϑ represents the velocity of point N relative to the MR. $D\Psi Dt{=}\vartheta{\cdot}\nabla\Psi{+}\partial\Psi\partial \mathrm{t}/x$ (5.4), the variation of the state variable of a specific point N is sum of the local variation and the convective term accounting for the relative displacement between the SR and MR. A similar equation for the state variable’s time derivative can be further derived relative to the CR:

$$\frac{D\Psi}{Dt} = (\vec{\vartheta} - \vec{\omega}) \cdot (\nabla\Psi) + \frac{\partial\Psi}{\partial \mathrm{t}} |_{\vec{u}} \qquad (5.5)$$

where u is the location of point N relative to the CR; ω is the relative velocity between the MR and CR.

Similarly, deriving from their Eulerian forms, the conservation equations for mass, momentum and energy can be described in ALE differential forms as follows:

$$\frac{D\rho}{Dt} = \rho\vec{\nabla} \cdot \vec{\vartheta} \qquad (5.6) \qquad \text{(Mass)}$$

$$\rho\frac{D\vartheta}{Dt} = \vec{\nabla}\cdot\sigma + \rho\vec{\mathrm{b}} \qquad (5.7) \qquad \text{(Momentum)}$$

$$\rho\frac{D\mathrm{E}}{Dt} = \vec{\nabla}\cdot(\sigma\cdot\vec{\vartheta}) + \vec{\vartheta}\cdot\rho\vec{\mathrm{b}} \qquad (5.8) \qquad \text{(Total energy)}$$

$$\rho\frac{D\mathrm{e}}{Dt} = \sigma{:}\frac{1}{2}(\nabla\vartheta + \nabla^{T}\vartheta) \qquad (5.9) \qquad \text{(Internal energy)}$$

where ρ is the material density, σ is the Cauchy stress tensor, b is the body force, E is total energy and e is the internal energy. To be noted, the $\sigma{:}\frac{1}{2}(\nabla\vartheta + \nabla^{\mathrm{T}}\vartheta)$ is the Frobenius inner product of the Cauchy stress and the strain rate tensor.

The conservation equations in an ALE form can be obtained by substituting the equation $\frac{D\Psi}{Dt} = (\vec{\vartheta} - \vec{\omega})\cdot(\nabla\Psi) + \frac{\partial\Psi}{\partial \mathrm{t}}|_{\vec{u}}$ (5.5) into the equations above:

$$\frac{\partial\rho}{\partial t} + (v-\omega)\cdot\nabla\rho = \rho\vec{\nabla}\cdot\vec{\vartheta} \qquad (5.10) \qquad \text{(Mass)}$$

$$\rho\frac{\partial\vartheta}{\partial t} + \rho(v-\omega)\cdot\nabla\vartheta = \vec{\nabla}\cdot\sigma + \rho\vec{\mathrm{b}} \qquad (5.11) \qquad \text{(Momentum)}$$

$$\rho\frac{\partial\mathrm{E}}{\partial t} + (v-\omega)\cdot\nabla E = \vec{\nabla}\cdot(\sigma\cdot\vec{\vartheta}) + \vec{\vartheta}\cdot\rho\vec{\mathrm{b}} \qquad (5.12) \qquad \text{(Total energy)}$$

$$\rho\frac{\partial\mathrm{e}}{\partial t} + (v-\omega)\cdot\nabla e = \sigma{:}\frac{1}{2}(\nabla\vartheta + \nabla^{T}\vartheta) \qquad (5.13) \qquad \text{(Internal energy)}$$

These equations are derived by replacing the material velocity v with the convective velocity $(v-\omega)$. For incompressible material, the density ρ of which is considered to be constant, equation $\frac{\partial\rho}{\partial t} + (v-\omega)\cdot\nabla\rho = \rho\vec{\nabla}\cdot\vec{\vartheta}$ (5.10) (Mass) will become:

$$\nabla\cdot\vartheta = 0 \qquad (5.14)$$

If substituting the constitutive equation

$$\sigma = -p\,I + 2\eta\,D \qquad (5.15)$$

into the Cauchy stress tensor of the momentum equation $\rho\frac{\partial\vartheta}{\partial t} + \rho(v-\omega)\cdot\nabla\vartheta = \vec{\nabla}\cdot\sigma + \rho\vec{\mathrm{b}}$ (5.11) (Momentum), THE Navier-Stokes formulation of ALE approach will be:

$$\rho\frac{\partial\vartheta}{\partial t} + \rho(v-\omega)\cdot\nabla\vartheta = -\vec{\nabla}p + \vec{\nabla}\cdot 2\eta\,D + \rho\vec{\mathrm{b}} \qquad (5.16)$$

According to equation $\rho\frac{\partial\vartheta}{\partial t} + \rho(v - \omega)\cdot\nabla\vartheta = -\vec{\nabla}\, p + \vec{\nabla}\cdot 2\eta\, D + \rho\vec{\mathrm{b}}$ (5.16), if assuming ω to be zero, the Navier-Stokes equations will be equivalent for Eulerian and ALE formulations, except for the fact that $\frac{\partial\vartheta}{\partial t}$ is defined relative to the CR.

During the modeling and calculation processes, the FE meshes defined as Eulerian formulation is fixed in the SR. As the Lagrangian motion and the material deformation transport through the Eulerian mesh, the Eulerian formulation can trace for element deformations. In order to achieve this, the Eulerian codes implement an approach of separating these terms in two phases (displayed in Figure 5.6): the FE meshes distort with the material in a Lagrangian step and the distorted meshes are mapped onto the CR moving arbitrary in space and not depending on the MR or SR. The second step is often referred to as the “advection”, “remap” or “Eulerian” step.

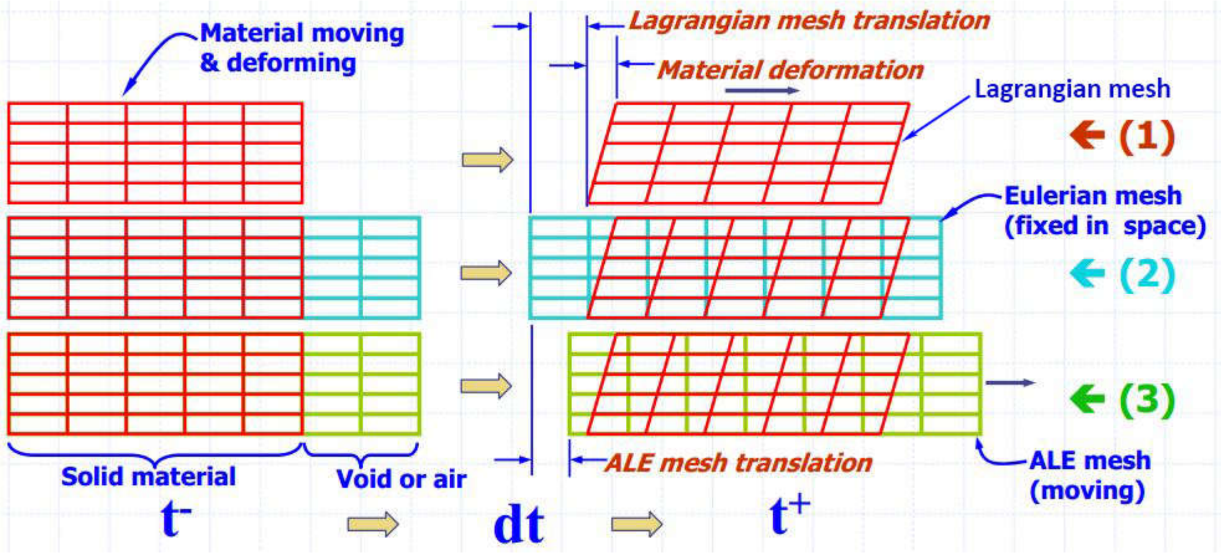
Material moving
& deforming
Lagrangian mesh translation
Material deformation
Lagrangian mesh
(1)
Eulerian mesh
(fixed in space)
(2)
(3)
ALE mesh translation
ALE mesh
(moving)
Solid material
Void or air
t-
dt
t+

Figure 5.6. Schematic drawing to show the deformation and translation of meshes in different formulations: (A) Lagrangian, (B) Eulerian and (C) ALE

Regarding the ALE formulation, the background mesh can move arbitrarily in the SR and the distorted meshes in the Lagrangian step are remapped onto the new ALE meshes as follows:

- more relaxed meshes are created with a mesh smoothing algorithm;
- the element-centered variables are mapped and transported;

- the node-centered momentums are mapped and transported.

Compared with the Lagrangian formulation in which the elements always contain a single material, the ALE and Eulerian formulations can contain more than one material in a single element. These ALE and Eulerian elements are referred to as “multi-material” elements and are more computationally expensive due to their complexities.

5.2 Article #4: Fluid-Structure Interaction Simulation of Aortic Blood Flow by Ventricular Beating: a Preliminary Model for Blunt Aortic Injuries in Vehicle Crashes

This article “Fluid-Structure Interaction Simulation of Aortic Blood Flow by Ventricular Beating: a Preliminary Model for Blunt Aortic Injuries in Vehicle Crashes” was published in the International Journal of Crashworthiness on 17th June, 2018.

Wei Wei[1,*], Cyril J.F. Kahn[1], Michel Behr[1]

[1] *Aix-Marseille Université, IFSTTAR, LBA UMR T24, 13916 Marseille, France*

Abstract

Blunt aortic injuries are common and severe in motor vehicle crash accidents (MVCAs), but the injury mechanisms, which can be categorized as kinematics and hydrodynamics aspects, remain to be uncertain. In this study, a finite element model was developed for the aorta-heart system with fluid-structure interaction methods, aimed to study both kinds of mechanisms simultaneously. The aortic blood flow was generated by simulating left ventricle contraction. This model was further integrated with a human body model to reconstruct a real car crash case. The aorta-heart model was validated against ventricular volume, blood pressure, velocity, flow rate and wall shear stress. The integrated model predicted aorta isthmus laceration and other injuries consistent with the case injury reports. The cardiac output during the accident was more intense than the physiological output, proving the ability of current simulation approach to capture the blood flow modification by the thoracic compressive loadings during accidents.

Keywords: Aortic Injury, Left Ventricle Contraction, Fluid-Structure Interaction, Fluid Dynamics, Motor Vehicle Crash Accidents

5.2.1 Introduction

The aorta is a vulnerable organ in motor vehicle crash accidents (MVCAs), in which blunt aortic rupture (BAR) is reported as the second most common cause of death [4]. In MVCAs, the BAR is acute with 85% of the victims deceased at the scene and about 30% of whom can stick to the hospital dying within a single day if untreated [5]. BAR mechanisms were widely investigated and various possible scenarios were proposed according to the situations: sudden stretching of the aorta with rupture at isthmus [6], entrapment of the aorta by the surrounding bony structures [7], sudden stroke of blood pressure related to water hammer effect [8], or even a combination of these different mechanisms [5].

To some extent, these mechanisms could therefore result from two different sources of contribution: the inertia of the aorta itself and its surrounding organs, hereafter referred to as kinematics, and the hydrodynamics of blood, hereafter referred to as hydrodynamics. Kinematics and structural responses of aorta in MVCAs were studied in previous researches without considering possible blood flow effects on BAR [17, 21, 55]. The blood hydrodynamics were also investigated in MVCAs, without including the interaction between aorta and other organs [22, 132]. In these last studies, blood flow was also limited to the definition of inlet and outlet pressure profiles, without considering cardiac output possibly modified by additional dynamic compression of the ventricles. In MVCAs, high levels of thoracic compression were however reported [133] and resultant significant blood pressure profile modifications should be expected.

In other words, previous studies dealing with BAR mechanisms investigation were subjected to two main limitations: simulating the concomitant effects of kinematics and hydrodynamics was not considered, nor the possible effect of chest compression on blood flow modification. Therefore, this paper deals with the development of an aorta-heart system finite element (FE) model based on fluid-structure interaction (FSI) methods with LS-DYNA that is able to consider altogether tissue kinematics, heart beats and blood hydrodynamics to investigate BAR mechanisms.

5.2.2 Material and methods

Isolated heart-aorta model was developed with FSI approach and validated against the aortic blood flow. The model was then integrated with a whole human body model which was subsequently used to reconstruct a BAR-related MVCA.

Isolated heart-aorta model

Geometry and meshes

The geometric model of the aorta and heart was acquired from an internet database [134]. An anatomist examined the geometry to ensure its normal anatomy and morphology. The geometry was scaled to make the aortic diameters of different sections (Table 5.1; Figure 5.7B) consistent with literature data [135, 136] and the before-systole left ventricle (LV) volume (123.2ml in this work) within the reported range [137].

Table 5.1. Aortic diameters at different sections comparing with the data in literature [135, 136].

Section	1	2	3	4	5	6	7	8
Diameter (mm)	27.4	27.8	27.1	24.8	24.0	21.9	20.8	18.1
Diameter range (mm)	26.8-28.7 [136]	27.2-29.1 [136]		24.4-26.4 [135]		20.3-22.1 [136]		19.3-20.8 [136]

The aorta and other vessels were meshed with 12,296 4-node shell elements. The heart was meshed with 85,035 tetrahedral elements since its complex geometry made it impossible to mesh with high-quality hexahedral elements. The heart was modeled only to pump the blood flow to the aorta and the heart's stress level was not current focus. An Eulerian grid with Arbitrary Lagrangian-Eulerian (ALE) formulation was constructed to model the fluid domain (Figure 5.7). The fluid region was meshed with 106,739 8-node hexahedral elements since the simulation solver (LS-DYNA) requires high-quality hexahedral elements for the initial ALE mesh. The amount of meshes was decided after a mesh-convergence analysis was conducted, based on section-averaged blood velocity with a 1% threshold.

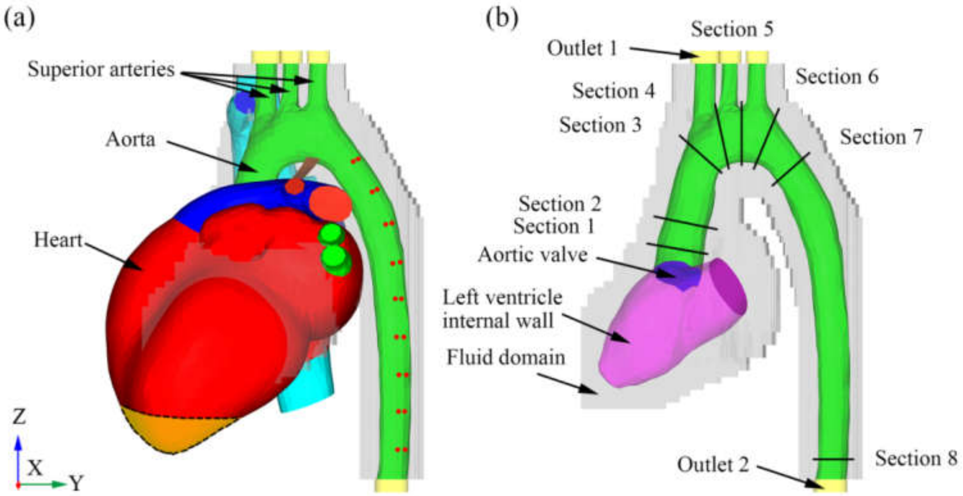
(a)
Superior arteries
Aorta
Heart
Z
X
Y
(b)
Section 5
Outlet 1
Section 6
Section 4
Section 3
Section 7
Section 2
Section 1
Aortic valve
Left ventricle internal wall
Fluid domain
Outlet 2
Section 8

Figure 5.7. FE model of heart-aorta system. (A) FE model displaying the location of boundary constraints on the descending aorta (red points) and on the heart (orange area in dash lines), (B) FE model showing structural components, fluid domain and the locations of each aortic section

Material properties and coupling interfaces

The aorta was assumed to be transversely isotropic and incompressible hyperelastic material [87], the parameters of which came from previously published data [88]. The other vessels and the heart were assigned with an elastic material law as detailed in [55, 70]. Multi-material ALE formulation was used for its improved accuracy under large deformation problems [131]. With multi-material ALE, it was possible to fill the initial LV volume with blood and to define the fluid space outside LV as void. Otherwise, it was impossible to divide the fluid domain into two separate parts (outside and inside LV) and to mesh them with hexahedral elements. For simplification, the blood inside LV and aorta was modeled as Newtonian fluid with a density of 1050kg/m^3, a dynamic viscosity set to 4500Pa•s and a bulk modulus of 2.5GPa as previously proposed in [24].

Three coupling interfaces were constructed between the fluid and the structure components: aorta, LV and a simplified aortic valve. The aortic valve (Figure 5.7B) was simplified as a layer of rigid shell elements, only to realize its physical function of preventing blood backflow during diastole. The function of the valve was achieved by activating the coupling interface during diastole and deactivating during systole. Since the mitral valve was not modeled, the coupling interface between LV and blood was dismissed during late diastole to allow the blood to replenish the LV. In this way, the LV volume will be recovered for next cycle. The interaction between solid and fluid domain was modeled by activating the penalty coupling algorithm parameter in LS-DYNA FSI keyword, in which elastic forces were computed against the structure-fluid penetration and imposed on coupling points of structural elements. In order to reduce the fluid leakage below 1% of the blood volume, 4 coupling points were distributed on each structural element (ventricle and aorta).

Boundary conditions

The lower region of the heart (see Figure 5.7A) was constrained to simulate the attachment between pericardium and diaphragm [138]. The posterior part of descending aorta (Figure 5.7A) was constrained to simulate the attachment of 9 pairs of intercostal arteries with thoracic spine [138]. The distal end of the descending aorta was also constrained to simulate the tight attachment of the diaphragm at the diaphragmatic aortic hiatus [138].

A physiological time-independent pressure previously detailed in [89] was correspondingly applied to outlet 1 and 2 (cf. Figure 5.7) by prescribing their thermodynamic states with the relative volume curves and the linear equations of state (APPENDIX H). The blood flow was obtained by simulating the contraction and relaxation of the LV. To do so, a time-dependent loading was applied on the LV internal wall, oriented to LV centre and normal to the meshes. The loading was iteratively adjusted to make the LV volume time-history consistent with those previously proposed in literature [139-141].

The model was mainly validated against published literature data in terms of blood flow velocity, flow rate and wall shear stress (WSS) at different aortic sections.

MVCA reconstruction with integrated human model

Integrated human model

The validated heart-aorta model was integrated with the Global Human Body Models Consortium (GHMBC) M50 model (V4.4; Elemance, Winston-Salem, USA). The GHBMC model has been widely validated against various impact scenarios and for different body parts [142]. The heart and aorta of GHBMC were simplified while blood flow could not be simulated. The original GHBMC heart-aorta was replaced with current heart-aorta model (displayed in Figure 5.8A). Superior arteries of the aorta were elongated to attach to the clavicles by sharing common nodes. The descending aorta was connected to the GHBMC abdominal descending aorta by sharing common nodes. Surface-to-surface contacts were defined between the heart-aorta and the surrounding GHBMC components (i.e. lung, diaphragm and spine). Tied contact was defined between the pulmonary arteries and the lung root to attach both components. Tied contacts were defined between the descending aorta and spine to model the subcostal artery and 8 intercostal arteries (corresponding to the boundary constraints in Figure 5.7A).

MVCA reconstruction

A vehicle side-impact case involving BAR was obtained from [20]. It was selected to reconstruct the accident since the case vehicle and victim were close to the available vehicle and human FE models in sizes (detailed in APPENDIX I). The case vehicle (1994 Honda Accord) impacted a rigid pole on its left front door with an estimated speed of 27.6km/h with 320-degree principal direction of force (Figure 5.8B). The driver (65-year old male, 181cm and 101kg) was constrained with a 3-point seatbelt but no side airbag was available during the accident. He died with aortic isthmus laceration and other injuries (detailed in APPENDIX I).

The case reconstruction was performed in two stages (Figure 5.8): vehicle-pole crash simulation; occupant simulation interacting with the restraint system and vehicle components. For stage 1, the FE model of 2012-year Toyota Camry, released and validated by the National Highway Traffic Safety Administration, was prescribed with an initial velocity of 27.6km/h to impact the rigid pole (diameter 46cm). Since the initial vehicle-pole relative position was not reported, the FE simulation was iteratively repeated, tuning the X-distance between the pole and B-pillar until a reasonable match was obtained for the case vehicle deformations measured according to the deformation classification (11LPAW3) [120]. The driver side structures, including the seat, doorframe, door armrest and left B-pillar, were grouped and their motions were recorded in separate binary interface files. These files were input as the loading conditions for stage 2 simulation.

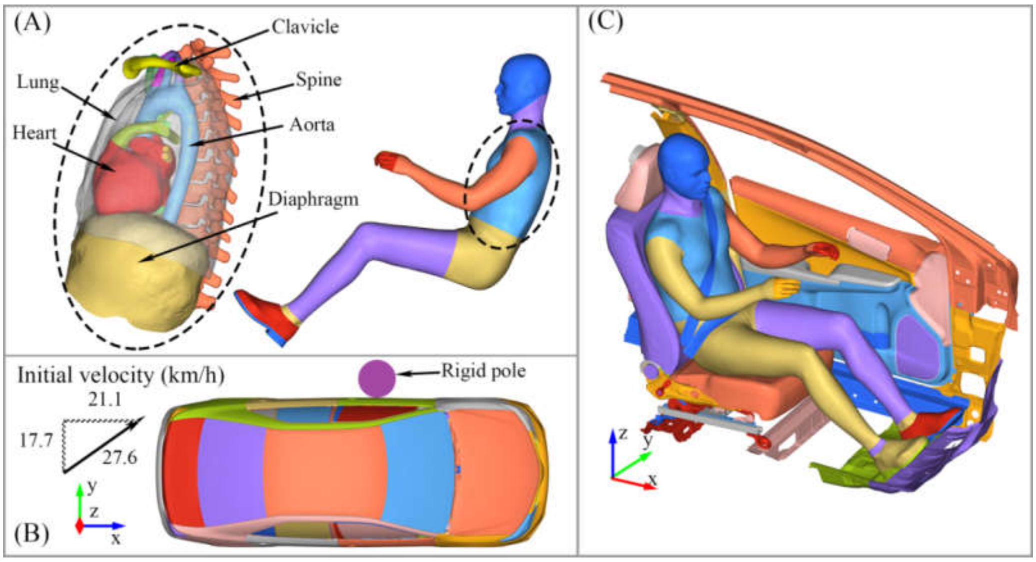

Figure 5.8. BAR-related MVCA reconstruction with the heart-aorta integrated human FE model. (A) the whole human FE model integrated with the heart-aorta FSI model, (B) stage 1 of MVCA reconstruction with car-pole side impact, (C) stage 2 of MVCA reconstruction with occupant-vehicle interaction

For stage 2, the driver side components grouped in stage 1 were extracted from the car model. The integrated human model was used to simulate the victim and firstly dropped onto the deformable seat under gravity loading. This simulation terminated until equilibrium in contacts between the occupant and vehicle components (seat and floor) was reached. A seatbelt with 6kN-load-limit retractor was then created and fit to the occupant's chest and abdomen as previously described in [121]. The interface files from stage 1 were imported to prescribe the motions of the driver side structures. Meanwhile, the initial stresses due to occupant-seat/floor contact were also inherited from the previous occupant drop simulation.

The occupant impact simulation was evaluated against the case injury descriptions in terms of stress and strain for the thoracic organs (e.g. aorta, lungs and ribs). The cardiac outputs during the accident were compared with those under the physiological condition in terms of LV volume, , blood pressure and velocity.

All the simulation pre-processing (e.g. heart-aorta modelling, human model integration and MVCA reconstruction) was performed with Hypermesh 12.0 (Altair Engineering Inc, MI, USA).

All the simulations (FSI and MVCA) were calculated with LS-DYNA 971 R7.1.1 (LSTC, Livermore, CA, USA) on an Intel Xeon (2.57 GHz) workstation with 40 processors.

5.2.3 Results

Isolated heart-aorta model validation

LV volume and blood pressure

The calibrated LV volume was displayed in Figure 5.9A with literature recordings. The ventricular pressure was shown in Figure 5.9B and compared with two smoothened curves in literature [23, 143]. The blood pressures in ascending (section 1) and descending aorta (section 8) were displayed in APPENDIX J with literature data.

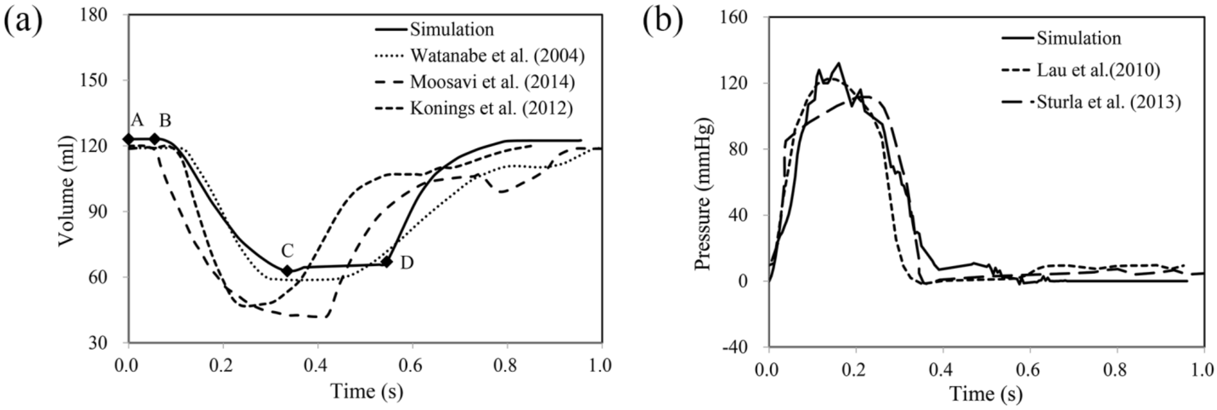

Figure 5.9. The time-history of LV volume (A) and blood pressure (B). The landmarks on LV volume change curve correspond to different cardiac moments when the LV began to contract (A), the LV began to eject (B), the LV stopped ejecting (C) as well as the LV began to recover its volume (D)

Blood flow and WSS at different aortic sections

The peak velocity of blood flow through aortic root was shown in Figure 5.10A, which was measured at the central node of section 1 as previously performed in [24]. The peak recorded value in the simulation curve was 1.86m/s, occurring 90ms after the beginning of ejection. The section-averaged blood velocity was displayed in Figure 5.10C for section 1 and in APPENDIX

K for other sections, which was computed by averaging the nodal velocity (Figure 5.10B) at each moment. The peak value of mean blood flow at section 1was 0.76m/s and 0.42-0.79m/s at other sections. Flow rates were displayed in Figure 5.10E for section 1 and in APPENDIX L for other sections which were computed by multiplying the section-averaged velocity and the real-time section area.

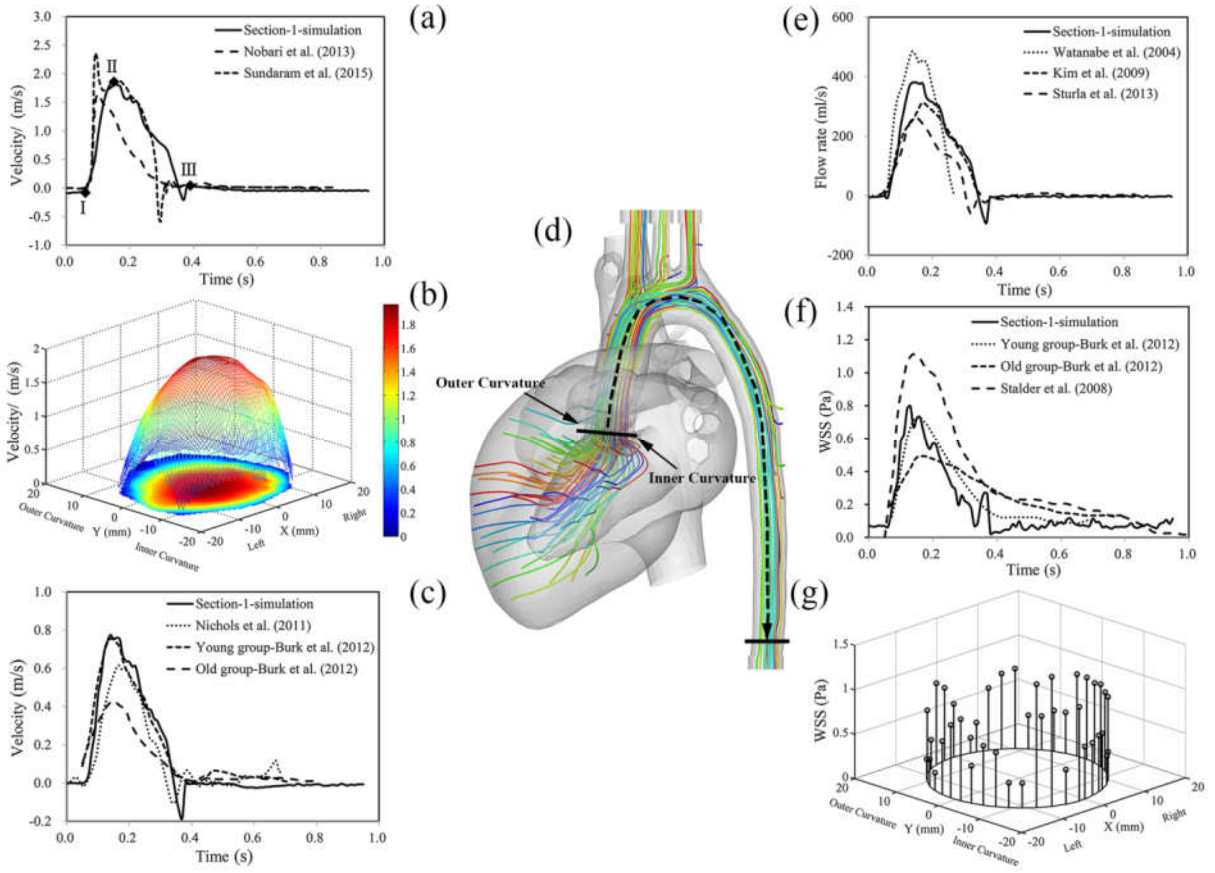

Figure 5.10. Blood flow and WSS at aortic section 1. (A) Peak blood velocity of section 1 during the cycle where landmark I, II and III represent respectively the beginning of LV ejection, the peak ejection and the beginning of diastole. (B) The blood flow profile fitted with cubic spline at the moment corresponding to landmark II. (C) Section-averaged blood velocity. (D) Blood flow stream line in the LV and aorta at the moment of landmark II. The dash line arrow represents the blood flow direction and the aortic midline from section 1 to 8 for measuring pulse wave velocity. (E) Blood flow rate. (F) Section-averaged WSS. (G) WSS distribution at the moment of landmark II.

Section-averaged WSS was displayed in Figure 5.10G for aortic root and in APPENDIX M for other sections, the computing procedure of which was detailed in APPENDIX M. The peak value of section-averaged WSS was 0.80Pa at section 1 and 0.47-0.89Pa for other sections.

MVCA reconstruction

The vehicle-pole impact duration was 120ms. The reconstructed lateral intrusions were listed in Table 5.2 and the deformation patterns including the locations of intrusion measurement were displayed in APPENDIX N. In stage 2, the occupant was subjected to the peak chest deformation at t=90ms when the corresponding deformations of rib cortical bones, diaphragm and aorta were displayed in Figure 5.11. Fractures occurred at the cortical bones of left rib 7-11 and right rib 6-11. The diaphragm had a peak VonMises stress of 2.7MPa with a corresponding strain of 78.5% at its attachments with the right costal cartilage and aortic hiatus. The aortic isthmus had a peak VonMises stress of 1.8MPa with a corresponding strain of 40.9%. The cardiac output recorded with the integrated FSI human model during the MVCA was displayed in Figure 5.12.

Table 5.2. Intrusions of vehicle-pole impact reconstruction compared with case vehicle crush profiles

Deformation (cm)	C1	C2	C3	C4	C5	C6	AD (%)
Case	0	23	38	31	15	2	--
Simulation	0	24	37	30	18	1	--
Difference (%)	0.0	4.3	-2.6	-3.2	20.0	-50.0	-5.3

*AD: Average difference

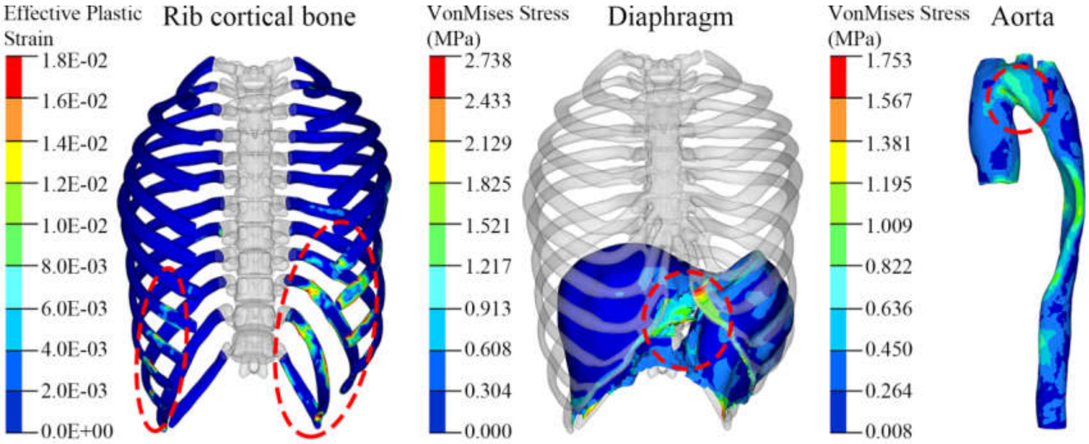
Effective Plastic Strain
Rib cortical bone
1.8E-02
1.6E-02
1.4E-02
1.2E-02
1.0E-02
8.0E-03
6.0E-03
4.0E-03
2.0E-03
0.0E+00
VonMises Stress (MPa)
Diaphragm
2.738
2.433
2.129
1.825
1.521
1.217
0.913
0.608
0.304
0.000
VonMises Stress (MPa)
Aorta
1.753
1.567
1.381
1.195
1.009
0.822
0.636
0.450
0.264
0.008

Figure 5.11. Simulation results of occupant injuries: contour plots of effective plastic strains for rib cortical bones, VonMises stress for diaphragm and aorta at t=90ms in stage 2

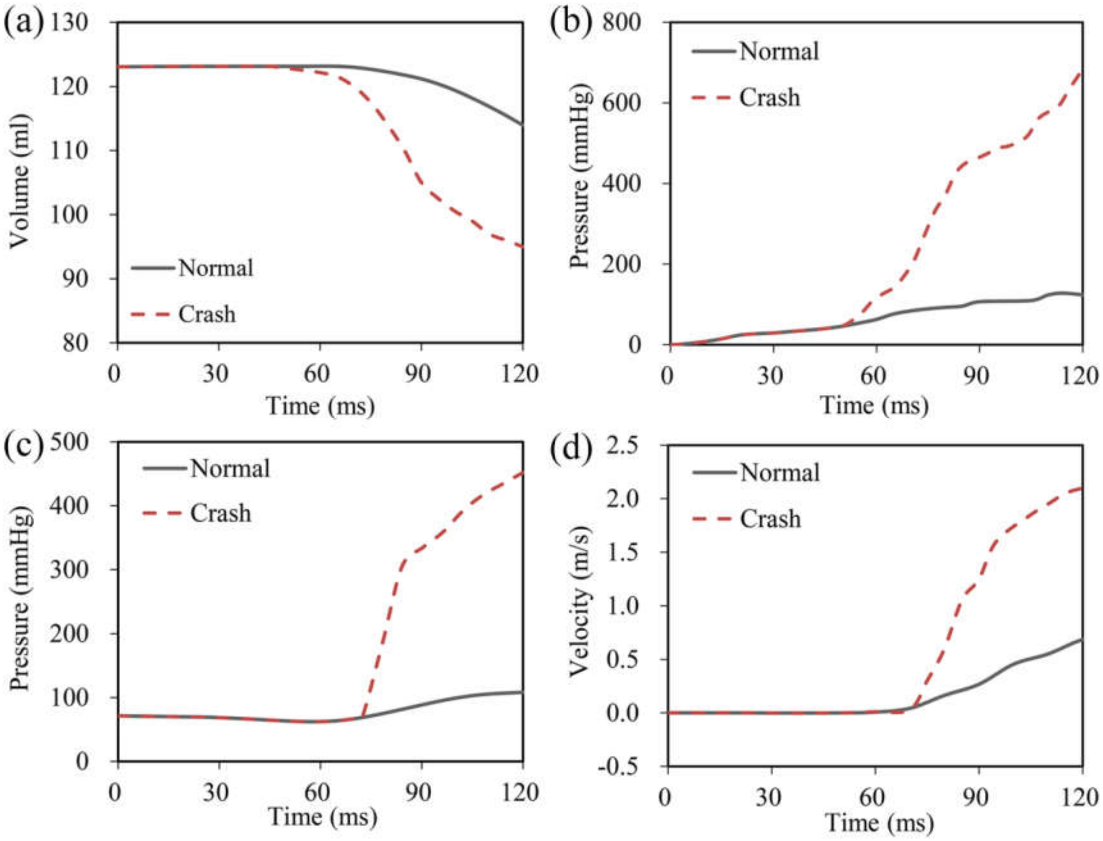

Figure 5.12. The cardiac output during the reconstructed MVCA compared with the normal cardiac output from isolated heart-aorta model: LV volume (A), LV blood pressure (B), blood pressure (C) and section-averaged velocity (D) recorded at section 1

5.2.4 Discussion

Isolated heart-aorta model validation

Realistic hydrodynamic descriptions in MVCAs require corresponding validations against blood dynamics. Since there was no available data on blood flow in MVCA situations, we had to compromise the validation against physiological hydrodynamics. Simulated LV volume, blood pressure and flow were compared with previous medical and simulation researches.

Simulated LV volume (Figure 5.9A) at the beginning and the end of systole was 123ml and 63ml respectively, i.e. in very good agreement with previously reported curves [139-141], despite minor amplitude discrepancies. The LV volume related ejection fraction and the before and after-systole LV volume did also agree with the ranges reported by Schlosser et al. [144]. The blood pressures in LV (Figure 5.9B) and in aorta (APPENDIX J) consisted with the published data [23, 89, 143, 145, 146] not only in shapes but also in magnitudes especially during systole phase. During diastole, the aortic blood pressure was found consistent with values reported in [89] and slightly lower than those reported in [146]. This could be ascribed to the relative lower outflow pressure (APPENDIX H) applied in this study. Even so, the validity of the model should not be affected when studying hydrodynamic effects on BAR, since blood flow during diastole can be neglected. The general good consistency of the LV volume and blood pressure confirmed the ability of the LV to pump appropriate volume of blood into the aorta during the realistic systole.

The blood flow validation in this study did not account for particle flow but was rather focused on section-averaged velocity, flow rate and WSS, i.e. general hydrodynamics information. This choice was made since model would be dedicated to MVCA scenario investigations rather than clinical research. In MVCAs involving BARs, the injuries usually happen within 100ms after collisions [19]. The possible hydrodynamic mechanisms should therefore be related to transient factors, e.g. the sudden pressure elevation resulting from general flow occlusion, than long term factors such as aortic tissue remodelling due to local particle flow modification. Moreover, simulating detailed blood flow like turbulence and vorticity requires finer fluid meshes, which are quite time-consuming and therefore not well adapted to a further integration into a full human FE model. The blood flow generated by LV beats was consistent with previously published data for different aortic sections in terms of blood velocity, flow rate and WSS [23, 24, 89, 141, 145-148].

The simulation curves agreed well with the previously published curves not only in their magnitudes but also in the duration of systole and diastole. To be noted, the aortic sections for validation against blood velocity, flow rate and WSS were not randomly chosen, but based on the available data in literature.

MVCA reconstruction

In stage 1, the reconstructed lateral intrusions agreed well with the case recordings with a maximal deformation difference of 3cm at C5 and an average difference of 5.3% among C1-C6 (Table 2). In stage 2, the simulated bilateral rib fractures were consistent with the injury descriptions. Previous human diaphragm stretch tests suggested the diaphragm failure stress ranged from 1.17MPa to 4.1MPa and failure strain ranged from 12.15% to 24.62% [149]. The simulated peak stress of 2.7MPa and peak strain of 79.1% at the diaphragm indicated its high risk of injury. Similarly, the peak stress of 1.8MPa and the peak strain of 40.9% at the aortic isthmus indicated its high risk of failure, since the aortic failure stress was reported to range from 1.67MPa to 2.32MPa with the failure strain range 21.7-27.7% [55]. The predicted injuries of diaphragm and aorta in stage 2 were consistent with the case recordings of diaphragm and aortic isthmus lacerations.

The cardiac output during the MVCA was compared with the normal output from the isolated heart-aorta FSI model (Figure 5.12). The LV stroke volume during the vehicle-pole duration (0-120ms) was 19.0ml more than the physiological value. The peak blood pressures recorded at LV and aortic section 1 during impact were 552mmHg and 342mmHg higher than the corresponding values in normal cardiac cycle. The peak blood velocity at aortic section 1 was 1.4m/s higher than the peak velocity in normal cycle. The more intense cardiac output during MVCA proved our previous assumption that the occupant thoracic compression could significantly modify the blood flow conditions in the aorta. In fact, the occupant suffered from a high level of chest compression due to his impact with the vehicle door structures. The chest compression imposed a compressive loading to the heart, resulting in a higher LV contraction force and stroke volume. To be noted, it was the current blood simulation approach by heartbeat that made it possible to capture the modification of cardiac output during MVCAs. The traditional simulation approaches tended to prescribe specific profiles of pressure at the aortic inflow and outflow. In this way, the aortic blood flow could not be regulated automatically with the varying external loadings (e.g. thoracic compression) during MVCAs.

5.2.5 Limitations

Although aortic blood flow was reproduced by heart-beating and the blood flow modification was captured during MVCA, some limitations existed in current study. The occupant simulation with the integrated human model in stage 2 was extremely long, up to 45 days on a workstation with 40 processors for 120ms crash duration. The FSI coupling algorithm highly increased the calculation time while the huge size of the integrated model made the simulation even longer. One possible solution is to make another sub-simulation with the thoracic components of the integrated human model. In stage 2, the original GHBMC model instead of the integrated model would be used for the occupant impact simulation. The thoracic components (e.g. lung, spine and diaphragm) were grouped to record their motions in the binary interface files as was done in stage 1. These motions were further imported in the sub-simulation to reproduce the interaction between the heart-aorta and the surrounding organs.

The relative period of the impact duration (0-120ms) against the cardiac cycle (0-1000ms) was another limitation. In our reconstructed MVCA, the vehicle-pole collision happened at the beginning of the cardiac cycle. However, the accident could happen at any moment of the cardiac cycle. Due to the tedious occupant simulation (the first limitation), a single scenario of collision-cardiac relative moment, which resulted in the shortest simulation (120ms), was considered in current study. More relative collision-cardiac moments remained to be simulated to investigate the sensitivity of thoracic compression effects on blood flow modifications.

Another limitation was the simulation approach of the simplified aortic valve. The valve function was modeled by activating and deactivating the valve-blood coupling interface at specific moments of the cardiac cycle. With the available LS-DYNA FSI keywords, it was impossible to detect the moment automatically according to the LV-aorta pressure gradient when the coupling interface should be active. A second-development of the FSI keywords (e.g. activating the coupling keyword with the pressure sensors located in the LV and aorta) would be necessary to achieve this function. The aortic stress/strain levels during MVCAs remained to be validated while more MVCAs should be reconstructed to investigate the collision-related blood flow modifications for future BAR researches. These were other limitations of current study.

5.2.6 Conclusions

In this paper, a FE model was developed for the aorta-heart system with FSI method, and was able to simulate realistic blood flow resulting from the heartbeat only, instead of the traditional inlet-outlet prescribed pressure approaches. This model was integrated with a human body model to reconstruct a BAR-related MVCA. The integrated model predicted aortic laceration and other injuries consistent with the case injury descriptions. The assumption that the aortic blood flow could be modified by the high level of thoracic compression during MVCAs was proved by the more intense cardiac output recorded in the MVCA reconstruction. The human model integrated with the FSI heart-aorta was able to consider both kinematic and hydrodynamic effects to study BAR mechanisms in MVCAs. Although certain limitations existed in current study, this work was, as far as the authors knew, the first attempt to consider the hydrodynamic effects on BAR by generating blood flow with heartbeat instead of theoretical inlet and outlet specifications. It was the heartbeat simulation that made it possible to capture the cardiac output modification during MVCAs.

5.2.7 Conflict of interest

None

CHAPTER 6 AORTIC STRESS LEVEL AND BAR MECHANISM IN MVCA

In Chapter 3, we concluded that the cardiac loadings should be considered for MVCA-related BAR studies by comparing the aortic responses under cardiac function with those experienced in MVCAs. In Chapter 4, we observed the significant effects of intra-aortic pressure on aortic deflections during the mini-sled tests and estimated a high pressure-related risk of BAR in the reconstructed MVCA case. Thus, we concluded that it was necessary to consider the intra-aortic pressure to better predict BAR in MVCAs. In Chapter 5, we succeeded in reproducing aortic blood flow with heartbeat during a cardiac cycle and MVCA.

However, the aortic responses during MVCAs, which were compared with the aortic responses under cardiac cycle in Chapter 3, came from literature with aortic FE models of different materials. Different aortic materials might result significantly different aortic responses. The observation of intra-aortic pressure effects on aortic mobility was based on in-vitro experiments with unrealistic aortic boundary conditions in Chapter 4. The pressure-related BAR risk was estimated according to the blood pressure from a human FE model which simplified blood modeling without simulating blood flow. Aortic mobility remains to be quantified with realistic boundary conditions under the loadings relevant with MVCA. The blood pressure during MVCA remains to be quantified with a model which can reproduce realistic aortic blood flow.

Therefore, this chapter aims to reproduce aortic responses under the loadings of MVCA including intra-aortic interactions and different intra-aortic pressure conditions, so as to provide such information as aortic stress, strain, mobility and luminal pressure under the corresponding loading conditions. These results altogether serve to investigate the BAR mechanisms in MVCA.

6.1 Aortic stress level under the loadings of blood pressure and intra-thoracic interactions in MVCAs

6.1.1 Introduction

One possible approach of including the aortic blood flow in MVCAs could be simulating the accidents directly with some whole human FE models able to generate blood flow. Various whole human FE models were previously developed for vehicle occupant injury prevention. Besides the WSHBM model developed by Shah et al [71] and mentioned in Chapter 2, other models include the H-model [150], the Ford human body model [151], the HUMOS2 model [152], the THUMS model [153] and the GHBMC model [154]. However, none of these models has the ability of reproducing blood flow since their aortic lumen was either filled with solid material or modeled with airbag. Therefore, some new human model with this ability needs to be developed to fulfill the purpose of including aortic blood flow in MVCAs. Based on the FSI heart-aorta model introduced in Chapter 5.2, a promising and easier way might be to integrate this model with some available whole human FE model. Considering our access to the models and the compatibility with the heart-aorta FSI model (LS-DYNA code), GHMBC-M50 model was chosen for the model integration and crash simulation works.

Before introducing the model integration and crash simulation, it is necessary to briefly review the model development, validation and application studies about GHBMC-M50. The geometry of the model was based on the computer design data which were developed from the clinical scanning images of a living male volunteer (26 years, 174.9cm height and 78.6kg weight). The regional models (i.e. head, neck, thorax, abdomen, pelvis and lower extremity) were independently developed with their focuses on meshing and model validation (see Figure 6.1). They were then integrated into a full body model, in which the mesh connections between neighboring body regions were performed according to the geometry, element type and anatomic purpose. The model contains a total of 1.3 million nodes, 1.95million elements and 961 parts, representing a mass of 75.5kg [155] (see Figure 6.1).

The regional model validation was performed for the head [156], neck [157-159], thorax [160, 161], abdomen [162], and pelvis and lower extremities [163, 164]. The full body model was also validated against frontal and side impact scenarios [133, 142, 165]. However, the aorta-related modeling was simplified to extent. For example, the blood inside the heart and aortic volume was defined as elastic fluid material. In this case, the aortic blood actually behaves as the structural solid material and can not flow from the LV to the aorta. Moreover, the interaction between the aorta and the spinal column was simulated as "automatic-surface-to-surface" contact, allowing sliding phenomenon and relative movement in the normal direction. From the anatomic perspective, the thoracic DA is, nevertheless, tightly attached to the spine by the subcostal artery and 8 pairs of intercostal arteries [138]. Therefore, in order to investigate the aortic stress levels and BAR mechanisms under the loadings of the intra-aortic pressure and intra-thoracic interactions, the heart-aorta FSI model should be integrated with the GHBMC model while the realistic constraint between the aorta and the spine should be added.

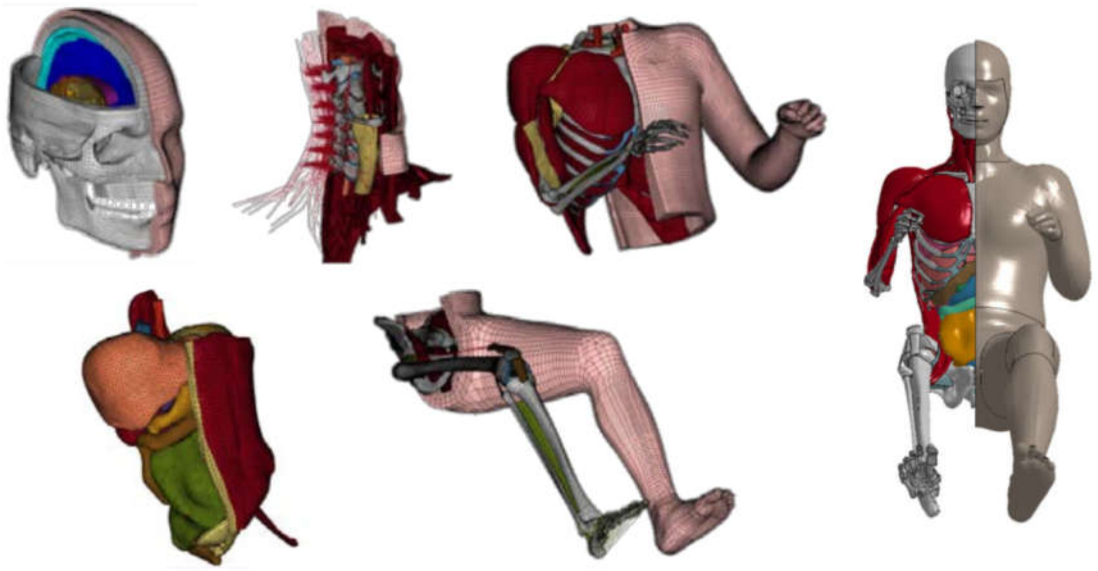

Figure 6.1 GHBMC-M50 body region and full body models (adapted from [155] and [142])

6.1.2 Material and methods

Model integration

The GHMBC-M50 model (V4.4; Elemance, Winston-Salem, USA) (see Figure 6.2A and B) was used in current study to integrate with the heart-aorta FSI model (displayed in Figure 6.2C), which was validated in Chapter 5.2 against a physiological cardiac cycle. The original GHBMC components of heart, aorta and blood were removed. The heart-aorta FSI model was firstly placed at a similar location as the original components in the thoracic cavity. Due to different shapes and sizes between FSI and original components, some penetrations existed between the FSI model and the GHBMC intra-thoracic components (e.g. the lungs, diaphragm and thoracic spine). The FSI components were moved and rotated to eliminate the penetrations while the heart and aorta were always ensured to be at normal anatomical positions relative to other intra-thoracic organs. To mimic the attachment of the subcostal and 8 intercostal arteries, tied contacts were defined between the 9 groups of aortic nodes (see Figure 6.2E) and T4-T11 segments with the LS-DYNA keyword "*CONTACT_TIED_NODES_TO_SURFACE". The interfaces of the original GHBMC heart-aorta and the surrounding organs were modeled with a general automatic-single-surface. In order to independently adjust the parameters for each contact pair and to better reproduce the interaction phenomenon, individual surface-to-surface contacts were defined between the FSI heart-aorta and the surrounding GHBMC components (i.e. lungs, diaphragm and spine). Node-to-surface tied contacts were also defined between the pulmonary arteries/veins and the lung roots to attach the FSI heart with the GHBMC lungs. The superior arteries of the aorta were elongated to attach to the clavicles by sharing common nodes in order to reproduce the physiological constraints at the aortic arch. The FSI fluid domain was enlarged in order to contain the possible fluid space as the heart and aorta moved and deformed with the thoracic deformation during MVCAs. This point was always ensured during the following car crash simulations.

Car crash simulations

Full scale

The car crash simulations were based on two car crash accidents (one oblique-frontal and one lateral impact) involving BARs. The oblique-frontal crash case was reconstructed in Chapter 4.3 with the original GHBMC-M50 model while the lateral impact was reconstructed in Chapter 5.2 with the integrated full body FSI model. The detailed information of both accidents could be found in Chapter 4.3 and Chapter 5.2. To compare the results of the two models and to complete the whole study, the oblique-frontal and lateral crashes were respectively reconstructed with the integrated full body FSI model (Figure 6.3A) and the original GHBMC-M50 model (Figure 6.3B). Since the difference between the original GHBMC and integrated FSI model was only for the heart and aorta, the current simulation configurations were the same as the previous ones. To briefly review the configurations, the integrated FSI model, which was constrained by a seatbelt with 6kN-load-limit retractor, was subjected to crash deceleration loadings reconstructed from the oblique-frontal impact case (Figure 6.3A). The original GHBMC-M50 model constrained by the same seatbelt was impacted by the vehicle side structures, the deformations and kinematics of which were reconstructed from the vehicle-pole side impact (Figure 6.3B). The simulation with original GHBMC model was hereafter referred as *Original GHBMC* and the simulation with the integrated FSI model was referred as *Integrated FSI*.

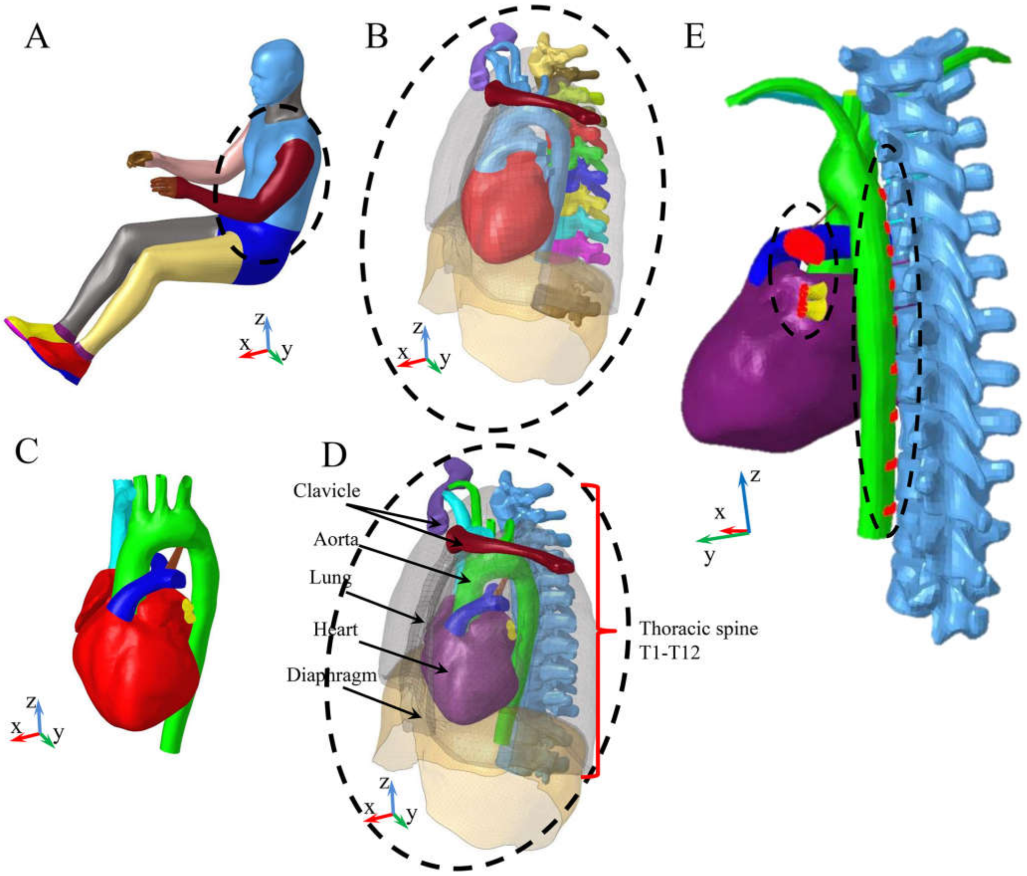

Figure 6.2 Model integration based on the GHBMC-M50 and the heart-aorta FSI models: (A) the original GHBMC-M50 model; (B) the partial enlarged figure to show the original GHBMC intra-thoracic organs with the lungs transparent; (C) the isolated heart-aorta FSI model; (D) the partial enlarged figure to show the intra-thoracic components of the integrated full body model; (E) the back-oblique view of the integrated model to show the groups of nodes, which are the red dots in the black dashed regions, for defining the “node-to-surface” tied contacts.

Sub-model scale

The full-scale simulations with the *Integrated-FSI* model were extremely long (e.g. about 45 days for a 120-ms crash duration on a workstation with 40 processors as mentioned in Chapter 5.2.5). In order to reduce the calculation expenses, sub-model scale simulations were performed for both crash cases which had been simulated in full-scale. The sub-model was obtained by extracting the thoracic components of the *Integrated FSI* model. The sub-model for both crash cases consists of heart, aorta, lungs, diaphragm, thoracic spine, fluid domain, etc (displayed in Figure 6.2D). The inputs of sub-model simulations were cardiac heartbeat of the isolated FSI model (see Chapter 5.2.2) and the kinematics of the intra-thoracic organs including the lungs, diaphragm, clavicle and thoracic spine. The kinematics of these organs was inherited from the full-scale simulations with original GHBMC model for the oblique-frontal (see chapter 0) and lateral (see the full-scale above0) crashes by two steps:

- These intra-thoracic organs which could interact with the heart and aorta during the crash were grouped in the full-scale phase, so that their kinematics was recorded in separate binary interface files (using LS-DYNA keyword *INTERFACE_COMPONENT_NODE);
- These interface files were imported to the sub-model simulations to prescribe the motions of the intra-thoracic organs during the whole crash durations (using LS-DYNA keyword *INTERFACE_LINKING_SEGMENT).

The sub-model scale FSI simulations were hereafter referred as *Sub-model FSI*.

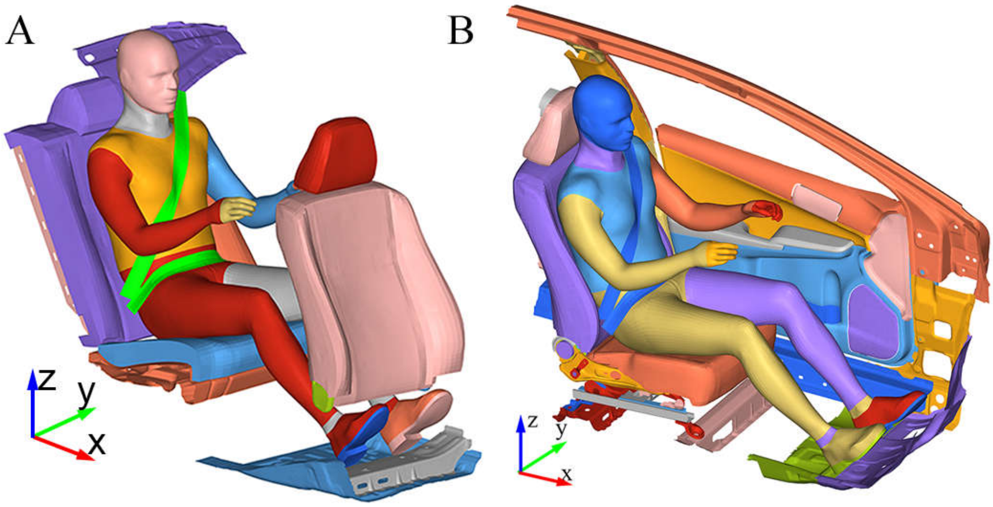

Figure 6.3 Oblique-frontal impact simulation with the *Integrated FSI* model (A) and lateral impact simulation with the *Original GHBMC* model (B)

6.1.3 Results

The calculation expenses on an Intel Xeon (2.57 GHz) workstation with 40 processors were summarized in Table 6.1 for the full scale and sub-model scale oblique-frontal and lateral crash simulations. The *Integrated FSI* simulation for lateral crash was the only simulation which reproduced blood flow in the crash duration and terminated without error. The *Integrated FSI* for oblique-frontal crash or the *Sub-model FSI* for lateral or oblique-frontal crash terminated with error of "negative volume in advection redo cycle".

The aorta VonMises stress and maximum principal strain distributions at the moment when peak values occurred were displayed in Figure 6.4 for all the complete simulations, i.e. *Original GHBMC* oblique-frontal crash*, Original GHBMC* lateral crash and *Integrated FSI* lateral crash simulations. The aorta peak stress and strain occurred at t=100ms during the *Original GHBMC* lateral and oblique-frontal crash simulations, while the peak values occurred at t=90ms during the *Integrated FSI* lateral crash simulation. The peak aortic stress and strain were respectively 1.2MPa and 12.2%, both located at the posterior part of aortic arch, during the *Original GHBMC* oblique-frontal crash simulation. The corresponding values were 1.1MPa and 6.0%, both located at the distal DA attaching to the diaphragm, during the *Original GHBMC* lateral crash simulation.

The corresponding values were 1.81MPa and 40.0%, both located at the aortic isthmus, during the *Integrated FSI* lateral crash simulation.

Table 6.1 Calculation expenses of the *Original GHBMC*, *Integrated FSI* and *Sub-model FSI* simulation for 120ms-duration oblique-frontal and lateral crashes

Simulations	Oblique-frontal crash			Lateral crash		
	Original GHBMC	*Integrated FSI*	*Sub-model FSI*	*Original GHBMC*	*Integrated FSI*	*Sub-model FSI*
Durations	**52h**	243h* (31ms)	178h* (48ms)	**64h**	**1081h**	135h* (39ms)

*These simulations terminated with errors and the calculation expenses were for the available simulation durations.

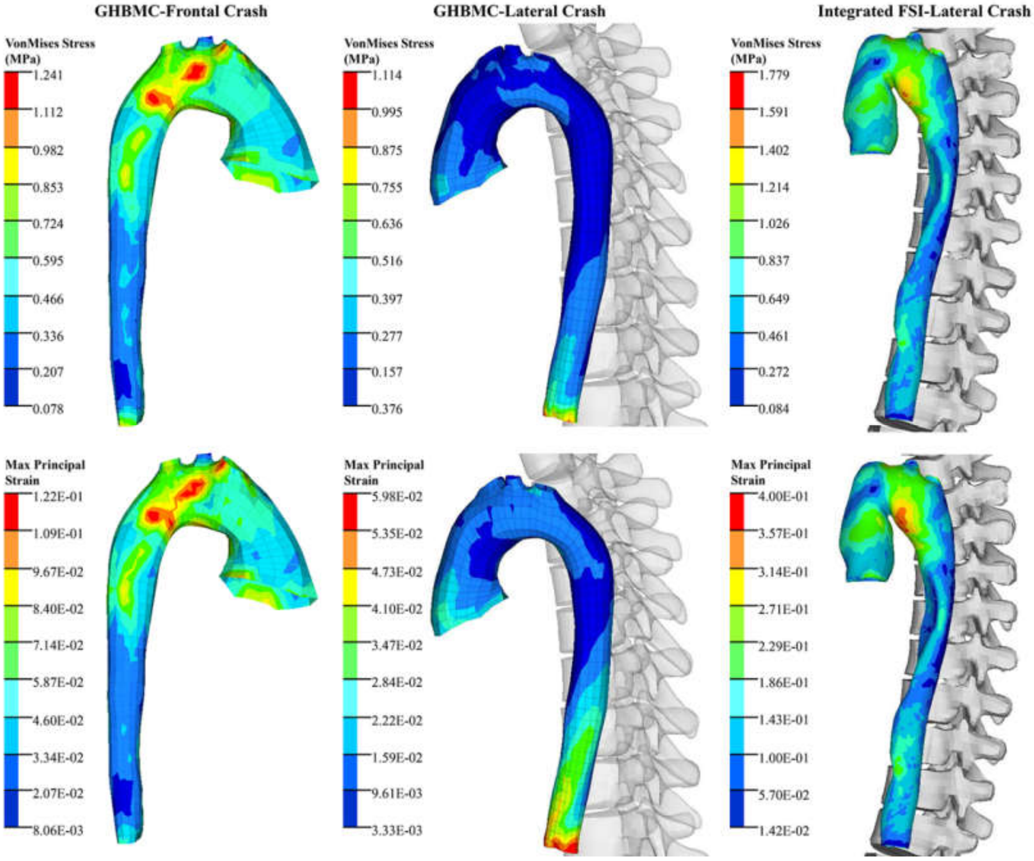

Figure 6.4 Aortic stress and strain distributions of the *Original GHBMC* and *Integrated FSI* simulations for oblique-frontal and lateral crash

6.1.4 Discussion

To reproduce aortic blood flow in MVCAs, the available FSI algorithms in LS-DYNA may be not stable enough for the complete crash durations, as three out of four FSI simulations (integrated and sub-model FSI) terminated with “negative volume” errors during the fluid advection redo cycles. The FSI simulations (the integrated one or the sub-model ones) stopped even before the aorta interacted with other intra-thoracic organs and before the intra-aortic pressure increased (t≤50ms) (see Figure 5.11 in Chapter 885.2). Second-development in LS-DYNA FSI algorithm might be necessary to improve the simulation stability, as numerous parameter options were tested but proved useless for the simulations.

The FSI simulations were significantly more time-consuming than the pure structural simulations (i.e. the *Original GHBMC*). The calculation expense of the *Integrated FSI* was about 18 times higher than that of the *Original GHBMC* for the lateral crash. Although being about 8 times as long as the *Original GHBMC* simulations for the same crash duration, the *Sub-model FSI* simulations were significantly shorter than the *Integrated FSI* ones. If the calculation stability could be ameliorated, the *Sub-model FSI* strategy would be a promising approach to reduce the calculation expense.

In the *Original GHBMC* oblique-frontal crash simulation, the aorta had a concentration of stress and strain at the posterior part of aortic arch. These peak values of the aortic stress and strain seemed to indicate the possible injury at the aortic arch according to the aortic stress levels reproduced in lateral collisions[19] and the failure thresholds recorded in aorta dynamic stretch tests [52]. However, after carefully examining the simulation, the stress and strain concentrations were found to result from the compressive force due to relative movement between DA and thoracic spine transverse process. In human anatomy, the DA is confined to thoracic vertebral bodies by intercostal arteries and the relative movement between DA and thoracic spine is unusual [138]. The unrealistic relative movement was caused by the absence of intercostal artery modeling in the original GHBMC model. Therefore, the *Original GHBMC* peak aortic responses could not reflect the real injury mechanism in the oblique-frontal crash case.

In the *Original GHBMC* lateral crash simulation, the peak aortic stress and strain were located at the diaphragmatic aortic hiatus of distal DA. These results did not agree with the case injury report of aortic arch transection (see Table D1 in APPENDIX D). Firstly, the magnitude of the aortic strain might not be enough to cause aortic injury at this location, according to the failure thresholds recorded in aorta dynamic stretch tests [52]. Secondly, the location of the aortic stress and strain concentrations was not consistent with the injury location at aortic arch in the injury report. These discrepancies might also result from the absence of intercostal artery modeling in the original GHBMC model. The aortic stress and strain distributions in the *Integrated FSI* lateral simulation could support this explanation to some extent. As mentioned in model integration section of Chapter 6.1.20, intercostal arteries were modeled as "tied contact" between the DA and thoracic spine in the *Integrated FSI* model. In the *Integrated FSI* lateral crash simulation, the DA had no significant displacement relative to the thoracic spine while the AA with heart moved posteriorly to the thoracic spine. The relative motion between the mobile AA and constrained DA resulted in significant deformation and thus significant stress and strain levels at the aortic arch (displayed in Figure 6.4). The peak stress of 1.81MPa and strain of 40.0% at the aortic arch indicated its vulnerability to injury, according to the aortic stress levels reproduced in lateral collisions[19] and the failure thresholds recorded in aorta dynamic stretch tests [52]. This was consistent with the case injury report of aortic arch transection and also conformed to the injury mechanism of relative motion between AA and DA as proposed in [66, 67].

The analysis above proved that the constraint of DA by intercostal arteries played a great role in aortic injury reproduction. However, the contribution of the blood flow to the aortic stress and strain levels remained to be studied. The aortic wall in the *Integrated FSI* was defined as hyperelastic material (see Chapter 5.2.2) while it was assumed to be linear elastic in original GHBMC model. With different material types and properties, it was meaningless to compare the aortic stress levels between the *Original GHBMC* (without blood flow or initial intra-aortic pressure) and *Integrated FSI* (with blood flow and pulsatile intra-aortic pressure). Therefore, it was impossible to postulate the effects of the blood flow on aortic injury. Additional simulations, which have the same aortic material properties and the same boundary conditions but different intra-aortic pressure conditions, remain to be performed in order to have more information about how the aortic responses vary with different intra-aortic pressures.

6.2 Aortic stress level under different intra-aortic pressure conditions in MVCAs

6.2.1 Introduction

Previously in Chapter 3.3, aorta stress and stretch levels during physiological cardiac cycle were found comparable with those reproduced in MVCAs [17, 19, 21, 101] and in stretch failure tests [98, 100]. We suggested that physiological cardiac pressure should be simulated in order to include the aortic responses resulting from initial luminal pressure for better BAR prediction. The aortic responses expected in MVCAs came from previous studies with different human FE models, which modeled the aortic wall with different materials. These aortic materials were also different from the aortic material of our model. The aortic responses could be highly different with different material properties but with the same boundary conditions. In Chapter 4.3, aortic luminal pressure was considered to be critical for BAR prediction in MVCAs. However, this conclusion was based on the aortic blood pressure reproduced in GHBMC model which simulates blood with elastic Lagrangian solid elements and does not simulates blood flow or initial intra-aortic pressure. Therefore, the contribution of blood flow and initial cardiac pressure to aortic stress and strain levels during MVCAs remain to be studied.

In Chapter 4.3, aortic mobility in terms of aortic deflection under 50mmHg and 200mmHg was assessed by performing mini-sled tests. The aortic deflection was found significantly affected by the initial intra-aortic pressure level. However, as we admitted in the limitation of the study in Chapter 4.3.4, no surrounding organs or realistic anatomic aortic constraints to limit the aortic arch movement were mimicked in the mini-sled tests. Therefore, the aortic arch mobility under realistic anatomic boundary conditions and under different initial luminal pressures remains to be quantified during MVCA.

Considering these contexts above, the objective of the following study is twofold: 1) to investigate the contribution of blood flow and initial luminal pressure on aortic responses during MVCA; 2) to identity the effect of initial luminal pressure on aortic mobility with realistic intra-thoracic boundary conditions during MVCA.

6.2.2 Material and methods

The *Integrated FSI* lateral crash simulation presented in Chapter 5.2 and Chapter 6.1 were used here to present the aortic responses (stress, strain and mobility) under the effects of initial intra-aortic pressure and pulsatile blood flow. We previously found in Chapter 6.1 that LS-DYNA FSI algorithms were not usually stable and the FSI (full-scale and sub-model) simulations were significantly more time-consuming than pure structural simulations. Moreover, the difference of aortic responses under a static pressure was found ignorable between the simulation approaches of FSI and structural pressure modeling [23]. Therefore, the structural pressure modeling approach was chosen to quantify the aortic responses under different initial luminal pressures during MVCA. The simulation configurations were the same as those of the *Sub-model FSI* lateral crash, except that no ALE or Eulerian components were used in these structural simulations. To be more specific, the structural components (including heart, aorta, thoracic spine, diaphragm, etc.) were extracted from the *Sub-model FSI* lateral crash model, with the fluid domain and the FSI-relevant keywords excluded. The LV in current simulations did not beat to pump blood into aorta, not like in *Sub-model FSI* simulation. Instead, the lumen enclosed by LV and aorta was currently defined as an airbag. The airbag was filled with blood which was assumed to be linear elastic fluid, similar with what was done in [18].

The initial pressure of airbag (lumen of LV and aorta) before impact was set as 0mmHg, 50mmHg and 120mmHg respectively in 3 simulations, hereafter referred as *Airbag-0mmHg*, *Airbag-50mmHg* and *Airbag-120mmHg*. Similar with *Sub-model FSI* lateral simulation, the motions and deformations of the intra-thoracic organs (i.e. lungs, thoracic spine, clavicles and diaphragm) were inherited from the *Original GHBMC* lateral crash (see Chapter 6.1.2) as the boundary conditions for these three structural airbag simulations. The airbag pressure time-history was recorded during the crash for the simulations. Six nodes (N1-N6) were distributed along the aorta outer surface from aortic root to the aortic section at vertebrae T7 level (displayed in Figure 6.5). A local coordinate system, the initial directions of which were the same as those of the global space system, was fixed on vertebrae T7. The displacements of the six nodes N1-N6 relative to the local system were recorded and measured to quantify the aortic motions during crash. To be noted, each thoracic vertebra was modeled as rigid body. Therefore, the relative displacements of the aortic nodes to the local system were independent from the location where the local system was fixed on T7. The aortic stress and strain distributions were recorded and compared among the airbag structural simulations and the *Integrated FSI* lateral crash.

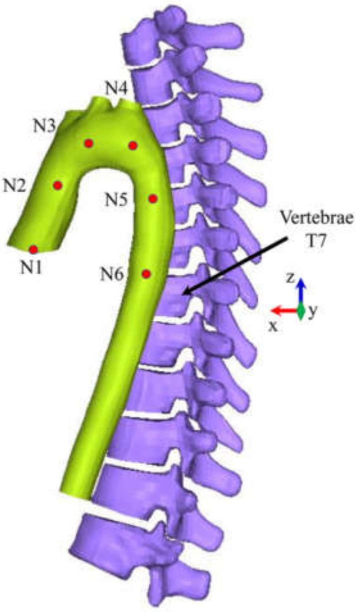

Figure 6.5 Aortic mobility measurement relative to vertebrae T7 with the global space system

6.2.3 Results

The aortic mobility represented by the aortic nodal resultant displacements relative to T7 was displayed in Figure 6.6 for *Airbag-0mmHg*, *Airbag-50mmHg*, *Airbag-120mmHg* and *Integrated-FSI* simulations. Figure 6.7 displayed the aortic luminal pressure time-histories for *Airbag-0mmHg*, *Airbag-50mmHg* and *Airbag-120mmHg* as well as the blood pressure time-history measured at the aortic root during *Integrated-FSI* simulation. The peak luminal pressure was respectively 305mmHg, 346mmHg and 410mmHg for *Airbag-0mmHg, Airbag-50mmHg and Airbag-120mmHg*, all occurring at t=75ms. The peak intra-aortic pressure was 450mmHg during *Integrated-FSI* simulation, occurring at t=120ms.

The aorta VonMises stress and maximum principal strain distributions at the moment when peak values occurred were displayed in Figure 6.8 for *Integrated-FSI* simulation (t=90ms), *Airbag-0mmHg*, *Airbag-50mmHg* and *Airbag-120mmHg* (t=75ms for airbag simulations). The peak aortic stress and strain were respectively 1.78MPa and 40.0%, both located at the aortic isthmus, during the *Integrated FSI* lateral crash simulation. The peak aortic stress and strain were also located at the aortic isthmus for all the airbag structural simulations with the corresponding values summarized in Table 6.2.

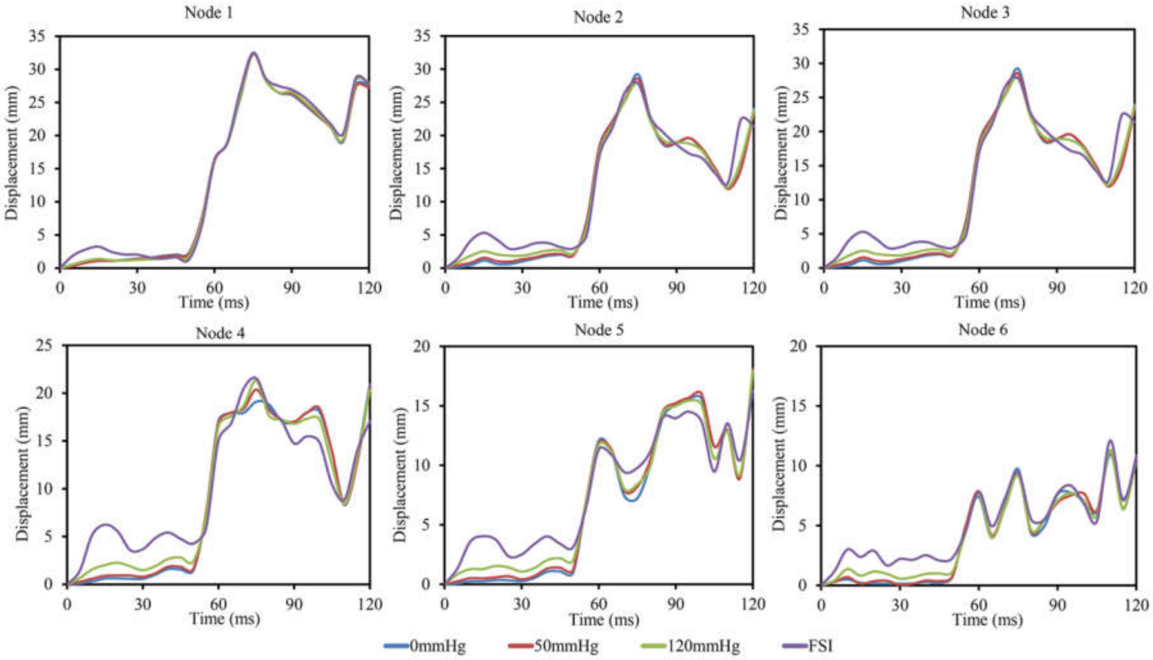

Figure 6.6 Aortic mobility in terms of aortic nodal displacements for *Airbag-0mmHg*, *Airbag-50mmHg*, *Airbag-120mmHg* and *Integrated-FSI* simulation

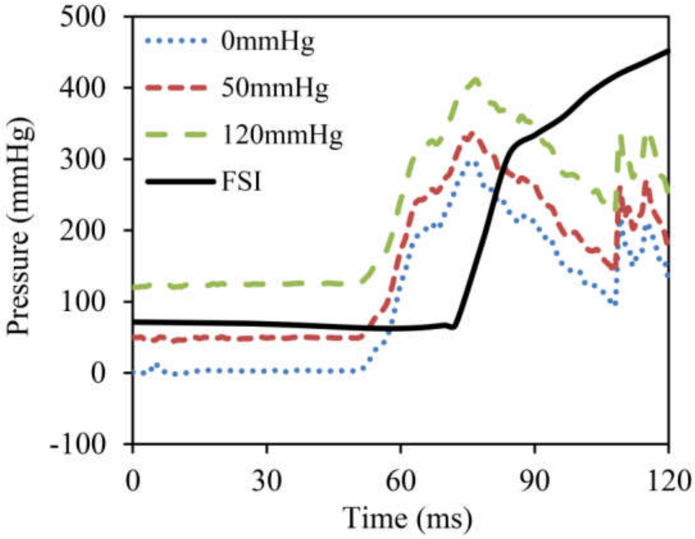

Figure 6.7 Airbag pressure time-histories during the crash for *Airbag-0mmHg*, *Airbag-50mmHg* and *Airbag-120mmHg* compared with the blood pressure measured at the aortic root during *Integrated-FSI* simulation

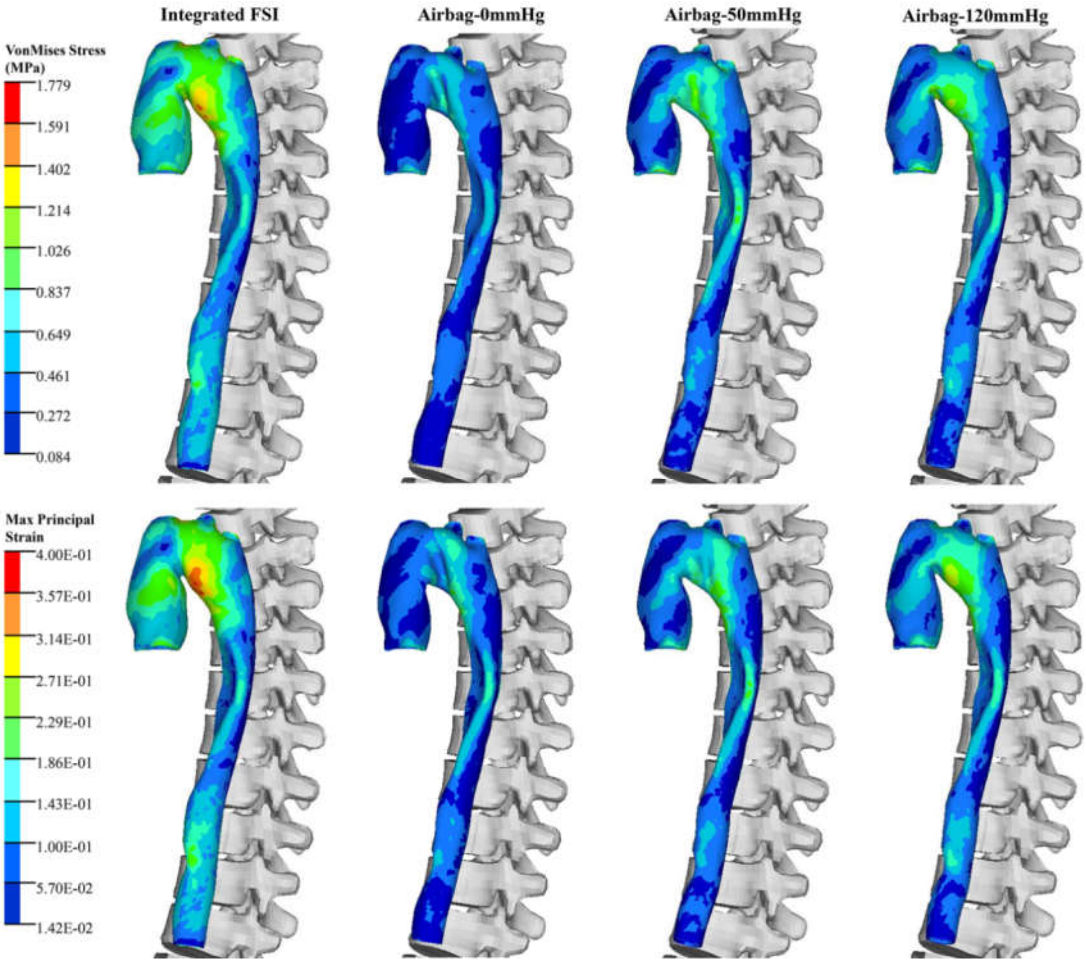
Integrated FSI
Airbag-0mmHg
Airbag-50mmHg
Airbag-120mmHg
VonMises Stress (MPa)
1.779
1.591
1.402
1.214
1.026
0.837
0.649
0.461
0.272
0.084
Max Principal Strain
4.00E-01
3.57E-01
3.14E-01
2.71E-01
2.29E-01
1.86E-01
1.43E-01
1.00E-01
5.70E-02
1.42E-02

Figure 6.8 Aortic stress and strain distributions of the integrated FSI and sub-model structural simulations for oblique-frontal and lateral crash

Table 6.2 Peak values of aortic VonMises stress and maximum principal strain during the simulations of *Integrated-FSI*, *Airbag-0mmHg, Airbag-50mmHg and Airbag-120mmHg*

Simulation	*FSI*[*]	*0mmHg*	*50mmHg*	*120mmHg*
Stress (MPa)	1.8	0.8	1.1	1.4
Strain (%)	40.0	16.6	22.0	29.0

[*] FSI, 0mmHg, 50mmHg and 120mmHg correspond to the simulations of *Integrated-FSI*, *Airbag-0mmHg, Airbag-50mmHg and Airbag-120mmHg.*

6.2.4 Discussion

Aortic mobility was quantified by computing the aortic nodal displacements relative to a coordinate system which was fixed on and translated with vertebrae T7. Therefore, the aortic mobility was rather the motion of different aortic sections relative to vertebrae T7 than the aortic absolute motion including the human body motion. The aortic nodal displacements were resultant magnitudes without considering their directions and thus the relative displacements between different aortic sections could not be calculated by simply subtracting their displacements. The peak displacements of AA (Node 1 and 2) and aortic arch (Node 3 and 4) occurred at the middle of crash duration (t=75ms) while the peak displacements of DA (Node 5 and 6) occurred at the end of crash duration (t=110~120ms). Along the aorta from Node 1 to Node 6, the peak displacement decrease, which confirmed that AA and aortic arch were relative mobile than DA, as previously postulated in [66, 67]. The nodal displacement time-histories were almost the same among different airbag simulations, with the magnitude differences always below 3mm (see Figure 6.6). The nodal displacement time-histories of *Integrated-FSI* had more vibrations than those of the airbag simulations, especially before the aorta contacted other intra-thoracic organs (t≤50ms). The vibrations might be caused by the heartbeat and the pulsatile intra-aortic pressure. Despite the curve vibrations, the aortic nodal motions during *Integrated-FSI* were consistent with those of the airbag simulations in shape and in magnitude. The magnitude differences of the aortic peak displacements between the *Integrated-FSI* and airbag structural simulations were always less than 3mm. The high proximity of the aortic mobility among the airbag structural and *Integrated-FSI* simulations indicated that the initial intra-aortic pressure levels might have no influence on the aortic kinematics or mobility at least in this lateral crash case. The effects of intra-aortic pressures on aortic mobility remain to be identified for more MVCA cases involving BARs.

The intra-aortic pressure increased significantly during the crash for the airbag structural and *Integrated-FSI* simulations. The peak pressures of airbag simulations occurred at the same time when the peak motions of AA and aortic arch occurred (t=75ms, see Figure 6.6 and Figure 6.7). In contrast, the peak pressure of *Integrated-FSI* occurred at t=120ms. If only considering the pressure-related injury, a BAR risk of 1.7%, 2.4%, 4.1% and 6.5% could result from the peak pressure of *Airbag-0mmHg, Airbag-50mmHg*, *Airbag-120mmHg* and *Integrated-FSI* according to the Bass curve [11]. Therefore, the aortic luminal pressure might not be the major cause of BAR in this case.

The intra-aortic pressure of airbag simulations (see Figure 6.7) was measured as the uniform pressure of the LV-aorta lumen. The pressure of *Integrated-FSI* was obtained by averaging the pressure values of the ALE fluid elements at the aortic root. In other words, the pressure of *Integrated-FSI* was only the local pressure at aortic root. The different approaches of quantifying the intra-aortic pressure in structural and FSI simulations might explain the significant difference of pressure time-histories between structural and FSI simulations. During the *Integrated-FSI*, the aorta had complex spatial motions and significant deformations at some aortic sections (e.g. aortic arch and middle DA). It was difficult to capture the complete pressure transition at these parts since the fluid elements located at these aortic sections were not always the same during the crash.

The deformed contours of aorta during FSI and airbag structural simulations were highly similar (see Figure 6.8). The peak values of aorta stress and strain were nevertheless different among the FSI and airbag structural simulations. In airbag structural simulations, the peak aorta stress and strain increased with the initial aortic lumen pressure. The peak values of aortic stress and strain during *Airbag-50mmHg* were 32.5% and 40.3% higher than the corresponding values during *Airbag-0mmHg*. The peak values of aortic stress and strain during *Airbag-120mmHg* were 75.0% and 74.7% higher than the corresponding values during *Airbag-0mmHg*. The aortic stress and strain during *Integrated-FSI* were 125% and 141.0% higher than the values during *Airbag-0mmHg*.

Belwadi [21] proposed a strain-based BAR risk curve, based on aortic maximal principal strains from a human FE model which had not been validated. If we assume the strain-based BAR risk curve to be accurate, the aorta peak strain during *Airbag-0mmHg, Airbag-50mmHg*, *Airbag-120mmHg* and *Integrated-FSI* corresponded to a BAR risk of 44.2%, 94.0%, 99.9% and 100%. In other words, the BAR risk would increase significantly (by 49.8~55.8%) if the initial intra-aortic pressure (static or pulsatile) was considered in the case reconstruction. On one hand, compared to *Airbag-0mmHg*, the increasing ratios of aortic stress, strain and BAR risk in *Airbag-50mmHg*, *Airbag-120mmHg* and *Integrated-FSI* suggested that the physiological intra-aortic pressure should be considered to better predict BARs in MVCAs. This finding is also consistent with our conclusion made in Chapter 3.3. On the other hand, without considering the aortic stress/strain resulting from aortic relative motion, the pressure-related BAR risk was previously estimated to be 1.7%~6.5% for *Airbag-0mmHg, Airbag-50mmHg*, *Airbag-120mmHg* and *Integrated-FSI*. The high risk of BAR in *Airbag-0mmHg* with the even higher values in other simulations further proved that the aortic deformation resulting from the relative motion between different sections should be the major cause of BAR in this case with the intra-aortic pressure as the secondary cause.

The initial intra-aortic pressure of *Integrated-FSI* was about 70mmHg, between the initial pressures of *Airbag-50mmHg and Airbag-120mmHg*. The aorta peak stress and strain of *Integrated-FSI* were nevertheless 28.6% and 37.9% higher than the values of *Airbag-120mmHg*. The higher responses at the aortic isthmus in *Integrated-FSI* might be attributed to the additional intra-aortic pressure resulting from local blood flow occlusion (i.e. “water hammer effect”). Unfortunately, we could not capture the intra-aortic pressure at the aortic isthmus due to the technical issue (the fluid domain translated with AR and thus the fluid elements located at isthmus were not always the same aorta due to the complex spatial motions and significant deformations of the aorta). The higher aortic stress and strain in *Integrated-FSI* resulted in a BAR risk which was only 0.1%~6.0% higher than that in *Airbag-50mmHg* and *Airbag-120mmHg.* This slight risk increase could be explained by the fact: the aortic strains in *Airbag-50mmHg* and *Airbag-120mmHg* were high enough to cause a high BAR risk (94%~99.9%) so that the contribution of “water hammer effect” to the injury risk seemed quite limited. The effects of “water hammer effect” on aortic responses and on BAR risk remain to be investigated in more MVCAs involving BARs.

6.3 Conclusion

This chapter consists of two studies. Firstly, the aortic responses in MVCA including blood flow and intra-thoracic interactions were investigated by reconstructing two BAR-related MVCA cases. Before the case reconstruction, the isolated heart-aorta FSI model was integrated with the GHMBC-M50 model so that the integrated human model was able to reproduce blood flow and intra-thoracic interactions during MVCAs. Full-scale GHBMC, full-scale and sub-model FSI simulations were used to reconstruct the MVCA cases. Among the full-scale and sub-model FSI simulations, only the full-scale FSI lateral crash (*Integrated FSI*) terminated without error while the other 3 FSI simulations terminated with error of “negative volume in advection redo cycle”. The FSI algorithm was not as stable as the *Original GHBMC* simulation in LS-DYNA. The full-scale FSI was also significantly more time-consuming than the *Original GHBMC* simulations. However, if the FSI stability was improved, the sub-model FSI might be a promising approach to reproduce blood flow in MVCAs and to reduce the calculation expenses.

Despite the stability and calculation expense issues, the *Integrated FSI* lateral simulation reproduced realistic aortic injuries as described in the case report. In contrast, the *Original GHBMC* oblique-frontal and lateral simulations could not mimic the reasonable aortic deformations due to the lack of modeling intercostal arties to constrain the DA. The DA constraint by intercostal arteries should play a great role in BAR reproduction. These results also indicated the aortic relative motion between AA and DA should be possible BAR mechanism in this lateral crash case.

Secondly, aortic responses under different intra-aortic pressure conditions in MVCAs were investigated by performing sub-model airbag structural simulations. The LV-aorta lumen was defined as airbag and was filled with linear elastic fluid of 0mmHg, 50mmHg and 120mmHg, respectively. The intra-aortic pressure, aortic mobility, stress and strain were compared among the airbag structural and *Integrated FSI* simulations. The static or pulsatile luminal pressures showed no effect on aortic kinematics or mobility. AA and aortic arch were found to be relative mobile than DA, which was consistent with previously published viewpoint. The intra-aortic pressure increased during the crash for the airbag and FSI simulations without causing significant pressure-related risk of BAR. This finding suggested the intra-aortic pressure should not be the primary cause of injury in this case. The aortic stress and strain were found to increase with the initial intra-aortic pressures during the airbag structural simulations. The aortic stress and strain during *Integrated FSI* were higher than those during all airbag simulations. The aortic strain in the *Integrated FSI* and airbag simulations of physiological intra-aortic pressures (*Airbag-50mmHg* and *Airbag-120mmHg*) could cause a BAR risk above 90% which was two times as high as the BAR risk in *Airbag-0mmHg*. This result proved that physiological intra-aortic pressure should be considered to better predict BARs in MVCAs. It could also be postulated that the aortic relative motion should be the major cause of BAR in this case with the intra-aortic pressure as the secondary cause.

CHAPTER 7 GENERAL DISCUSSION AND CONCLUSION

Aorta is one of the major arteries in the human body and BAR is the second leading cause of death following blunt trauma in MVCAs. The majority of BARs occurring in MVCAs were found in vehicle occupants (53.5%), followed by pedestrians, motorcyclists, bicyclists and truck occupants. BAR could often cause catastrophic consequences with 85% of the victims deceased at the collision scene and 30% of the remaining untreated victims deceased within 24 hours. Various injury mechanisms of BAR have been proposed, including sudden stretching of the aorta with rupture at isthmus; entrapment of the aorta by the surrounding bony structures; sudden stroke of blood pressure with what is referred to in literature as the water hammer effect and the combination of different mechanisms including these above. In our study, these injury mechanisms were generally categorized into two sources of contributions which are aortic distraction and intra-aortic pressure. The aortic distraction is related to aortic motions resulting from thoracic compression and was postulated to be a primary BAR mechanism. However, the intra-aortic pressure effects on BAR remain to be controversial.

To investigate the injury mechanisms of BAR, experimental and numerical approaches have been previously used. The previous experimental researches were usually performed as ex-vivo experiments with animal or human cadaver samples. These experiments often had difficulties in reproducing BARs due to the difficulty of reflecting the realistic boundary conditions which aorta sustains in MVCAs. Moreover, the experimental studies also had difficulties in providing such information as aorta stress and strain which could be promising index for investigating BAR mechanisms. In contrast, human FE models used for numerical approach would have advantages over experimental approach in reproducing realistic boundary conditions and in providing straightforward aortic injury information when studying MVCA-related BAR mechanisms. However, the previous human FE models for MVCA-related BAR researches used to ignore the effects of intra-aortic pressure or intra-thoracic organ interaction on aortic responses. Moreover, even if the human FE models took into account of the intra-aortic pressure effect on aortic responses, the aortic lumen was not filled with blood of physiological pressure levels. It was unclear whether the initial intra-aortic pressure should play a great role in aortic responses during MVCAs.

With the context above, the objective of the current work is to investigate BAR mechanisms in MVCAs with a focus on intra-aortic pressure mechanism. To achieve this final objective, the current work could be divided into four sections to correspondingly answer the four following questions (displayed in Figure 1.1):

1) Is it reasonable to ignore cardiac function in MVCA-related BAR studies? (Chapter 3)

2) Does intra-aortic pressure contribute significantly to BAR in MVCA? (Chapter 4Chapter 3)

3) Is it possible to simulate intra-aortic pressure including cardiac function to study MVCA-related BAR mechanisms? (Chapter 5)

4) How are the aortic stress levels and the BAR mechanisms if considering physiological intra-aortic pressures and intra-thoracic interactions in MVCAs? (Chapter 6)

To answer question: 1) how are the aortic response (stress/strain) levels under physiological cardiac loadings? The AR in-plane motion was firstly assessed in Chapter 3, since the physiological cardiac loadings on aortic wall mainly consist of the luminal pressure and the ventricular traction at AR due to heartbeat. The AR 3D spatial motion resulting from the ventricular traction could be decomposed as AR longitudinal (along AA lumen longitudinal direction) and in-plane (perpendicular to AA lumen longitudinal direction) motions. The AR longitudinal displacement was previously reported as the mean value of 8.9mm with a range of 6.4-11.3mm [81] while previous studies on AR in-plane motions were quite limited without mentioning the component displacements in the anterior-posterior or the lateral direction [82, 83]. Therefore, our measurement on AR-in plane motion based on MRI data from 25 healthy volunteers provided detailed information about the AR in-plane component displacements which were measured under the MRI and local PDA systems. The X and Y components under MRI system were measured as 3.1±0.9mm and -4.4±1.7mm while the corresponding values under PDA system were 3.0±1.3mm and 3.1±1.5mm.

The detailed AR in-plane motions together with the previously reported AR longitudinal displacement and the commonly known physiological intra-aortic pressure allowed us to quantify the aortic response levels under cardiac loadings. The aortic responses were evaluated with an aorta FE model which was reconstructed from end-diastolic MRI data of a young healthy volunteer. The stress-free configuration of the model was obtained by reversely imposing diastolic pressure on aortic exterior surface and was then validated against the distensibility by imposing cardiac luminal pressure. Based on the validated aorta model, the aortic stress and stretch were quantified under various loading conditions: 1) intra-aortic pressure of 120mmHg; 2) 120mmHg pressure and AR longitudinal displacement of 8.9mm; 3) 120mmHg pressure, AR longitudinal (8.9mm) and in-plane (3.1mm and -4.4mm for XY components) displacements; 4) 120mmHg pressure, AR longitudinal (8.9mm) and excessive in-plane (6.2mm and -8.8mm for XY components) displacements. The peak values of aortic stretch and VonMises stress were 1.48 and 0.25MPa, always located at the interior curvature of aortic arch distal to AA during all the simulations. The peak aortic stretch and VonMises stress were independent from the simulated loading conditions. The AR longitudinal or in-plane motion displayed no effect on aortic wall stress distribution. Although the AR longitudinal increased the AA longitudinal stress, the increasing AA stress up to 0.084MPa was far below the aortic longitudinal stress threshold of 1.21±0.09MPa [100] to increase AA dissection risk. Therefore, the aortic responses under cardiac loadings mainly result from the aortic luminal pressures.

The aortic responses under cardiac loadings were additionally compared among the simulations of different approaches to impose luminal pressure: 1) static structural pressure, 2) static FSI pressure and 3) static FSI pressure with blood flow. The aortic responses including luminal volume, aorta diameters and stresses were found to be equivalent between the simulations of static structural and FSI pressure with their differences below 1%. However, the aortic stresses, luminal volume and radial dilation during the simulation of static FSI pressure with blood flow were respectively 6.4-7.5%, 3.0% and 1.1-2.9% less than the corresponding values in the simulation of static structural pressure. These differences were caused by the pressure gradient along the aorta to maintain the blood flow in the simulation of FSI pressure with blood flow. Therefore, it is necessary to mimic the non-uniform hydrodynamic pressure ambient in the aorta with the FSI blood flow simulation approach, if we need to accurately reproduce the aortic responses under cardiac cycle.

The peak aortic stress and stretch under cardiac loadings were compared with those reproduced in MVCAs and aorta stretch failure tests. The aortic stresses due to cardiac cycle were 28.3%~29.8% of the aortic failure thresholds while the stretch ratios were about 67.1~70.5% of the stretch thresholds. The physiological aortic stresses were also comparable with the stress levels reproduced in MVCAs involving BARs. Therefore, the aortic response due to cardiac function should be considered in MVCA-related BAR researches.

To answer question: 2) is it necessary to consider intra-aortic pressure for BAR prediction in MVCAs? We attempted to investigate the effects of intra-aortic pressure on MVCA-related BARs in Chapter 4 from two independent perspectives: 1) whether aortic luminal pressure affects aortic mobility which has been considered critical to BARs and 2) whether the increasing luminal pressure during MVCAs can lead to BARs directly. A preliminary study was firstly conducted to determine the aortic pressure threshold leading to BAR. Since there was only one previous experimental study on quantifying this threshold for human aortas [11] with a loading rate (720kPa/s) corresponding to high-speed impact conditions, this preliminary study was thus aimed to determine the threshold with a loading rate (56.5kPa/s) corresponding to relatively low-speed impact conditions. The mean value of aortic rupture pressures was 131.9±11.8kPa with 44% of cases (4 out of 9 aortas) ruptured at aortic peri-isthmus. The mean pressure versus time before aortic rupture and the corresponding experimental corridors were also presented in Chapter 4.2. The BAR risk curve against the rupture pressures was developed using Weibull survival model with the luminal pressure of 133kPa corresponding to a risk of 50%.

To identify the effect of intra-aortic pressure on aortic mobility, mini-sled tests (*Impact-10°* and *Impact-20°*) were performed with each aorta sample pressurized to 50mmHg (6.7kPa) and 200mmHg (26.7kPa). The aortic deflections along the impact direction were recorded and compared between both pressure levels. For *Impact-10°*, the mean values of peak aortic deflections were 1.9±1.0cm and 1.1±0.5cm respectively under 50mmHg and 200mmHg. For *Impact-20°*, the corresponding values were 3.7±1.8cm and 2.4±0.9cm. In both impact series, the aortic deflections under 50mmHg were correlated with and significantly higher than the deflections under 200mmHg, indicating the significant effects of intra-aortic pressures on the aortic mobility under current impact loading conditions. To our knowledge, our study proposed the hypothesis for the first time that intra-aortic pressure has significant effects on aortic mobility. Nevertheless, as we also admitted in Chapter 4.3, these aortic deflections should not be considered as those experienced by aortas in real intra-thoracic conditions, for two main reasons: there are no surrounding organs limiting (or increasing) somehow the movements of the aortic arch; the tests do not reflect the realistic anatomic constraints of aorta (e.g. tethering from the superior aortic branches and ligamentum arteriosum). Therefore, this hypothesis still remains to be identified in intact intra-thoracic environments during MVCAs.

Finally, an oblique-frontal real car crash case involving BAR was reconstructed to deal with the perspective about pressure-related BAR risk in MVCAs. The accident case was extracted from the CIREN database and reconstructed with equivalent vehicle and occupant FE models. The numerical reconstruction was validated against the car frontal intrusions and the victim injury descriptions, both of which were reported in the database. The reconstructed maximum vehicle intrusions were 55cm while the average difference of intrusions was 8.5% between the simulation and case report. A peak resultant acceleration of 28.9g was reconstructed in the crash simulation, which resulted in peak stress and strain levels at the occupant’s diaphragm, lung, ribs and aorta corresponding to the similar case injury descriptions. A peak aortic luminal pressure of 135kPa was predicted at the location of AR. The peak pressure level was within the ranges previously reproduced in lateral impacts [19, 21]. Referring to the pressure-based injury curves reported in [11] and in Chapter 4.2 of our work, the reproduced peak pressures could induce a BAR risk above 50%. The risk would be even higher if considering the additional water hammer pressure which was not simulated in the human body model. The possible high pressure-induced BAR risk in the reconstructed case justified the necessity of considering intraluminal pressure for MVCA-related BAR studies. This could be achieved ideally by simulating cardiac blood flow instead of imposing a uniform static pressure in the aorta to involve both hydrostatic pressure and water hammer effect. Even if intraluminal pressure was proved to be offset by comparable extra-aortic pressure in collisions as suggested [12], it is still essential to consider pressure distributions inside and outside aorta for BAR researches.

To answer question: 3) is it possible to develop a human FE model which can simultaneously reproduce blood flow (intra-aortic pressure) and intra-thoracic interactions effects for MVCA-related BAR researches? A FE model of the isolated aorta-heart system was firstly developed with FSI approach. The model geometry was validated against LV volume and aortic diameters at different sections. The model was meshed with a number of elements which was determined after a mesh-convergence analysis was conducted against section-averaged blood velocity with a 1% threshold. An Eulerian grid with ALE formulation was constructed to model the fluid domain. Three coupling interfaces were constructed between the fluid and the structure components: aorta, LV and a simplified aortic valve. The interaction between solid and fluid domain was modeled by activating the penalty coupling algorithm parameter in LS-DYNA FSI keyword. In order to reproduce blood flow during the whole cardiac cycle, a time-dependent loading was applied on the LV internal wall to simulate the LV contraction and relaxation. The aorta-heart FSI model was validated against various cardiac outputs, such as LV volume and pressure time-history, blood flow velocity and WSS at different aortic sections. The realistic cardiac outputs proved that it was possible to reproduce blood flow by modeling heart beat with FSI approach in the isolated aorta-heart system.

The validated heart-aorta FSI model was subsequently integrated with the GHBMC M50 model to identify the possibility of reproducing blood flow in MVCAs. The original GHBMC components of heart, aorta and blood were replaced by the heart-aorta FSI model. Tied contacts were defined between the 9 groups of aortic nodes and T4-T11 segments to mimic the attachments of the subcostal and 8 intercostal arteries which were ignored in the original GHBMC model. Using the *Integrated FSI* model, a vehicle side-impact case involving BAR was reconstructed by validating the vehicle side intrusions and the occupant injuries against the case report descriptions. The maximum vehicle intrusion was 38cm while the average intrusion difference between the simulation and report was -5.3%. The *Integrated FSI* model reproduced bilateral rib fractures, diaphragm contusion and aortic arch transection, all of which were consistent with the case injury descriptions. The cardiac outputs (including LV stroke volume, the peak blood pressures recorded at LV and aortic section 1 and the peak blood velocity at aortic section 1) during the crash were also recorded and found to be elevated significantly by the impact loadings, compared to the normal outputs of the isolated heart-aorta FSI model during physiological cardiac cycle. The more intense cardiac output during MVCA proved our assumption that the occupant thoracic compression could significantly modify the blood flow conditions in the aorta. Moreover, the modification of cardiac output due to impact loadings could be captured by the heartbeat modeling approach with FSI rather than the traditional simulation approach of prescribe specific pressure loadings at the aortic inflow and outflow. These results altogether proved that it was possible to develop a human FE model which can simultaneously reproduce blood flow (intra-aortic pressure) and intra-thoracic interactions effects for MVCA-related BAR studies.

To answer the final question: 4) how are the aortic stress and strain levels if considering physiological intra-aortic pressures and intra-thoracic interactions in MVCAs? The oblique-frontal crash case which was simulated in Chapter 4.3 with the original GHBMC-M50 model was reconstructed with the *Integrated FSI* model. The lateral impact which was simulated in Chapter 5.2 with the *Integrated FSI* model was also reconstructed with the original GHBMC-M50 model. All the 4 simulations with *Original GHBMC* and *Integrated FSI* models for oblique-frontal and lateral crashes constituted the full-scale MVCA reconstructions. Due to the heavy calculation expenses of the full-scale FSI simulations, sub-model scale FSI simulations were performed for both cases. The sub-model FSI components were extracted from the *Integrated FSI* model (including heart, aorta, lungs, diaphragm, thoracic spine, fluid domain, etc). The inputs of the sub-model simulations were the cardiac heartbeat of the *Integrated FSI* model and the kinematics of the intra-thoracic organs inherited from the full-scale simulations. To reproduce aortic blood flow in MVCAs, the available FSI algorithms in LS-DYNA may be not stable enough for the complete crash durations, as three out of four FSI simulations (full-scale and sub-model FSI) terminated with advection-related errors. The full-scale FSI simulations were also significantly more time-consuming than the pure structural simulations (i.e. the *Original GHBMC*). If the calculation stability was ameliorated, the *Sub-model FSI* strategy could be a promising approach to reduce the FSI calculation expense.

The *Original GHBMC* oblique-frontal crash reproduced a peak aortic stress and strain of 1.2MPa and 12.2% at the posterior part of aortic arch. The *Original GHBMC* lateral crash reproduced a peak aortic stress and strain of 1.1MPa and 6.0%, both located at the distal descending aorta. The peak aortic stress and strain were 1.81MPa and 40.0%, both located at the aortic isthmus, during the *Integrated FSI* lateral crash simulation. The aortic stress and strain resulting from both the effects of cardiac blood flow (intra-aortic pressure) and intra-thoracic interactions during *Integrated FSI* lateral crash predicted the possible aortic isthmus transection, which was consistent with the case injury description. The *Original GHBMC* oblique-frontal and lateral simulations nevertheless did not mimic the reasonable aortic deformations due to the lack of modeling intercostal arties to constrain the DA. The DA constraint by intercostal arteries was considered to play a great role in BAR reproduction. These results also proved the possible injury mechanism of aortic relative motion between AA and DA in this lateral crash case.

Aortic stress and strain levels under different intra-aortic pressure conditions were subsequently compared by additionally performing sub-model scale structural simulations. The sub-model structural simulations were set up with the same configurations as those of the sub-model FSI simulation, except that no ALE or Eulerian components were used in structural simulations. Instead, the LV and aorta lumen was defined as an airbag which was filled with linear elastic fluid of initial pressure 0mmHg, 50mmHg and 120mmHg, respectively. The boundary conditions of these airbag simulations were the kinematics of the intra-thoracic organs inherited from the full scale GHBCM lateral crash simulation. By comparing the aortic arch deflections among the structural and *Integrated-FSI* simulations, the initial static or pulsatile luminal pressure was found to have no influence on the aortic kinematics or mobility at least in this lateral crash case. The effects of intra-aortic pressures on aortic mobility remain to be identified for other MVCA cases involving BARs. AA and aortic arch were found to be relative mobile than DA, which confirmed the previous postulation proposed in [66, 67]. The aortic luminal pressure was found to increase during the crash in all structural and FSI simulations, but the pressure increase levels were not sufficient to cause significant BAR risk alone. This finding suggested the intra-aortic pressure should not be the primary cause of BAR in this case. The aortic stress and strain were found to increase with the initial intra-aortic pressures during the airbag structural simulations. The aortic stress and strain during *Integrated FSI* were higher than those during *Airbag-120mmHg* simulation, while the initial pressure before impact (70mmHg) during FSI was less than 120mmHg. This indicated that the “water hammer effect” should have resulted from aortic blood flow occlusion and caused additional luminal pressure elevation. It was the additional pressure elevation that further increased aortic responses during *Integrated FSI*. The aortic strain in the *Integrated FSI*, *Airbag-50mmHg* and *Airbag-120mmHg* could cause a BAR risk above 90% which was two times as high as the BAR risk in *Airbag-0mmHg*. This result further proved that physiological intra-aortic pressure should be considered to better predict BARs in MVCAs, following the conclusion of Chapter 3. It could also be postulated that the aortic relative motion should be the major cause of BAR in this case with the intra-aortic pressure as the secondary cause.

REFERENCES

[1] Sevitt S. Fatal road accidents in Birmingham: times to death and their causes. Injury. 1973;4(4):281-93.

[2] Zeldenrust J, Aarts J. Traumatic aortic rupture in traffic accidents. Nederlands tijdschrift voor geneeskunde. 1962;106:464-8.

[3] Otte D, Facius T, Brand S. Injury Mechanisms of Aortic Ruptures to Vehicle Occupants and Vulnerable Road Users – An In-Depth-Investigation over Time. Journal of Forensic Biomechanics. 2017;8(1):132-143.

[4] Benjamin MM, Roberts WC. Fatal aortic rupture from nonpenetrating chest trauma. Proceedings (Baylor University Medical Center). 2012;25(2):121.

[5] Skarupa DI, Menaker I. Blunt aortic injury. Vascular Emergencies: Expert Management for the Emergency Physician. 2013:88.

[6] Moar J. Traumatic rupture of the thoracic aorta. S Afr Med J. 1985;67:383.

[7] Neschis DG, Scalea TM, Flinn WR, Griffith BP. Blunt aortic injury. New England Journal of Medicine. 2008;359(16):1708-16.

[8] Lundevall J. Traumatic Rupture of Aorta-With Special Reference to Road Accidents. Acta pathologica et microbiologica Scandinavica. 1964;62(1):29-.

[9] Hardy WN, Shah CS, Mason MJ, Kopacz JM, Yang KH, King AI, et al. Mechanisms of traumatic rupture of the aorta and associated peri-isthmic motion and deformation. Stapp car crash journal. 2008;52:233.

[10] Hardy WN, Shah CS, Kopacz JM, Yang KH. Study of potential mechanisms of traumatic rupture of the aorta using insitu experiments. Stapp car crash journal. 2006;50:247.

[11] Bass C, Darvish K, Bush B, Crandall J, Srinivasan S, Tribble C, et al. Material properties for modeling traumatic aortic rupture. Stapp car crash journal. 2001;45:143-60.

[12] Forman J, Stacey S, Evans J, Kent R. Posterior acceleration as a mechanism of blunt traumatic injury of the aorta. Journal of biomechanics. 2008;41(6):1359-64.

[13] Kroell CK, Schneider DC, Nahum AM, editors. Impact tolerance and response of the human thorax II. Stapp Car Crash Conference Proceedings; 1974.

[14] Viano DC. Biomechanical responses and injuries in blunt lateral impact. SAE Technical Paper, 1989 0148-7191.

[15] Viano DC. Chest impact experiments aimed at producing aortic rupture. Clinical Anatomy. 2011;24(3):339-49.

[16] Baqué P, Serre T, Cheynel N, Arnoux P-J, Thollon L, Behr M, et al. An experimental cadaveric study for a better understanding of blunt traumatic aortic rupture. Journal of Trauma and Acute Care Surgery. 2006;61(3):586-91.

[17] Richens D, Field M, Hashim S, Neale M, Oakley C. A finite element model of blunt traumatic aortic rupture. European journal of cardio-thoracic surgery : official journal of the European Association for Cardio-thoracic Surgery. 2004;25(6):1039-47.

[18] Shah CS, Hardy WN, Yang KH, Van Ee CA, Morgan RM, Digges KH. Investigation of the traumatic rupture of the aorta (TRA) by simulating real-world accidents. Proceedings of the 2007 International Research Council on Biomechanics of Injury, Maastricht, The Netherlands. 2007:349-59.

[19] Siegel JH, Belwadi A, Smith JA, Shah C, Yang K. Analysis of the mechanism of lateral impact aortic isthmus disruption in real-life motor vehicle crashes using a computer-based finite element numeric model: with simulation of prevention strategies. Journal of Trauma and Acute Care Surgery. 2010;68(6):1375-95.

[20] Belwadi A, Siegel JH, Singh A, Smith JA, Yang KH, King AI. Finite element aortic injury reconstruction of near side lateral impacts using real world crash data. Journal of biomechanical engineering. 2012;134(1):011006.

[21] Belwadi AN. Finite element reconstruction of real world aortic injury in near-side lateral automotive crashes with conceptual countermeasures. Ph.D. diss., Wayne State University; 2011.

[22] Lee S-H, Kent R. Blood flow and fluid-structure interactions in the human aorta during traumatic rupture conditions. Stapp car crash journal. 2007;51:211.

[23] Sturla F, Votta E, Stevanella M, Conti CA, Redaelli A. Impact of modeling fluid–structure interaction in the computational analysis of aortic root biomechanics. Medical engineering & physics. 2013;35(12):1721-30.

[24] Sundaram GBK, Balakrishnan KR, Kumar RK. Aortic Valve Dynamics using a Fluid Structure Interaction Model-The Physiology of opening and closing. Journal of biomechanics. 2015.

[25] Williams P L, Warwick R, Dyson M, et al. Gray's anatomy 37th ed[J]. Churchill Livingstone, Edinburgh, 1989..

[26] Standring S. Smooth muscle and the cardiovascular and lymphatic systems. Gray’s anatomy: the anatomical basis of clinical practice 40th ed Edinburgh: Churchill Livingstone. 2008:127-43.

[27] Parmley LF, Mattingly TW, Manion WC, Jahnke EJ. Nonpenetrating traumatic injury of the aorta. Circulation. 1958;17(6):1086-101.

[28] Greendyke RM. Traumatic rupture of aorta: special reference to automobile accidents. JAMA : the journal of the American Medical Association. 1966;195(7):527-30.

[29] Fabian TC, Richardson JD, Croce MA, Smith JS, Jr., Rodman G, Jr., Kearney PA, et al. Prospective study of blunt aortic injury: Multicenter Trial of the American Association for the Surgery of Trauma. The Journal of trauma. 1997;42(3):374-80; discussion 80-3.

[30] Jackson DH. Of TRAs and ROCs. Chest. 1984;85(5):585-7.

[31] Mattox KL. Fact and fiction about management of aortic transection. The Annals of thoracic surgery. 1989;48(1):1-2.

[32] Hill D, Duflou J, Delaney L. Blunt traumatic rupture of the thoracic aorta: an epidemiological perspective. Journal of the Royal College of Surgeons of Edinburgh. 1996;41(2):84-7.

[33] Burkhart HM, Gomez GA, Jacobson LE, Pless JE, Broadie TA. Fatal blunt aortic injuries: a review of 242 autopsy cases. The Journal of trauma. 2001;50(1):113-5.

[34] Teixeira PG, Inaba K, Barmparas G, Georgiou C, Toms C, Noguchi TT, et al. Blunt thoracic aortic injuries: an autopsy study. Journal of Trauma and Acute Care Surgery. 2011;70(1):197-202.

[35] McLellan BA, Rizoli SB, Brenneman FD, Boulanger BR, Sharkey PW, Szalai JP. Injury pattern and severity in lateral motor vehicle collisions: a Canadian experience. Journal of Trauma and Acute Care Surgery. 1996;41(4):708-13.

[36] Katyal D, McLellan BA, Brenneman FD, Boulanger BR, Sharkey PW, Waddell JP. Lateral impact motor vehicle collisions: significant cause of blunt traumatic rupture of the thoracic aorta. Journal of Trauma-Injury, Infection, and Critical Care. 1997;42(5):769-72.

[37] Horton TG, Cohn SM, Heid MP, Augenstein JS, Bowen JC, McKenney MG, et al. Identification of trauma patients at risk of thoracic aortic tear by mechanism of injury. Journal of Trauma and Acute Care Surgery. 2000;48(6):1008-14.

[38] Bertrand S, Cuny S, Petit P, Trosseille X, Page Y, Guillemot H, et al. Traumatic rupture of thoracic aorta in real-world motor vehicle crashes. Traffic injury prevention. 2008;9(2):153-61.

[39] Demetriades D, Velmahos GC, Scalea TM, Jurkovich GJ, Karmy-Jones R, Teixeira PG, et al. Operative repair or endovascular stent graft in blunt traumatic thoracic aortic injuries: results of an American Association for the Surgery of Trauma Multicenter Study. Journal of Trauma and Acute Care Surgery. 2008;64(3):561-71.

[40] Scalea T, Goldstein A, Phillips T, Sclafani S, Panetta T, McAuley J, et al. An analysis of 161 falls from a height: the'jumper syndrome'. Journal of Trauma and Acute Care Surgery. 1986;26(8):706-12.

[41] deGuzman BJ, Morgan AS, Pharr WF. Aortic transection following air-bag deployment. New England journal of medicine. 1997;337(8):573-4.

[42] OCHSNER JR MG, Champion HR, Chambers R, Harviel JD. Pelvic fracture as an indicator of increased risk of thoracic aortic rupture. Journal of Trauma and Acute Care Surgery. 1989;29(10):1376-9.

[43] Creasy JD, Chiles C, Routh WD, Dyer RB. Overview of traumatic injury of the thoracic aorta. Radiographics. 1997;17(1):27-45.

[44] Letterer E. Beiträge zur Entstehung der Aortenrupturen an typischer Stelle. Virchows Archiv. 1924;253(3):534-44.

[45] Hass GM. Types of internal injuries of personnel involved in aircraft accidents. J Aviat Med. 1944;15:77.

[46] Roberts V, Jackson F, Berkas E. Heart motion due to blunt trauma to the thorax. SAE Technical Paper, 1966 0148-7191.

[47] Stapp JP. Human tolerance to deceleration. The American Journal of Surgery. 1957;93(4):734-40.

[48] Melvin JW, Baron KJ, Little WC, Gideon TW, Pierce J. Biomechanical analysis of Indy race car crashes. SAE Technical Paper, 1998 0148-7191.

[49] Oppenheim F. Gibt es eine Spontanruptur der gesunden Aorta und wie kommt sie zustande. Münch med Wschr. 1918;65:1234-7.

[50] Klotz O, Simpson W. Spontaneous Rupture Op The Aorta. The American Journal of the Medical Sciences. 1932;184(4):455-72.

[51] Taylor ER. Thrombocytopenia following abrupt deceleration. Preliminary communication, 6571st Aeromedical Research Lab, Holloman AFB, New Mexico, Rept ARL-TDR. 1962:62-30.

[52] Shah CS, Hardy WN, Mason MJ, Yang KH. Dynamic biaxial tissue properties of the human cadaver aorta. Stapp car crash journal. 2006;50:217.

[53] Rindfleisch E. Zur entstehung und heilung des Aneurysma dissecans Aortae. Archiv für pathologische Anatomie und Physiologie und für klinische Medicin. 1893;131(2):374-8.

[54] Mohan D, Melvin JW. Failure properties of passive human aortic tissue. II--Biaxial tension tests. Journal of biomechanics. 1983;16(1):31-44.

[55] Shah CS. Investigation of traumatic rupture of the aorta (TRA) by obtaining aorta material and failure properties and simulating real-world aortic injury crashes using the whole-body finite element (FE) human model: ProQuest; 2007.

[56] Marshall T. Traumatic dissecting aneurysms. Journal of clinical pathology. 1958;11(1):36.

[57] Cammack K, Rapport RL, Paul J, Baird WC. Deceleration injuries of the thoracic aorta. AMA archives of surgery. 1959;79(2):244-51.

[58] Gotzen L, Flory P, Otte D. Biomechanics of aortic rupture at classical location in traffic accidents. The Thoracic and cardiovascular surgeon. 1980;28(01):64-8.

[59] Crass J, Cohen A, Motta A, Tomashefski Jr J, Wiesen E. A proposed new mechanism of traumatic aortic rupture: the osseous pinch. Radiology. 1990;176(3):645-9.

[60] Kirshner R, Seltzer S, D'Orsi C, DeWeese JA. Upper rib fractures and mediastinal widening: indications for aortography. The Annals of thoracic surgery. 1983;35(4):450-4.

[61] Sturm JT, Luxenberg MG, Moudry BM, Perry JF. Does sternal fracture increase the risk for aortic rupture? The Annals of thoracic surgery. 1989;48(5):697-8.

[62] Sevitt S. The mechanisms of traumatic rupture of the thoracic aorta. British Journal of Surgery. 1977;64(3):166-73.

[63] Coermann R, Dotzauer G, Lange W, Voigt G. The effects of the design of the steering assembly and the instrument panel on injuries (especially aortic rupture) sustained by car drivers in head-on collision. Journal of Trauma and Acute Care Surgery. 1972;12(8):715-24.

[64] Shatsky SA, Alter WA, Evans DE, Armbrustmacher VW, Earle KM, Clark G. Traumatic distortions of the primate head and chest: correlation of biomechanical, radiological and pathological data. SAE Technical Paper, 1974 0148-7191.

[65] Nusholtz GS, Kaiker PS, Bosio AC, Kirsh M. Thoracic Response to FrontalImpact. SAE Technical Paper, 1985 0148-7191.

[66] Cavanaugh JM, Walilko TJ, Malhotra A, Zhu Y, King AI. Biomechanical response and injury tolerance of the thorax in twelve sled side impacts. SAE Technical Paper, 1990 0148-7191.

[67] Cavanaugh JM, Zhu Y, Huang Y, King A. Injury and response of the thorax in side impact cadaveric tests. SAE Technical Paper, 1993 0148-7191.

[68] Cavanaugh JM, Koh S-W, Kaledhonkar SL, Hardy WN. An analysis of traumatic rupture of the aorta in side impact sled tests. SAE Technical Paper, 2005 0148-7191.

[69] Lau IV, Viano DC. The viscous criterion-bases and applications of an injury severity index for soft tissues. SAE Technical Paper, 1986 0148-7191.

[70] Shah CS, Yang KH, Hardy W, Wang HK, King AI. Development of a computer model to predict aortic rupture due to impact loading. Stapp car crash journal. 2001;45:161-82.

[71] Shah CS, Lee JB, Hardy WN, Yang KH, editors. A partially validated finite element whole-body human model for organ level injury prediction. Proceedings of the IMECE04 ASME International Mechanical Engineering Congress: IMECE; 2004.

[72] Shah CS, Maddali M, Mungikar SA, Beillas P, Hardy WN, Yang KH, et al. Analysis of a real-world crash using finite element modeling to examine traumatic rupture of the aorta. SAE Technical Paper, 2005 0148-7191.

[73] Mohan D, Melvin JW. Failure properties of passive human aortic tissue. I--uniaxial tension tests. Journal of biomechanics. 1982;15(11):887-902.

[74] García-Herrera CM, Celentano DJ, Cruchaga MA. Bending and pressurisation test of the human aortic arch: experiments, modelling and simulation of a patient-specific case. Computer methods in biomechanics and biomedical engineering. 2013;16(8):830-9.

[75] Han IS, Kim YE, Chae S-w. Effects of aging factors on thoracic injury risk under blunt impact loading. International Journal of Precision Engineering and Manufacturing. 2015;16(4):813-21.

[76] Howard DP, Sideso E, Handa A, Rothwell PM. Incidence, risk factors, outcome and projected future burden of acute aortic dissection. Annals of cardiothoracic surgery. 2014;3(3):278-84.

[77] Beller CJ, Labrosse MR, Thubrikar MJ, Robicsek F. Role of aortic root motion in the pathogenesis of aortic dissection. Circulation. 2004;109(6):763-9.

[78] Beller C, Labrosse M, Thubrikar M, Robicsek F. Finite element modeling of the thoracic aorta: including aortic root motion to evaluate the risk of aortic dissection. Journal of medical engineering & technology. 2008;32(2):167-70.

[79] Nathan DP, Xu C, Gorman JH, Fairman RM, Bavaria JE, Gorman RC, et al. Pathogenesis of acute aortic dissection: a finite element stress analysis. The Annals of thoracic surgery. 2011;91(2):458-63.

[80] Fillinger MF, Marra SP, Raghavan ML, Kennedy FE. Prediction of rupture risk in abdominal aortic aneurysm during observation: wall stress versus diameter. Journal of vascular surgery. 2003;37(4):724-32.

[81] Kozerke S, Scheidegger MB, Pedersen EM, Boesiger P. Heart motion adapted cine phase‐contrast flow measurements through the aortic valve. Magnetic resonance in medicine. 1999;42(5):970-8.

[82] Weber TF, Ganten M-K, Böckler D, Geisbüsch P, Kauczor H-U, von Tengg-Kobligk H. Heartbeat-related displacement of the thoracic aorta in patients with chronic aortic dissection type B: quantification by dynamic CTA. European journal of radiology. 2009;72(3):483-8.

[83] Rengier F, Weber TF, Henninger V, Böckler D, Schumacher H, Kauczor H-U, et al. Heartbeat-related distension and displacement of the thoracic aorta in healthy volunteers. European journal of radiology. 2012;81(1):158-64.

[84] Singh S, Xu X, Pepper J, Izgi C, Treasure T, Mohiaddin R. Effects of aortic root motion on wall stress in the Marfan aorta before and after personalised aortic root support (PEARS) surgery. Journal of biomechanics. 2016.

[85] Bal-Theoleyre L, Lalande A, Kober F, Giorgi R, Collart F, Piquet P, et al. Aortic Function's Adaptation in Response to Exercise-Induced Stress Assessing by 1.5 T MRI: A Pilot Study in Healthy Volunteers. PloS one. 2016;11(6):e0157704.

[86] Labrosse MR, Beller CJ, Mesana T, Veinot JP. Mechanical behavior of human aortas: Experiments, material constants and 3-D finite element modeling including residual stress. Journal of biomechanics. 2009;42(8):996-1004.

[87] Guccione JM, McCulloch AD, Waldman L. Passive material properties of intact ventricular myocardium determined from a cylindrical model. Journal of biomechanical engineering. 1991;113(1):42-55.

[88] Labrosse MR, Lobo K, Beller CJ. Structural analysis of the natural aortic valve in dynamics: from unpressurized to physiologically loaded. Journal of biomechanics. 2010;43(10):1916-22.

[89] Kim HJ, Vignon-Clementel IE, Figueroa CA, LaDisa JF, Jansen KE, Feinstein JA, et al. On coupling a lumped parameter heart model and a three-dimensional finite element aorta model. Annals of biomedical engineering. 2009;37(11):2153-69.

[90] Voges I, Jerosch-Herold M, Hedderich J, Pardun E, Hart C, Gabbert DD, et al. Normal values of aortic dimensions, distensibility, and pulse wave velocity in children and young adults: a cross-sectional study. Journal of Cardiovascular Magnetic Resonance. 2012;14(1):77.

[91] Weber TF, Müller T, Biesdorf A, Wörz S, Rengier F, Heye T, et al. True four-dimensional analysis of thoracic aortic displacement and distension using model-based

segmentation of computed tomography angiography. The international journal of cardiovascular imaging. 2014;30(1):185-94.

[92] Lin E, Alessio A. What are the basic concepts of temporal, contrast, and spatial resolution in cardiac CT? Journal of cardiovascular computed tomography. 2009;3(6):403-8.

[93] Redheuil A, Yu W-C, Wu CO, Mousseaux E, de Cesare A, Yan R, et al. Reduced ascending aortic strain and distensibility. Hypertension. 2010;55(2):319-26.

[94] Mensel B, Kühn J-P, Schneider T, Quadrat A, Hegenscheid K. Mean thoracic aortic wall thickness determination by cine MRI with steady-state free precession: validation with dark blood imaging. Academic radiology. 2013;20(8):1004-8.

[95] Dua MM, Dalman RL. Hemodynamic influences on abdominal aortic aneurysm disease: Application of biomechanics to aneurysm pathophysiology. Vascular pharmacology. 2010;53(1):11-21.

[96] Papaioannou TG, Karatzis EN, Vavuranakis M, Lekakis JP, Stefanadis C. Assessment of vascular wall shear stress and implications for atherosclerotic disease. International journal of cardiology. 2006;113(1):12-8.

[97] Bäck M, Gasser TC, Michel J-B, Caligiuri G. Biomechanical factors in the biology of aortic wall and aortic valve diseases. Cardiovascular research. 2013;99(2):232-41.

[98] García-Herrera CM, Celentano DJ. Modelling and numerical simulation of the human aortic arch under in vivo conditions. Biomechanics and modeling in mechanobiology. 2013;12(6):1143-54.

[99] Azadani AN, Chitsaz S, Mannion A, Mookhoek A, Wisneski A, Guccione JM, et al. Biomechanical properties of human ascending thoracic aortic aneurysms. The Annals of thoracic surgery. 2013;96(1):50-8.

[100] Vorp DA, Schiro BJ, Ehrlich MP, Juvonen TS, Ergin MA, Griffith BP. Effect of aneurysm on the tensile strength and biomechanical behavior of the ascending thoracic aorta. The Annals of thoracic surgery. 2003;75(4):1210-4.

[101] Kermani G, Assari S, Hemmasizadeh A, Darvish K. Characterizing the Inhomogeneity of Aorta Mechanical Properties and its Effect on the Prediction of Injury. 2015 Ohio State University Injury Biomechanics Symposium. 2015.

[102] Richens D, Field M, Neale M, Oakley C. The mechanism of injury in blunt traumatic rupture of the aorta. European Journal of Cardio-Thoracic Surgery. 2002;21(2):288-93.

[103] Arthurs ZM, Starnes BW, Sohn VY, Singh N, Martin MJ, Andersen CA. Functional and survival outcomes in traumatic blunt thoracic aortic injuries: an analysis of the National Trauma Databank. Journal of vascular surgery. 2009;49(4):988-94.

[104] Kenny D, Hijazi ZM. Coarctation of the aorta: from fetal life to adulthood. Cardiology journal. 2011;18(5):487-95.

[105] Ungar TC, Wolf SJ, Haukoos JS, Dyer DS, Moore EE. Derivation of a clinical decision rule to exclude thoracic aortic imaging in patients with blunt chest trauma after motor vehicle collisions. Journal of Trauma and Acute Care Surgery. 2006;61(5):1150-5.

[106] Otte D, Facius T, Klintschar M, Brand S, editors. Investigations and Injury Mechanisms of Aortic Ruptures among Vehicle Occupants and Vulnerable Road Users over Time. IRCOBI Conference Proceedings; 2016.

[107] Pongratz J, Ockert S, Reeps C, Eckstein H. Traumatic rupture of the aorta: origin, diagnosis, and therapy of a life-threatening aortic injury. Der Unfallchirurg. 2011;114(12):1105-12; quiz 13-4.

[108] Richens D, Kotidis K, Neale M, Oakley C, Fails A. Rupture of the aorta following road traffic accidents in the United Kingdom 1992–1999. The results of the co-operative crash injury study. European journal of cardio-thoracic surgery. 2003;23(2):143-8.

[109] Estrera AL, Miller CC, Guajardo-Salinas G, Coogan S, Charlton-Ouw K, Safi HJ, et al. Update on blunt thoracic aortic injury: fifteen-year single-institution experience. The Journal of thoracic and cardiovascular surgery. 2013;145(3):S154-S8.

[110] Stemper BD, Yoganandan N, Pintar FA, Brasel KJ. Multiple subfailures characterize blunt aortic injury. Journal of Trauma and Acute Care Surgery. 2007;62(5):1171-4.

[111] Schmoker JD, Lee CH, Taylor RG, Chung A, Trombley L, Hardin N, et al. A novel model of blunt thoracic aortic injury: a mechanism confirmed? Journal of Trauma and Acute Care Surgery. 2008;64(4):923-31.

[112] White N, Shah C, Hardy W, editors. Mechanisms of traumatic rupture of the aorta: recent multi-scale investigations. 26th Southern Biomedical Engineering Conference SBEC 2010, April 30-May 2, 2010, College Park, Maryland, USA; 2010: Springer.

[113] Pearson R, Philips N, Hancock R, Hashim S, Field M, Richens D, et al. Regional wall mechanics and blunt traumatic aortic rupture at the isthmus. European journal of cardio-thoracic surgery. 2008;34(3):616-22.

[114] Lessley D, Crandall J, Shaw G, Kent R, Funk J. A normalization technique for developing corridors from individual subject responses. SAE Technical Paper, 2004 0148-7191.

[115] Mohan D, Melvin JW. Failure properties of passive human aortic tissue. I—uniaxial tension tests. Journal of biomechanics. 1982;15(11):887-93.

[116] Bourgouin S, Bège T, Masson C, Arnoux P-J, Mancini J, Garcia S, et al. Biomechanical characterisation of fresh and cadaverous human small intestine: applications for abdominal trauma. Medical & biological engineering & computing. 2012;50(12):1279-88.

[117] Fitzharris M, Franklyn M, Frampton R, Yang K, Morris A, Fildes B. Thoracic aortic injury in motor vehicle crashes: the effect of impact direction, side of body struck, and seat belt use. Journal of Trauma and Acute Care Surgery. 2004;57(3):582-90.

[118] Kurland G, Orenstein DM. Complications of pediatric lung and heart-lung transplantation. Current opinion in pediatrics. 1994;6(3):262-71.

[119] Pellicer J, Garcia-Morales V, Hernández M. On the demonstration of the Young-Laplace equation in introductory physics courses. Physics Education. 2000;35(2):126.

[120] Standard S A E. J224[J]. Collision Deformation Classification, 1980.

[121] Yu M. Finite element analysis of passenger multiple belt restraint configurations. Diss., Wake Forest University; 2010.

[122] Li K, Wang Q, Pham T, Sun W. Quantification of structural compliance of aged human and porcine aortic root tissues. Journal of Biomedical Materials Research Part A. 2014;102(7):2365-74.

[123] Shkrum MJ, McClafferty KJ, Green RN, Nowak ES, Young JG. Mechanisms of aortic injury in fatalities occurring in motor vehicle collisions. Journal of Forensic Science. 1999;44(1):44-56.

[124] Jeremy RW, Huang H, Hwa J, McCarron H, Hughes CF, Richards JG. Relation between age, arterial distensibility, and aortic dilatation in the Marfan syndrome. The American journal of cardiology. 1994;74(4):369-73.

[125] O'rourke MF, Nichols WW. Aortic diameter, aortic stiffness, and wave reflection increase with age and isolated systolic hypertension. Hypertension. 2005;45(4):652-8.

[126] Siegel JH, Smith JA, Siddiqi SQ. Change in velocity and energy dissipation on impact in motor vehicle crashes as a function of the direction of crash: key factors in the production of thoracic aortic injuries, their pattern of associated injuries and patient survival a Crash Injury Research Engineering Network (CIREN) study. Journal of Trauma-Injury, Infection, and Critical Care. 2004;57(4):760-78.

[127] Yuen K, Cronin DS, Deng Y, editors. Lung response and injury in side impact conditions. Proceedings of the 2008 International Research Council on Biomechanics of Injury (IRCOBI) Conference; 2008.

[128] Gayzik FS. Development of a finite element based injury metric for pulmonary contusion Ph.D. Diss., Virginia Tech, 2008.

[129] Lundevall J. The mechanism of traumatic rupture of the aorta. APMIS. 1964;62(1):34-46.

[130] Thorley A. Fluid transients in pipeline systems–a guide to the control and suppression of fluids transients in liquids in closed conduits. Professional Engineering Publishing Limited, United Kingdom. 2004.

[131] Hallquist JO. LS-DYNA® Keyword User's Manual: Volumes I, II, and III LSDYNA R7. 1. Livermore Software Technology Corporation, Livermore (LSTC), Livermore, California. 2014;1265.

[132] Feng J, An M, Sashikumar S, Chen W. 3D computational fluid dynamic modelling for pulsatile blood wave propagation in the event of car crash. International Journal of Crashworthiness. 2017;22(4):394-400.

[133] Vavalle NA, Davis ML, Stitzel JD, Gayzik FS. Quantitative validation of a human body finite element model using rigid body impacts. Annals of biomedical engineering. 2015;43(9):2163-74.

[134] STL database available at: http://www.stlfinder.com/model/human-heart-7.

[135] Isnard RN, Pannier BM, Laurent S, London GM, Diebold B, Safar ME. Pulsatile diameter and elastic modulus of the aortic arch in essential hypertension: a noninvasive study. Journal of the American College of Cardiology. 1989;13(2):399-405.

[136] Nevsky G, Jacobs JE, Lim RP, Donnino R, Babb JS, Srichai MB. Sex-specific normalized reference values of heart and great vessel dimensions in cardiac CT angiography. American Journal of Roentgenology. 2011;196(4):788-94.

[137] Maceira A, Prasad S, Khan M, Pennell D. Normalized left ventricular systolic and diastolic function by steady state free precession cardiovascular magnetic resonance. Journal of Cardiovascular Magnetic Resonance. 2006;8(3):417-26.

[138] Drake R, Vogl AW, Mitchell AW. Gray's anatomy for students*,* 3rd ed., Churchill Elsevier, Philadelphia, 2014.

[139] Konings MK, Goovaerts HG, Roosendaal MR, Rienks R, Koevoets FM, Bleys RL, et al. A new electric method for non-invasive continuous monitoring of stroke volume and ventricular volume-time curves. Biomedical engineering online. 2012;11(1): 51-80.

[140] Moosavi M-H, Fatouraee N, Katoozian H, Pashaei A, Camara O, Frangi AF. Numerical simulation of blood flow in the left ventricle and aortic sinus using magnetic resonance imaging and computational fluid dynamics. Computer methods in biomechanics and biomedical engineering. 2014;17(7):740-9.

[141] Watanabe H, Sugiura S, Kafuku H, Hisada T. Multiphysics simulation of left ventricular filling dynamics using fluid-structure interaction finite element method. Biophysical journal. 2004;87(3):2074-85.

[142] Vavalle NA, Moreno DP, Rhyne AC, Stitzel JD, Gayzik FS. Lateral impact validation of a geometrically accurate full body finite element model for blunt injury prediction. Annals of biomedical engineering. 2013;41(3):497-512.

[143] Lau K, Diaz V, Scambler P, Burriesci G. Mitral valve dynamics in structural and fluid–structure interaction models. Medical engineering & physics. 2010;32(9):1057-64.

[144] Schlosser T, Pagonidis K, Herborn CU, Hunold P, Waltering K-U, Lauenstein TC, et al. Assessment of left ventricular parameters using 16-MDCT and new software for endocardial and epicardial border delineation. American Journal of Roentgenology. 2005;184(3):765-73.

[145] Nobari S, Mongrain R, Leask R, Cartier R. The effect of aortic wall and aortic leaflet stiffening on coronary hemodynamic: a fluid–structure interaction study. Medical & biological engineering & computing. 2013;51(8):923-36.

[146] Nichols W, O'Rourke M, Vlachopoulos C. McDonald's blood flow in arteries: theoretical, experimental and clinical principles: 6th ed. Hodder Arnold, London, 2011.

[147] Bürk J, Blanke P, Stankovic Z, Barker A, Russe M, Geiger J, et al. Evaluation of 3D blood flow patterns and wall shear stress in the normal and dilated thoracic aorta using flow-sensitive 4D CMR. Journal of Cardiovascular Magnetic Resonance. 2012;14(1):1-11.

[148] Stalder A, Russe M, Frydrychowicz A, Bock J, Hennig J, Markl M. Quantitative 2D and 3D phase contrast MRI: optimized analysis of blood flow and vessel wall parameters. Magnetic resonance in medicine. 2008;60(5):1218-31.

[149] Gaur P, Chawla A, Verma K, Mukherjee S, Lalvani S, Malhotra R, et al. Characterisation of human diaphragm at high strain rate loading. Journal of the mechanical behavior of biomedical materials. 2016;60:603-16.

[150] Haug E, Choi H-Y, Robin S, Beaugonin M. Human models for crash and impact simulation. Handbook of Numerical Analysis. 2004;12:231-452.

[151] Ruan J, El-Jawahri R, Li C, Barbat S, Prasad P. Prediction and analysis of human thoracic impact responses and injuries in cadaver impacts using a full human body finite element model. Stapp car crash journal. 2003;47:299.

[152] Vezin P, Verriest JP, editors. Development of a set of numerical human models for safety. 19th International Technical Conference on the Enhanced Safety of Vehicles, Washington DC; 2005: Citeseer.

[153] Iwamoto M, Kisanuki Y, Watanabe I, Furusu K, Miki K, Hasegawa J. Development of a finite element model of the total human model for safety (THUMS) and application to injury reconstruction. Proceedings of the 2002 International Research Council on Biomechanics of Injury, Munich, Germany. 2002:31-42.

[154] Gayzik FS, Moreno DP, Vavalle NA, Rhyne AC, Stitzel JD, editors. Development of a full human body finite element model for blunt injury prediction utilizing a multi-modality medical imaging protocol. 12th International LS-DYNA User Conference, Dearborn, MI; 2012.

[155] Gayzik FS, Moreno DP, Vavalle NA, Rhyne AC, Stitzel JD, editors. Development of the global human body models consortium mid-sized male full body model. International Workshop on Human Subjects for Biomechanical Research; 2011.

[156] Mao H, Zhang L, Jiang B, Genthikatti VV, Jin X, Zhu F, et al. Development of a finite element human head model partially validated with thirty five experimental cases. Journal of biomechanical engineering. 2013;135(11):111002.

[157] DeWit JA, Cronin DS. Cervical spine segment finite element model for traumatic injury prediction. Journal of the mechanical behavior of biomedical materials. 2012;10:138-50.

[158] Panzer MB, Cronin DS. C4-C5 segment finite element model development, validation, and load-sharing investigation. Journal of biomechanics. 2009;42(4):480-90.

[159] Fice JB, Cronin DS, Panzer MB. Cervical spine model to predict capsular ligament response in rear impact. Annals of biomedical engineering. 2011;39(8):2152-62.

[160] Li Z, Kindig MW, Kerrigan JR, Untaroiu CD, Subit D, Crandall JR, et al. Rib fractures under anterior–posterior dynamic loads: experimental and finite-element study. Journal of biomechanics. 2010;43(2):228-34.

[161] Li Z, Kindig MW, Subit D, Kent RW. Influence of mesh density, cortical thickness and material properties on human rib fracture prediction. Medical engineering & physics. 2010;32(9):998-1008.

[162] Beillas P, Berthet F. Performance of a 50th percentile abdominal model for impact: effects of size and mass. Journal of biomechanics. 2012;45:S83.

[163] Shin J, Yue N, Untaroiu CD. A finite element model of the foot and ankle for automotive impact applications. Annals of biomedical engineering. 2012;40(12):2519-31.

[164] Untaroiu CD, Yue N, Shin J. A finite element model of the lower limb for simulating automotive impacts. Annals of biomedical engineering. 2013;41(3):513-26.

[165] Hayes AR, Vavalle NA, Moreno DP, Stitzel JD, Gayzik FS. Validation of simulated chestband data in frontal and lateral loading using a human body finite element model. Traffic injury prevention. 2014;15(2):181-6.

APPENDIX A STRESS DISTRIBUTION OF STRUCTURAL AND FSI SIMULATIONS

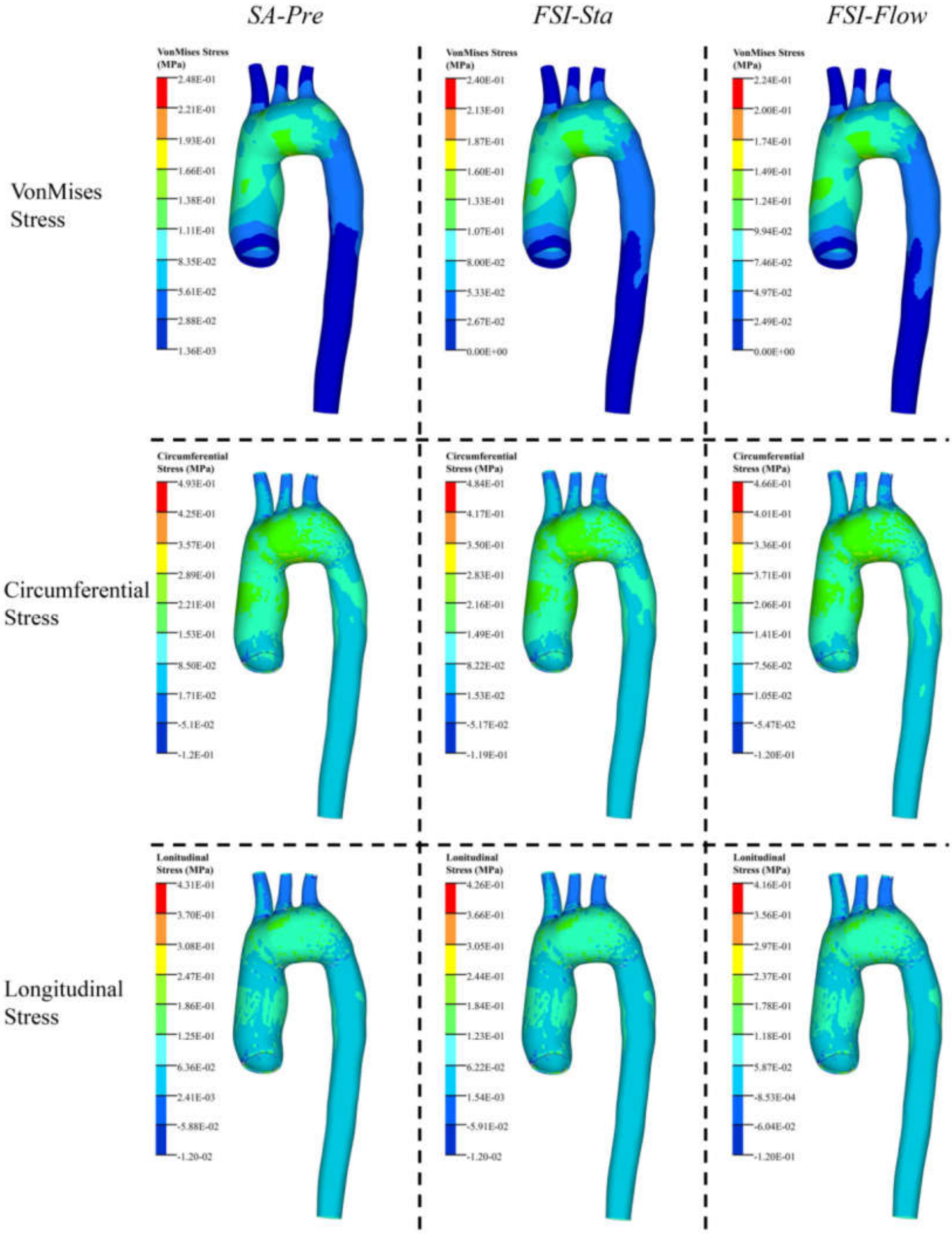
SA-Pre
FSI-Sta
FSI-Flow
VonMises Stress
VonMises Stress (MPa)
2.48E-01
2.21E-01
1.93E-01
1.66E-01
1.38E-01
1.11E-01
8.35E-02
5.61E-02
2.88E-02
1.36E-03
VonMises Stress (MPa)
2.40E-01
2.13E-01
1.87E-01
1.60E-01
1.33E-01
1.07E-01
8.00E-02
5.33E-02
2.67E-02
0.00E+00
VonMises Stress (MPa)
2.24E-01
2.00E-01
1.74E-01
1.49E-01
1.24E-01
9.94E-02
7.46E-02
4.97E-02
2.49E-02
0.00E+00
Circumferential Stress
Circumferential Stress (MPa)
4.93E-01
4.25E-01
3.57E-01
2.89E-01
2.21E-01
1.53E-01
8.50E-02
1.71E-02
-5.1E-02
-1.2E-01
Circumferential Stress (MPa)
4.84E-01
4.17E-01
3.50E-01
2.83E-01
2.16E-01
1.49E-01
8.22E-02
1.53E-02
-5.17E-02
-1.19E-01
Circumferential Stress (MPa)
4.66E-01
4.01E-01
3.36E-01
3.71E-01
2.06E-01
1.41E-01
7.56E-02
1.05E-02
-5.47E-02
-1.20E-01
Longitudinal Stress
Lonitudinal Stress (MPa)
4.31E-01
3.70E-01
3.08E-01
2.47E-01
1.86E-01
1.25E-01
6.36E-02
2.41E-03
-5.88E-02
-1.20-02
Lonitudinal Stress (MPa)
4.26E-01
3.66E-01
3.05E-01
2.44E-01
1.84E-01
1.23E-01
6.22E-02
1.54E-03
-5.91E-02
-1.20-02
Lonitudinal Stress (MPa)
4.16E-01
3.56E-01
2.97E-01
2.37E-01
1.78E-01
1.18E-01
5.87E-02
-8.53E-04
-6.04E-02
-1.20E-01

Figure A1. VonMises, circumferential and longitudinal stress distribution of the control model and FSI simulations

APPENDIX B BLOOD VELOCITY PROFILE AND WSS AT AA, PDA AND DDA

The blood velocity of each node at different aortic sections (AA, PDA and DDA) was exported from the simulation. With the fitting tools of MATLAB R2013a (The Mathworks, Natick, MA, USA), the cubic spline interpolation was used to fit the blood flow profile at each section (Figure B1). WSS corresponds to the friction force from the flowing blood at the vessel wall and depends on the spatial velocity gradient at the wall. It can be computed with the simplified equation (B1):

$$\mathrm{WSS} = \mu \left(\frac{\delta u}{\delta x}\right)_{x=0} \qquad \text{(B1)}$$

where μ is the blood dynamic viscosity, u the blood flow velocity along the lumen direction and x the distance from the wall along its inward normal direction. In Figure B2 was displayed the WSS distribution at AA, PDA and DDA.

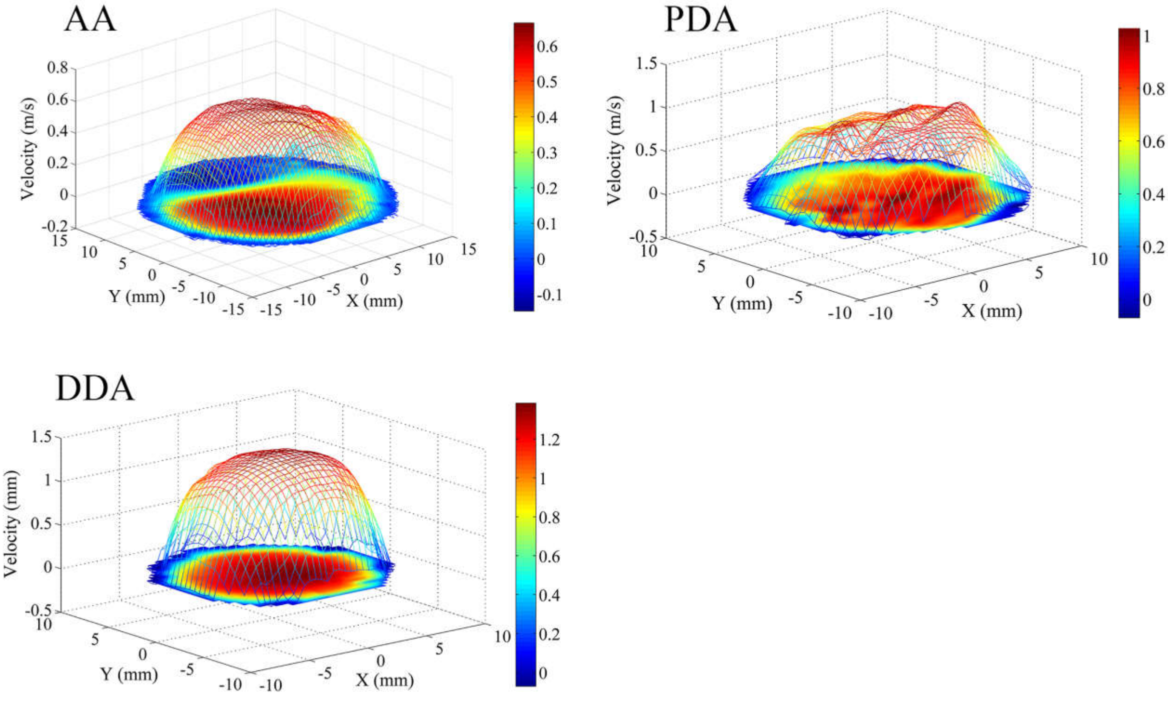

Figure B1. Blood velocity profile at AA, PDA and DDA

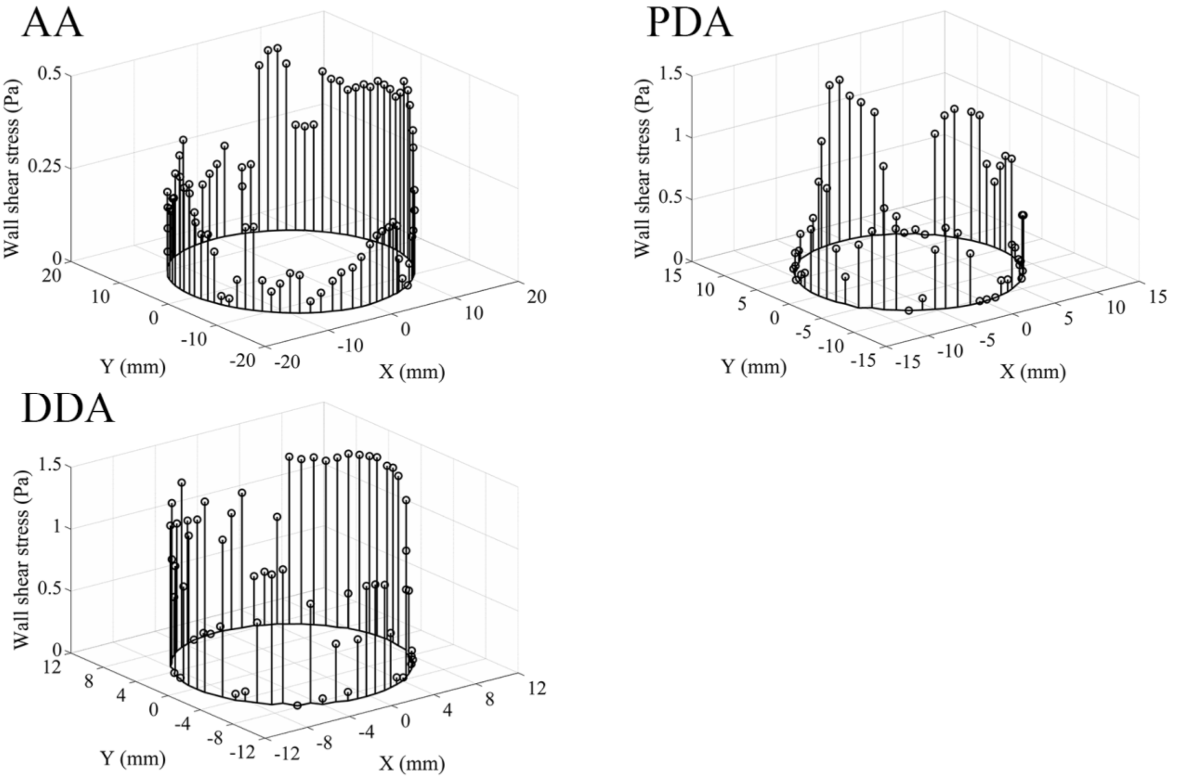
AA
PDA
DDA

Figure B2. Wall shear stress distribution at AA, PDA and DDA

APPENDIX C ELEMENT AXIS ORIENTATION

In order to obtain the circumferential and longitudinal stress of the aortic wall, the element axis was firstly oriented during mesh construction process. In LS-Prepost, the 'direction' function in 'element editing' submenu was used to orient the axis of the selected aortic shell elements along lumen longitudinal direction (Fig. C. 1). The aortic shell elements were subsequently offset with an uniform 2mm thickness to generate the brick elements, the axis of which would also be consistently oriented. During post-processing, the aortic wall stress could be displayed according to element coordinate system, where the XX (Fig. C. 2) component corresponded to the circumferential stress and YY component (Fig. C. 3) to the longitudinal stress.

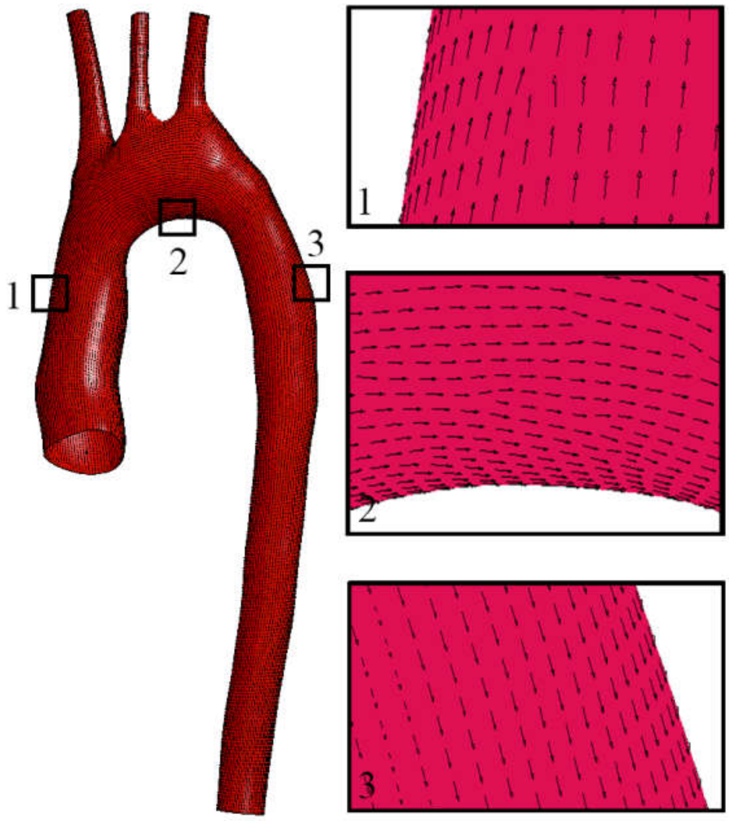

Figure C1. Element axis of 2D aortic shell elements

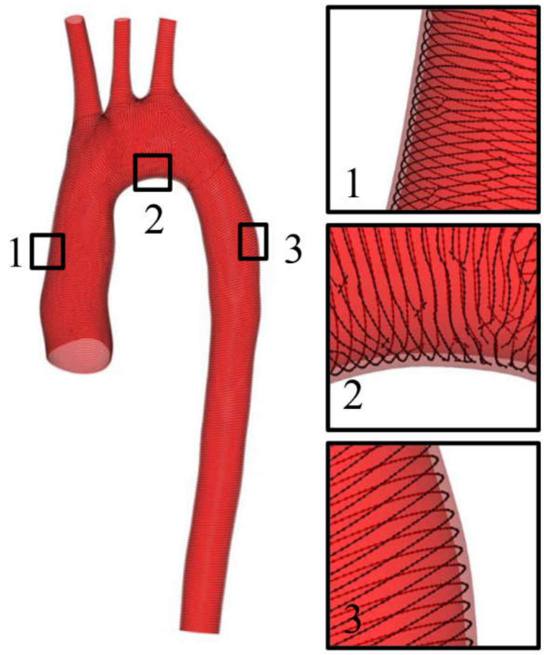

Figure C2. Circumferential stress distribution on 3D aortic wall

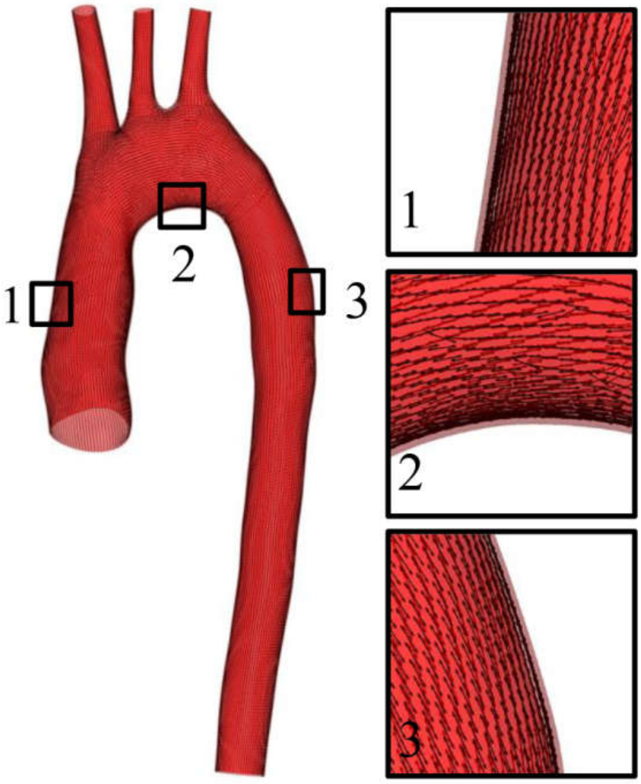

Figure C3. Longitudinal stress distribution on 3D aortic wall

APPENDIX D PARAMETRIC COMPARISON BETWEEN CASE DESCRIPTIONS AND FE MODELS FOR RECONSTRUCTION

Table D1. Comparison between the victim and GHBMC M50 model in terms of gender, age, height and weight

	Gender	Age (Years)	Height (cm)	Weight (kg)	Injury Descriptions
Victim	Male	36	173	64	Aortic arch transection/rupture, lung contusion/laceration, Bilateral rib fractures, Skin contusion, etc.
Model	Male	26	174.9	78.6	--

Table D2. Comparison between the case vehicle and the FE model in terms of size and weight

	Weight (kg)	Width (mm)	Height (mm)	Wheel Base (mm)	Length (mm)
Case Vehicle (2004 Honda Civic)	1117+182*	1720	1420	2620	4440
FE Model (1996 Dodge Neon)	1324	1715	1350	2642	4336
Difference (%)	1.9	-2.4	1.5	2.7	-1.4

*A total mass of 182kg for 3 occupants in the car

APPENDIX E MINI-SLED ACCELERATIONS

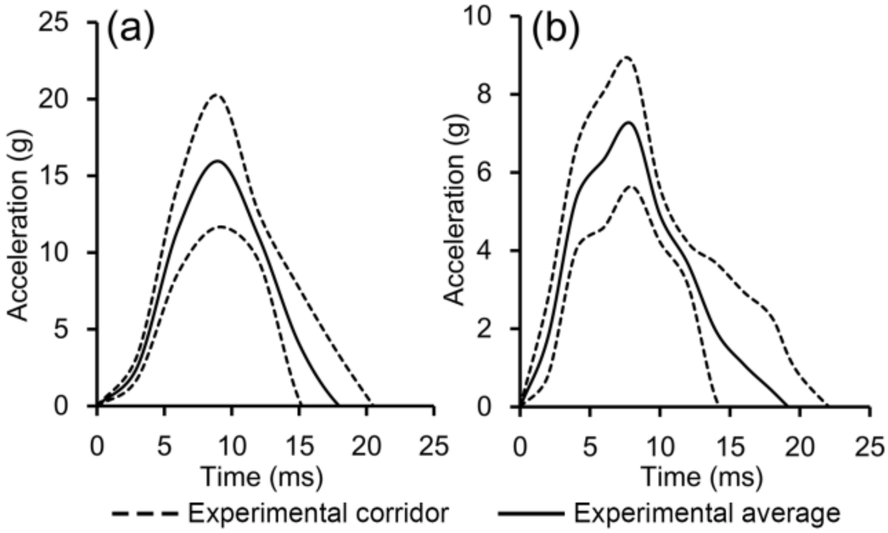

Figure E1. Mean accelerations of mini-sled along with the experimental corridors recorded in *Impact-20°* (a) and *Impact-10°* (b)

APPENDIX F AORTIC DEFLECTION IN MINI-SLED TESTS

The *xy* coordinate system (see Figure F1) was fixed on the sled to measure the aortic arch location relative to the sled. The aortic arch *deflection* was evaluated with the initial coordinates (x_0,y_0) of the superior aortic arch at t=0ms and the coordinates (x,y) at each moment relative to the coordinate system fixed on the sled (see Figure F1). Since the sled was only allowed to travel in *x* direction, the aortic arch deflection was only considered for its projection on the *x* axis and measured as x-x_0.

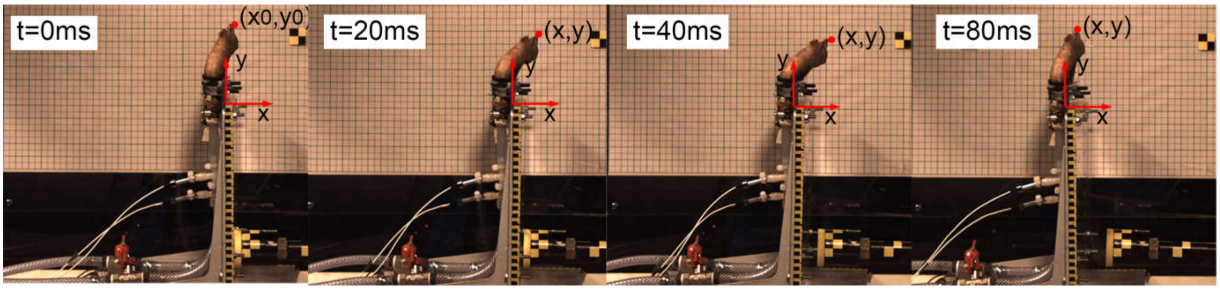

Figure F1. High-speed photos of Aorta-3 under 50mmHg pressurization in *Impact-20°* to capture aortic arch deflections at four different experimental moments: the beginning of pendulum-sled impact (t=0ms), the aortic bending (t=20ms), the peak aortic deflection (t=40ms) and the aortic rebound (t=80ms)

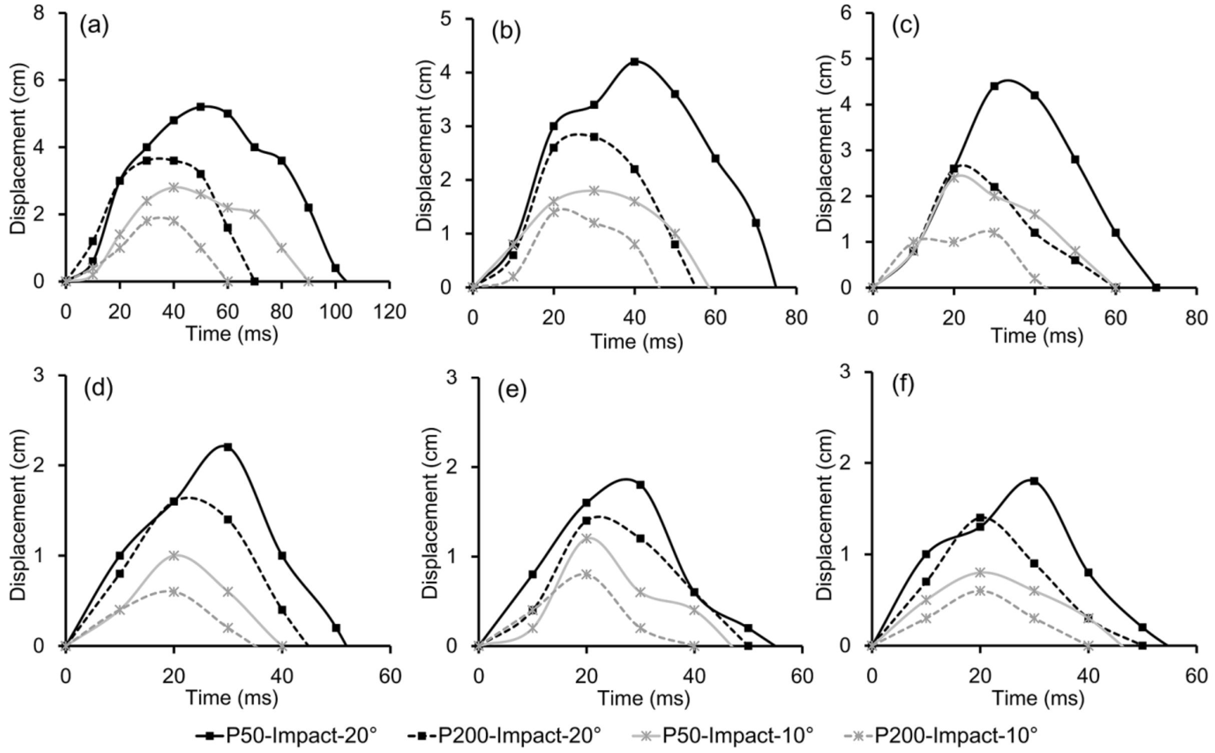

Figure F2. Aortic deflection versus time of all the aortas except aorta 3: Aorta-1 (a), Aorta-2 (b), Aorta-4 (c), Aorta-5 (d), where P50 and P200 correspond to pressure 50mmHg ad 200mmHg

APPENDIX G OBLIQUE-FRONTAL CRASH RECONSTRUCTION

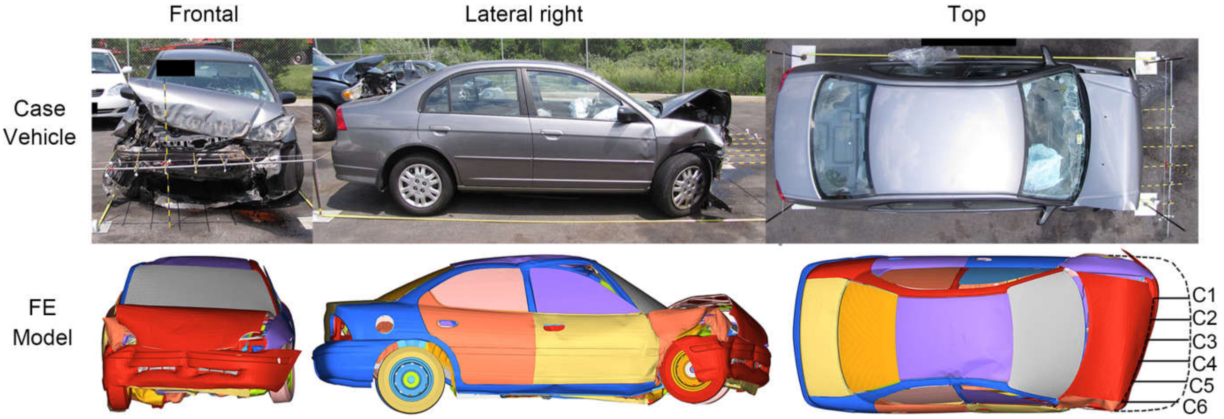
Frontal
Lateral right
Top
Case Vehicle
FE Model
C1
C2
C3
C4
C5
C6

[redacted] [redacted]

Figure G1. Crush profiles of the oblique-frontal crash reconstruction compared with the case vehicle deformations

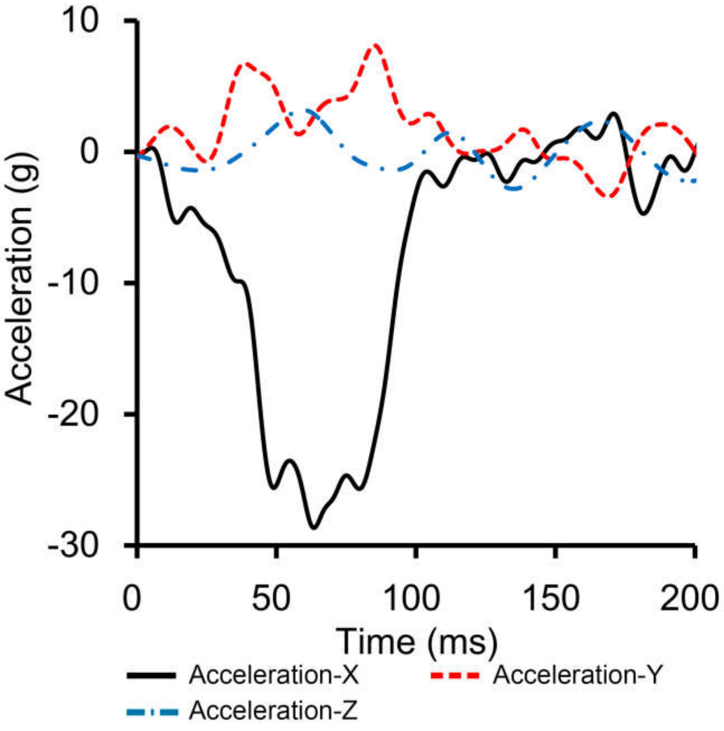

Figure G2. Acceleration time-histories acquired in stage 1 and input for stage 2

APPENDIX H THE EQUATION OF STATE (EOS) FOR BLOOD AND THE RELATIVE VOLUME TIME-HISTORY FOR FLUID OUTFLOW

The EOS is a thermodynamic equation which provides a mathematical relationship between two or more state variables (for example: temperature, pressure) associated with a material. The EOS is often used to correlate densities of materials to temperatures and pressures especially in the situations when the material is subjected to very high strain rates and when the material pressures are much higher than yield stress. In this study, the linear Gruneisen EOS was used to describe the relation between blood pressure and density, which could be computed with the simplified equation (H1):

$$p = (\rho - \rho_0) \cdot C^2 \qquad \text{(H1)}$$

where p is the blood pressure; ρ and ρ_0 correspond to the current and initial blood densities; C is the speed of sound propagating through the blood. C could also be calculated by the Newton-Laplace equation (H2):

$$C = \sqrt{\frac{K}{\rho}} \qquad \text{H2)}$$

where K is the blood bulk modulus and ρ was assumed to be equal to initial density for simplifying the sound speed calculation. The sound speed passing through blood was determined to be 1543.0m/s.

In order to reproduce realistic fluid outflow, a physiological time-independent pressure [89] was correspondingly applied to outlet 1 and 2 (cf. Figure 5.7). Since it is impossible to prescribe pressure to Eulerian meshes directly in LS-DYNA, the fluid relative volume time-history was converted based on the equation (H3):

$$v_r = \frac{v}{v_0} = \frac{\rho_0}{\rho} = \frac{\rho_0 \cdot C^2}{p + \rho_0 \cdot C^2} \qquad \text{(H3)}$$

where v_0, v and v_r correspond to initial, current and relative blood volume. The time-history of outlet relative volume was displayed in Figure H1.

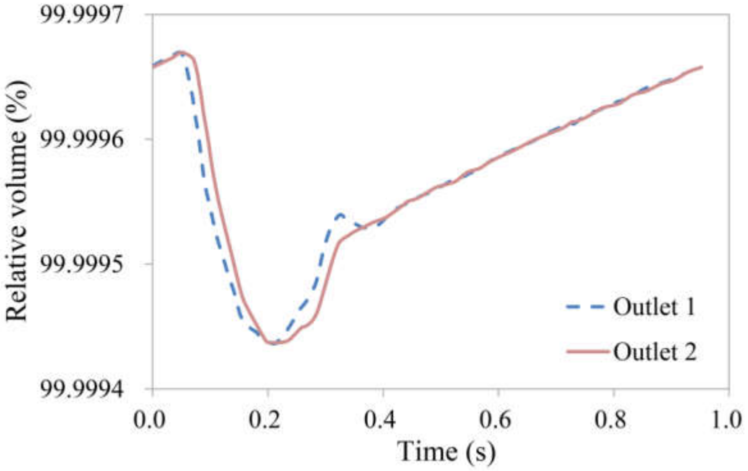

Figure H1. Time-history of blood relative volume to prescribe physiological outflow at outlet 1 and 2

APPENDIX I PARAMETRIC COMPARISON BETWEEN CASE DESCRIPTIONS AND NUMERICAL RECONSTRUCTION

Table I1. Comparison between the victim and GHBMC M50 model in terms of gender, age, height and weight

	Gender	Age (Years)	Height (cm)	Weight (kg)	Injury Descriptions
Victim	Male	65	181	101	Aortic isthmus transverse laceration, bilateral rib fractures, diaphragm laceration, etc.
Model	Male	26	174.9	78.6	--

Table I2. Comparison between the case vehicle and the FE model in terms of size and weight

	Weight (kg)	Width (mm)	Height (mm)	Wheel Base (mm)	Length (mm)
Case Vehicle (1994 Honda Accord)	1295	1781	1420	2715	4770
FE Model (2012 Toyota Camry)	1145	1823	1442	2789	4835
Difference (%)	-10.3	2.4	1.5	2.7	1.4

APPENDIX J BLOOD PRESSURE TIME-HISTORY IN THE ASCENDING AORTA AND DESCENDING AORTA

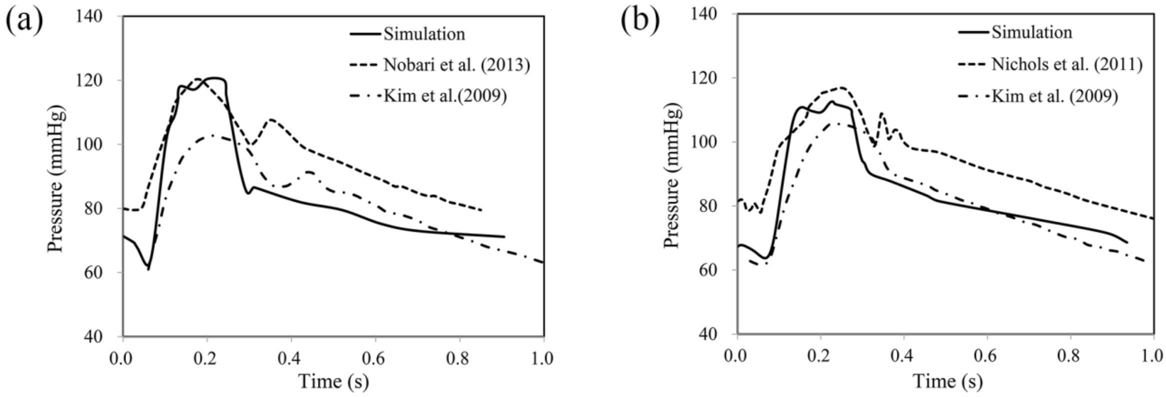

Figure J1. The time-history of blood pressure in the ascending aorta (A) and the descending aorta (B)

APPENDIX K TIME-HISTORY OF SECTION-AVERAGED BLOOD VELOCITY FOR SECTION 3, 4, 6 AND 8

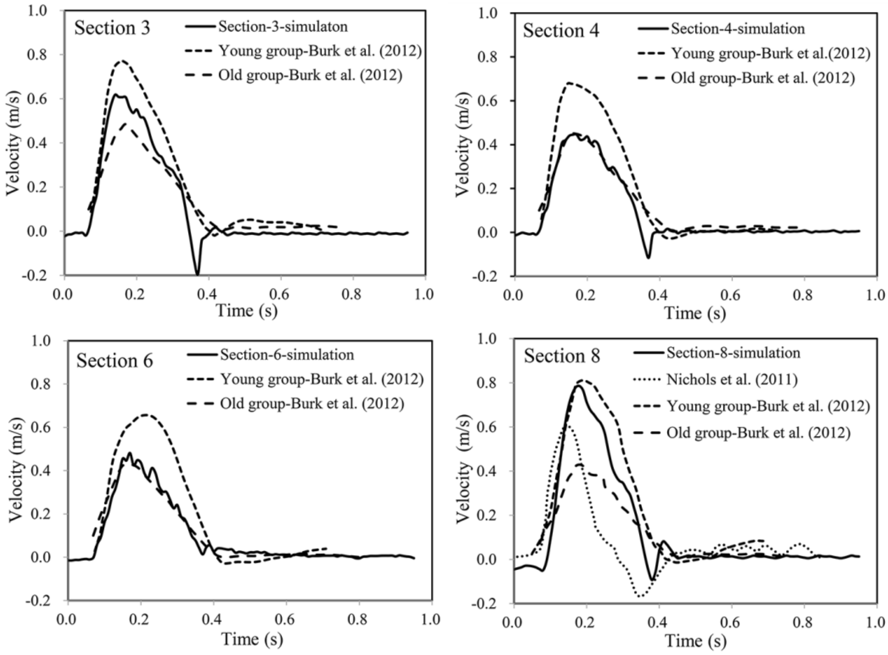

Figure K1. Time-history of section-averaged blood velocity for section 3, 4, 6 and 8

APPENDIX L TIME-HISTORY OF BLOOD FLOW RATE FOR SECTION 3, 6 AND 8

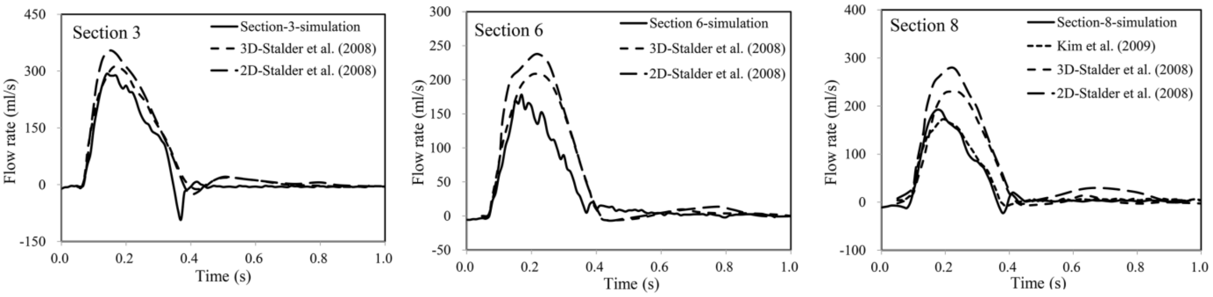

Figure L1. Time-history of blood flow rate for section 3, 6 and 8

APPENDIX M SECTION-AVERAGED WSS EVALUATION

WSS corresponds to the friction force from the flowing blood at the vessel wall and is an index suggested to affect the function of endothelial cells and the development of some vascular diseases. WSS depends on the spatial velocity gradient at the wall and can be computed with the simplified equation (M1):

$$WSS = \mu \left(\frac{\delta u}{\delta x}\right)_{x=0} \qquad \text{(M1)}$$

where μ is the blood dynamic viscosity, u the blood flow velocity along the lumen direction and x the distance from the wall along its inward normal direction.

In this study, the flow on the vessel wall was assumed to be zero and the blood velocity at each node on each section was extracted and projected along the aortic longitudinal direction. With the fitting tools of MATLAB (The Mathworks, Natick, MA, USA), the cubic interpolation was chosen to compute the blood axial flow velocity close enough to the vessel. Consequently, WSS on each point of the aortic section could be computed based on equation (M1). The section-averaged WSS (Figure M1) was calculated as the mean value of the WSS distribution on each section during the whole cardiac cycle.

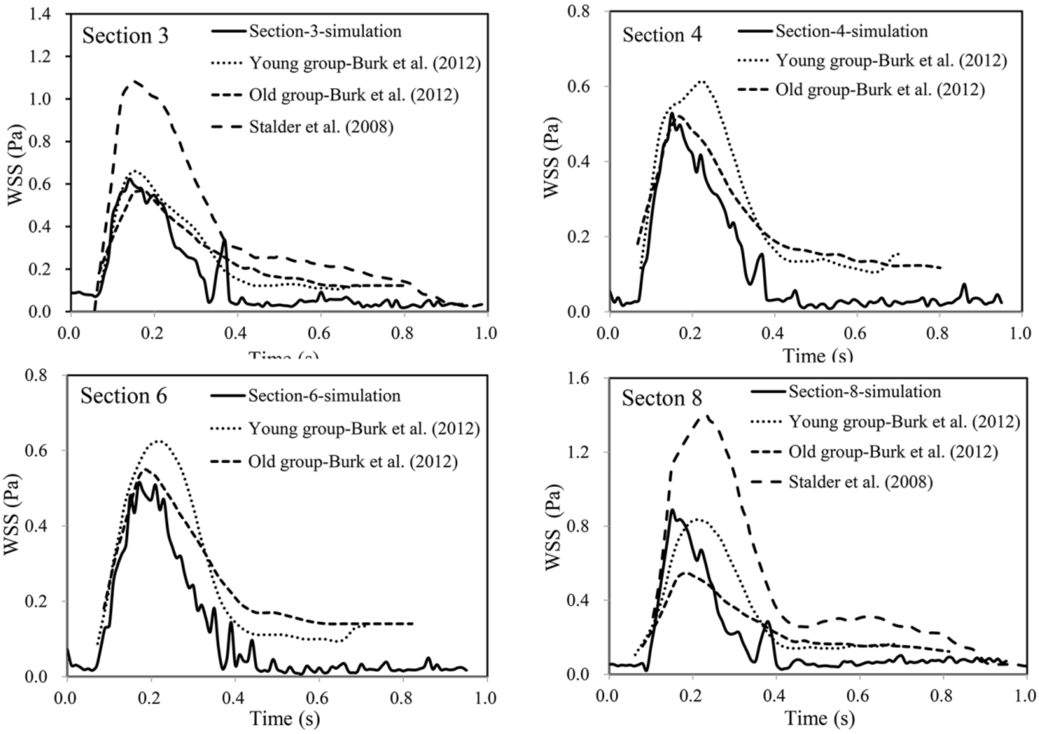

Figure M1. Time-history of section-averaged WSS for section 3, 4, 6 and 8

APPENDIX N DEFORMATION PATTERNS OF NUMERICAL RECONSTRUCTION AND CASE VEHICLE

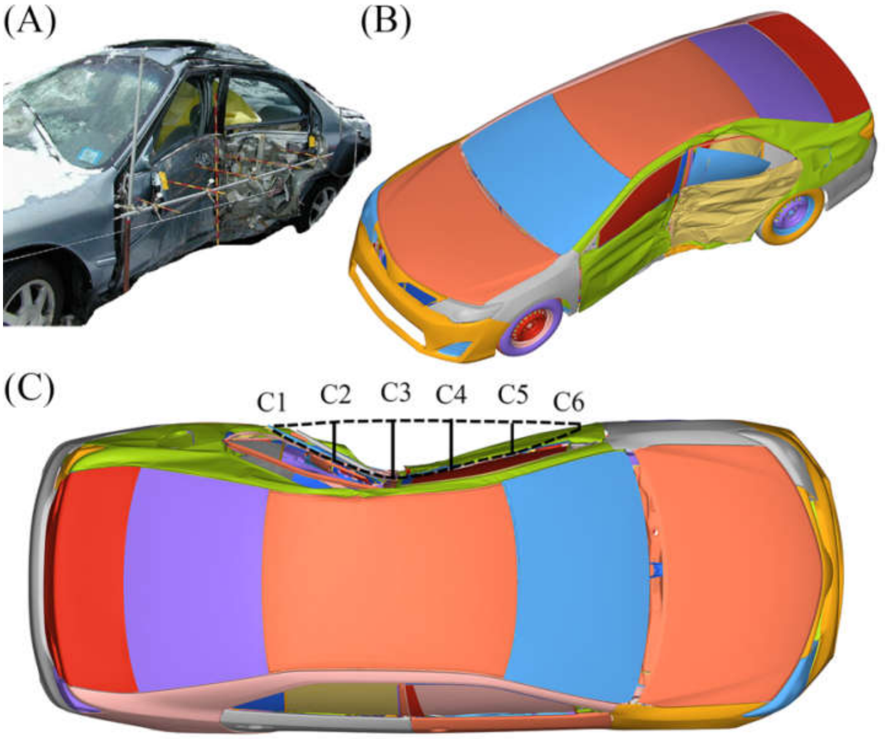

Figure N1. Comparison of deformation pattern between case vehicle (A) and numerical reconstruction (B, C), where C1-C6 correspond the locations of intrusion measurement (see Table 4.2)

APPENDIX O DETAILED INFORMATION OF SAMPLE PROPERTIES (GENDER, AGE, DIAMETERS AND LENGTH)

The aortic diameters and lengths were measured when the aortas were pressurized under 50mmHg before the mini-sled tests. The diameters (D1, D2 and D3) were measured at 3 locations presented in the sketch of the table below. The lengths were measured from vasalva sinus to the incision level (T8) along the inner curving of the aortic samples, since we could not measure the centerline length without in-vivo medical images. We should also bear in mind that there is no specific landmark at the T8 level during the sample incisions. The aortic lengths were only rough data to some extent.

Table O1. Summary of sample properties (gender, age, diameter and length)

ID	Gender	Age (Year)	D1 (mm)	D2 (mm)	D3 (mm)	L (mm)
Aorta-1	F	96	29	27	27	175
Aorta-2	F	85	31	29	29	185
Aorta-3	F	92	28	26	25	160
Aorta-4	F	87	25	25	23	180
Aorta-5	F	96	32	30	28	155
Aorta-6	M	93	30	28	27	170
Aorta-7	M	68	27	27	26	165
AV*	--	88	29	27	26	170
STD*	--	9	2	2	2	10

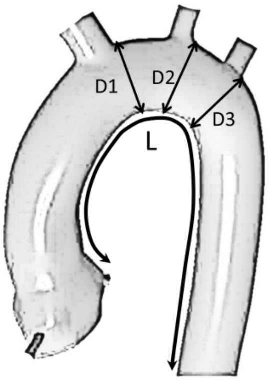

** AV-average value, STD-standard deviation.*